Finding the First Quasars at Birth

by

Marco Surace

This thesis is submitted in partial fulfilment of
the requirements for the award of the degree of
Doctor of Philosophy of the University of Portsmouth.

July 2, 2020

FORM UPR16

Research Ethics Review Checklist

Please include this completed form as an appendix to your thesis (see the Research Degrees Operational Handbook for more information

UNIVERSITY OF PORTSMOUTH

Postgraduate Research Student (PGRS) Information				**Student ID:**	795458
PGRS Name:	Marco Surace				
Department:	ICG	**First Supervisor:**	Dr. Daniel Whalen		
Start Date: (or progression date for Prof Doc students)	1st October 2015				
Study Mode and Route:	Part-time ☐	MPhil ☐	MD ☐		
	Full-time ☑	PhD ☑	Professional Doctorate ☐		

Title of Thesis:	Finding the First Quasars at Birth
Thesis Word Count: (excluding ancillary data)	27,676

If you are unsure about any of the following, please contact the local representative on your Faculty Ethics Committee for advice. Please note that it is your responsibility to follow the University's Ethics Policy and any relevant University, academic or professional guidelines in the conduct of your study

Although the Ethics Committee may have given your study a favourable opinion, the final responsibility for the ethical conduct of this work lies with the researcher(s).

UKRIO Finished Research Checklist:
(If you would like to know more about the checklist, please see your Faculty or Departmental Ethics Committee rep or see the online version of the full checklist at: http://www.ukrio.org/what-we-do/code-of-practice-for-research/)

a)	Have all of your research and findings been reported accurately, honestly and within a reasonable time frame?	YES ☑ NO ☐
b)	Have all contributions to knowledge been acknowledged?	YES ☑ NO ☐
c)	Have you complied with all agreements relating to intellectual property, publication and authorship?	YES ☑ NO ☐
d)	Has your research data been retained in a secure and accessible form and will it remain so for the required duration?	YES ☑ NO ☐
e)	Does your research comply with all legal, ethical, and contractual requirements?	YES ☑ NO ☐

Candidate Statement:

I have considered the ethical dimensions of the above named research project, and have successfully obtained the necessary ethical approval(s)

Ethical review number(s) from Faculty Ethics Committee (or from NRES/SCREC):	9626-A4C9-1254-819E-AFB8-2A5A-6675-4EEF

If you have *not* submitted your work for ethical review, and/or you have answered 'No' to one or more of questions a) to e), please explain below why this is so:

Signed *(PGRS)*:	M Surace	**Date:** 10/06/20

Certificate of Ethics Review

Project Title:	Near infrared luminosities of the first quasars
User ID:	795458
Name:	Marco Surace
Application Date:	14/11/2017 14:36:46

You must download your certificate, print a copy and keep it as a record of this review.

It is your responsibility to adhere to the University Ethics Policy and any Department/School or professional guidelines in the conduct of your study including relevant guidelines regarding health and safety of researchers and University Health and Safety Policy.

It is also your responsibility to follow University guidance on Data Protection Policy:

- General guidance for all data protection issues
- University Data Protection Policy

You are reminded that as a University of Portsmouth Researcher you are bound by the UKRIO Code of Practice for Research; any breach of this code could lead to action being taken following the University's Procedure for the Investigation of Allegations of Misconduct in Research.

Any changes in the answers to the questions reflecting the design, management or conduct of the research over the course of the project must be notified to the Faculty Ethics Committee. Any changes that affect the answers given in the questionnaire, not reported to the Faculty Ethics Committee, will invalidate this certificate.

This ethical review should not be used to infer any comment on the academic merits or methodology of the project. If you have not already done so, you are advised to develop a clear protocol/proposal and ensure that it is independently reviewed by peers or others of appropriate standing. A favourable ethical opinion should not be perceived as permission to proceed with the research; there might be other matters of governance which require further consideration including the agreement of any organisation hosting the research.

GovernanceChecklist
A1-BriefDescriptionOfProject: Performing cosmological simulations of the first quasars, and post-processing the output to extract synthetic observables
A2-Faculty: Technology
A3-VoluntarilyReferToFEC: No
A5-AlreadyExternallyReviewed: No
B1-HumanParticipants: No
HumanParticipantsDefinition
B2-HumanParticipantsConfirmation: Yes
C6-SafetyRisksBeyondAssessment: No

D2-PhysicalEcologicalDamage: No
D4-HistoricalOrCulturalDamage: No
E1-ContentiousOrIllegal: No
E2-SociallySensitiveIssues: No
F1-InvolvesAnimals: No
F2-HarmfulToThirdParties: No
G1-ConfirmReadEthicsPolicy: Confirmed
G2-ConfirmReadUKRIOCodeOfPractice: Confirmed
G3-ConfirmReadConcordatToSupportResearchIntegrity: Confirmed
G4-ConfirmedCorrectInformation: Confirmed

Abstract

Recent discoveries confirming the existence of supermassive black holes, with masses in excess of a billion solar masses, forming less than a billion years after the Big Bang poses a major challenge to our understanding of the formation of the first galaxies and black holes in the universe.

Amongst the main candidate theories for the formation of supermassive black hole seeds, it remains unclear whether stellar mass primordial star black hole seeds or seeds formed in dense stellar clusters would have encountered sufficient gas reservoirs in their host environments to grow rapidly, and it is expected that they would struggle to reach the required mass in the available time, even under conditions of persistent Eddington growth.

In this thesis we will focus our attention on the promising direct collapse black hole scenario in which a monolithic collapse occurs in a hot atomically cooled primordial halo exposed to a sufficiently strong Lyman-Werner flux from a nearby star forming halo. A supermassive primordial star forms at the centre of the halo which grows under accretion rates of up 1 $M_{\odot}$ yr^{-1} and reaches a mass of up to a few 10^5 $M_{\odot}$, before collapsing directly to a black hole.

We present realistic synthetic spectra of supermassive stars in their birth envelopes calculated using the spectral synthesis code Cloudy, with data extracted from cosmological simulations in which they were modelled using the radiation hydrodynamics code Enzo. Spectra are calculated for two types of supermassive star predicted by stellar evolution models: cool, red hypergiants at 6000-8000 K with luminosities greater than 10^{10} $L_{\odot}$ and hot, blue

stars with with surface temperatures of 20,000 - 40,000 K. We also calculate spectra for a direct collapse black hole at birth in its host environment that was born in cold accretion flows in which it is destined to grow to 10^9 $M_\odot$ by $z \sim 7$, again modelled using Enzo. We calculate near infrared AB magnitudes for these objects at source redshifts ranging from $z = 20$ down to 6 for various telescopes to be launched in the next decade, and determine out to which redshifts they are observable in the near infrared today given the instrumental detection limits.

Table of Contents

Abstract **i**

Declaration **xiii**

Acknowledgements **xiv**

Dissemination **xvi**

Notation **xviii**

1 Introduction **1**

1.1 The early universe 2

1.2 Dark Ages and the growth of large scale structure 3

1.3 The formation of the first stars 5

1.4 The formation of SMBH seeds 8

1.4.1 The mass growth of BHs 10

1.4.2 Stellar mass BHs 13

1.4.3 BH seeds from dense stellar clusters 18

1.4.4 Direct collapse black holes 19

1.4.5 DCBH observational signatures 29

1.5 Overview 32

2 Numerical Simulations **34**

2.1 Enzo 34

2.1.1 Numerical methods and physics 34

2.1.2 Physical Equations 36
2.1.3 Simulation box size 38
2.1.4 Random seed sifting 38
2.1.5 Quasar simulation 40
2.1.6 SMS envelope simulation 43
2.2 Other simulation campaigns 46
2.3 Cloudy 47
2.3.1 Setting up calculations 49
2.3.2 Cloudy tests 55
2.4 Redshifting source spectra and calculating AB magnitudes . . 65

3 On the Detection of Supermassive Primordial Stars 67
3.1 Abstract 67
3.2 Introduction 68
3.3 Numerical Method 70
3.3.1 Enzo Envelope Model 72
3.3.2 Cloudy Spectra 73
3.4 Observing Supermassive Stars 74
3.4.1 SMS Spectra 74
3.4.2 NIR Magnitudes 75
3.4.3 SMS Formation / Detection Rates 78
3.5 Conclusion 79

4 On the detection of supermassive primordial stars. II. Blue supergiants 82
4.1 Abstract 82
4.2 Introduction 83
4.3 Numerical Method 87
4.3.1 TLUSTY Atmosphere Models 87
4.3.2 Cloudy Models 88
4.4 Blue Supermassive Stars 91
4.4.1 Stellar Spectra 91

4.4.2 Reprocessed Spectra 91
4.4.3 NIR Magnitudes 95
4.4.4 SMS Detection Rates 96
4.5 Discussion and Conclusion 97

5 Finding the First Quasars at Birth **101**
5.1 Abstract 101
5.2 Introduction 101
5.3 Numerical Method 103
5.3.1 Enzo Model 103
5.3.2 Cloudy Spectra 107
5.4 Detecting DCBHs 108
5.4.1 NIR Magnitudes 109
5.4.2 DCBH Formation / Detection Rates 111
5.5 Discussion and Conclusion 112

6 Summary and Conclusions **114**
6.1 Aims 114
6.2 Simulations 115
6.3 Conclusions and Future Prospects 116

Bibliography **119**

List of Figures

1.1 Original diagram from Rees (1978) outlining the possible formation pathways for SMBHs. 9

1.2 Summary of the possible pathways to massive black holes via a stellar seed black hole, a quasi star or via a nuclear star cluster in DM haloes with $T_{\rm vir} \gtrsim 10^4$ K. Adopted from Regan & Haehnelt (2009b) 11

1.3 The fate of single stars as a function of their initial mass and initial metallicity. Tracks for the formation of DCBHs from the stars are highlighted in black whilst the white region in the bottom right indicates the range for a pair instability supernova. Adopted from (Heger et al., 2003) 14

1.4 Accretion rate history for $M_{\rm BH} = 10^3$ (green long dashed), 3×10^3 (blue short dashed), 5×10^3 (magenta dotted), 10^4 (red solid), and 2×10^4 $M_\odot$(orange dot-dashed). The radiative efficiency is assumed to be $\epsilon = 3/(10 + 3\dot{m})$ (the trapping model). The density of the ambient gas is 10^5 cm^{-3}. For $M_{\rm BH} < 10^4$, the average accretion rate is limited to $\dot{m} \lesssim 10$. For higher BH mass ($M_{\rm BH} \geq 10^4$ $M_\odot$), a big jump of the accretion rate occurs and the accretion rate approaches a constant value, where $\dot{M} \simeq 8000 \dot{M}_{\rm Edd}$. Adopted from Inayoshi et al. (2016). 16

1.5 Mass assembly history of a seed, non-rotating BH with $M_0 = 100\ M_\odot$ accreting intermittently at $\dot{m}/\dot{m}_E = 3$ with a duty cycle of 0.5 (*orange solid line*) and at $\dot{m}/\dot{m}_E = 4$ with a duty cycle of 0.2 (*gray dashed line*). In both cases the period of quiescence is 100 Myr. Adopted from Madau et al. (2014). . . 17
1.6 Time evolution of the maximum mass in a stellar cluster system for six different accretion models. The models vary by whether the gas reservoir is infinite or finite, and whether a position or time dependent accretion model is used. Except for Model 5, all models efficiently convert at least half of the initial gas mass into a single massive object. Adopted from Boekholt et al. (2018). 20
1.7 Density-temperature diagram for primordial gas collapse. Cooling via atomic H leads to a DCBH (solid), while cooling via molecular hydrogen leads to Pop. III stars (dashed). Figure taken from Agarwal et al. (2016a) 23
1.8 Density-temperature diagram for the collapse of primordial gas irradiated by Far UV radiation ($h\nu < 13.6$ eV). The evolutionary tracks are drawn for various values of J_{21}, where the highest value corresponds to the atomically cooling track. The dashed lines indicate a constant Jeans mass. Taken from (Omukai, 2001). 25

1.9 The synchronised haloes scenario. In case A, with only a background LW radiation field, a (delayed) Pop III star forms due to H_2 cooling. In case B, a DCBH can form in an atomically cooling halo if a nearby star-burst galaxy and the radiation background provide the critical LW flux required. T_{sync} is defined as the time between the star-burst turning on and the point at which a Pop III would have formed. T_{on} is the time taken for an atomic cooling halo to collapse and form a DCBH (or the minimum time the source must shine for). Adopted from Regan et al. (2017). 27

1.10 Left panel: formation of on OBG when a DCBH seed merges with its parent star forming halo. Star formation is quenched in the DCBH host halo due to LW photons from the neighbouring SF halo. However, a stellar component is accrued promptly via merging with the parent SF galaxy leading to the formation of an OBG. Right panel: sequence for a growing Pop III remnant BH seed. Adopted from Natarajan et al. (2017). 31

2.1 2D temperature slice projected along the z axis, weighted by density, for a quasar at $z = 19$. The quasar is almost visible as a dot at the centre of the slice, surrounded by gas flows of varying temperature. 44

2.2 Phase plots of the gas temperature (upper panel) and ionized fraction (lower panel) for a quasar at $z = 19$ 51

2.3 An illustration of the two approaches to modelling a cloud in the Cloudy code. In both cases each pair of arcs corresponds to a single spherical shell or Cloudy model. Left panel: using a single model to represent the entire cloud, in which the density is allowed to vary. Right panel: using multiple Cloudy models to represent the cloud, where the density is fixed for each individual model, but can vary between models. 52

2.4 Upper Panel: A TLUSTY source frame spectrum for a hot blue metal-free supermassive star under an accretion rate of 1 $M_{\odot}$ yr^{-1}. Lower Panel: The same spectrum once it has been ported to Cloudy, with some emission and absorption lines absent. 57
2.5 1D profiles of a quasar H II region at $z = 16$ for the gas temperature, as calculated by Enzo (blue), and by Cloudy (green). Here Cloudy assumes that the illuminating source at the centre of the model is the only source of heating. Cloudy captures more of the heating due to the emitted radiation at shorter radii, whereas Enzo captures the hydrodynamical heating at larger radii further from the central source. 58
2.6 Comparing the AB magnitude in the *JWST* NIRcam F444W filter for a quasar at different source redshifts for three different sets of metal abundances in Cloudy: solar metallicity (blue crosses), Enzo 1D profile metallicities (green crosses), and a primordial metallicity (red crosses). The AB magnitudes tend to be highest for solar metallicity, and lowest for primordial metallicity gas. 60
2.7 A quasar spectrum at a source redshift of $z = 17$ in the observer frame, before (blue curve) and after (green curve) transmission by the *JWST* F250M filter. 62
2.8 1D spherically averaged gas temperature profiles for a quasar at $z = 19$ created with 16 bins (top left), 32 bins (top right), 64 bins (bottom left), and 256 bins (bottom right). Zero-valued bins are present for 64 and 256 bin profiles. 64

3.1 Evolution of red supergiant (RSG) stars with an initial mass of 10 $M_{\odot}$ accreting at 1.0 and 0.1 $M_{\odot}$ yr^{-1} in the GENEVA stellar evolution code. Left panel: luminosities. Right panel: surface temperatures. 69

3.2 Top left: 2D density slice (6 pc proper on a side) of the accretion disk at 0.625 Myr after the onset of collapse. Top right: central accretion rates. Bottom left: spherically-averaged gas densities in the halo. Bottom right: spherically-averaged temperatures. 71
3.3 1.0 $M_\odot$ yr^{-1} SMS spectra at a stellar age of 100,000 yr. Blue: spectrum of the star itself; red: spectrum after reprocessing by the envelope. 76
3.4 NIR AB magnitudes for the 1.0 $M_\odot$ yr^{-1} (solid) and 0.1 $M_\odot$ yr^{-1} (dashed) SMSs in *JWST*, *Euclid* and *WFIRST* bands. Top left: *JWST* NIRCam bands. Top right: *JWST* MIRI bands. Bottom left: *Euclid*. Bottom right: *WFIRST*. The horizontal lines are the 5σ AB magnitude detection limits for 100 hour exposures in the filter of the corresponding colour for the *JWST* filters, and the detection limits for deep-drilling fields in *Euclid* and *WFIRST*. 77

4.1 Top row: evolution of SMSs accreting at 1.0 and 0.1 $M_\odot$ yr^{-1} in our Kepler models. Left panel: surface temperatures. Right panel: luminosities. Evolution lines for the two stars end at different times because the less rapidly accreting star lives for a much longer time. Bottom row: spherically-averaged profiles of the dense, atomically-cooled shroud surrounding the star 0.238 Myr after the formation of the accretion disk. Left: gas densities. Right: temperatures. 86

4.2 Top row: spectra of the two blue SMSs in our study. Red: uncorrected BB spectrum. Blue: TLUSTY model. Left: the 0.1 $M_\odot$ yr^{-1} star at 8.01 $\times$ 10^5 yr and $T_{\rm eff}$ = 22,093 K. Right: the 1.0 $M_\odot$ yr^{-1} star at 1.51 $\times$ 10^5 yr and $T_{\rm eff}$ = 36,963 K. Bottom row: spectra emerging from the accretion envelopes of the stars. Blue: incident stellar spectrum. Red: spectrum after reprocessing by the envelope. Left: the 0.1 $M_\odot$ yr^{-1} star. Right: the 1.0 $M_\odot$ yr^{-1} star. 90

4.3 NIR AB magnitudes for the 1.0 $M_\odot$ yr^{-1} blue SMS in *JWST*, *Euclid* and *WFIRST* bands. Solid line: with the accretion envelope but no contribution from its Lyα line. Dashed line: no envelope. Dotted line: with the envelope and its Lyα line. Top left: *JWST* NIRCam bands. Top right: *JWST* MIRI bands. Bottom left: *Euclid filters*. Bottom right: *WFIRST filters*. The horizontal lines are the 5σ AB magnitude detection limits for 100 hour exposures in the filter of the corresponding colour for the *JWST* filters, and the detection limits for deep-drilling fields in *Euclid* and *WFIRST*. 92

4.4 NIR AB magnitudes for the 0.1 $M_\odot$ yr^{-1} blue SMS in *JWST*, *Euclid* and *WFIRST* bands. Solid line: with the accretion envelope but no contribution from its Lyα line. Dashed line: no envelope. Dotted line: with the envelope and its Lyα line. Top left: *JWST* NIRCam bands. Top right: *JWST* MIRI bands. Bottom left: *Euclid filters*. Bottom right: *WFIRST filters*. The horizontal lines are the 5σ AB magnitude detection limits for 100 hour exposures in the filter of the corresponding colour for the *JWST* filters, and the detection limits for deep-drilling fields in *Euclid* and *WFIRST*. 93

5.1 Ionized H fraction in the vicinity of the DCBH z = 17. The image is 30 kpc proper on a side. 104

5.2 Rest frame spectra for the DCBH at $z = 19$ before (blue) and after (red) reprocessing by its host halo. 105

5.3 NIR AB magnitudes for the 1.0×10^5 $M_\odot$ DCBH at birth as it would appear at $z = 8$ - 20 in *JWST*, *Euclid* and *WFIRST*. Top left: *JWST* NIRCam bands. The horizontal dashed lines are 5σ AB magnitude detection limits for 100 hour exposures in the filters of corresponding color (2.77 μm: 31.4, 3.56 μm: 31.5, 4.44 μm: 31.0 and 4.60 μm: 29.8). Top right: *JWST* MIRI bands. The horizontal dashed lines are 5σ AB magnitude detection limits for 100 hour exposures in the filters of corresponding color (5.6 μm: 28.0, 7.7 μm: 27.6, 10.0 μm: 27.0, 15.0 μm: 26.1 and 18.0 μm: 24.7). Bottom left: *Euclid*. Bottom right: *WFIRST*. The horizontal dashed lines are detection limits for each instrument (32 for NIRCam, 28 for MIRI assuming a 20 hr exposure, and 26 and 28 for deep-drilling fields in *Euclid* and *WFIRST*, respectively. 110

Declaration

Whilst registered as a candidate for the above degree, I have not been registered for any other research award. The results and conclusions embodied in this thesis are the work of the named candidate and have not been submitted for any other academic award.

Word count: 27,676 words.

Acknowledgements

Firstly, I would like to thank my supervisor Daniel Whalen for all his help and guidance. I would also like to thank all our collaborators without whose expertise the work could not have been carried out. In particular I would like to thank Claes-Erik Rydberg and Mohammed Latif for taking the time to answer my questions and provide helpful advice.

Gary Burton at the ICG provided me with tremendous amounts of advice and support on using the Sciama HPC cluster for my simulations. He really is the best HPC administrator one could hope for.

I would also like to mention all the academics at the ICG, who together created a very welcoming and friendly environment there. Their wealth of knowledge was disseminated week after week at Tuesday talks or during tearoom chats, which broadened my physics horizons.

Although we were never based at the same institution apart from the first few months of the PhD in Heidelberg, Carla Bernhardt was a great 'academic sister' to have, and I wish her all the best to her and her family and a successful conclusion to her PhD. Thanks also to Sam Patrick, for being someone I could bounce ideas off of, and vent frustrations about codes with.

Thank you to all my fellow PhD friends, Ben, Ben, Lucy, Taniya, Paul, Pier, and Rob, for all the fun times and endlessly fascinating conversations and debates we've had over the years. One could not hope for better office pals, and I'm sure you'll all go on to achieve great things.

Lastly and most importantly, I would like to thank my parents for all

their care and support. And to my wife Anna, thank you for being there for me through all the ups and downs, and for all your love and support. I know it has been a testing time, and being apart did not make it any easier, but I couldn't have done it without you.

Dissemination

Publications

D. J. Whalen, **M. Surace**, C. Bernhardt, E. Zackrisson, F. Pacucci, B. L. Ziegler, M. Hirschmann. *Finding the first quasars at birth.* Accepted by Astrophysical Journal Letters, arXiv:2005.03018, May 2020.

M. Surace, E. Zackrisson, D. J. Whalen, T. Hartwig, S. C. O. Glover, T. E. Woods, and A. Heger. *On the detection of supermassive primordial stars - II. Blue Supergiants.* Monthly Notices of the Royal Astronomical Society, 488(3):3995-4003, July 2019.

M. Surace, D. J. Whalen, T. Hartwig, E. Zackrisson, S. C. O. Glover, S. Patrick, T. E. Woods, A. Heger, and L. Haemmerlé. *On the detection of supermassive primordial stars.* The Astrophysical Journal, 869(2):L39, December 2018.

T. E. Woods, B. Agarwal, V. Bromm, A. Bunker, K. Chen, S. Chon, A. Ferrara, S. C. O. Glover, L. Haemmerlé, **M. Surace** et al. *Titans of the early universe: The prato statement on the origin of the first supermassive black holes.* Publications of the Astronomical Society of Australia, 36, August 2019.

J. Smidt, D. J. Whalen, J. L. Johnson, **M. Surace**, and H. Li. *Radiation Hydrodynamical Simulations of the First Quasars.* The Astrophysical Journal, 865:126, October 2018.

M. Surace, K. D. Kokkotas, and P. Pnigouras. *The stochastic background of gravitational waves due to the f-mode instability in neutron stars.* Astronomy & Astrophysics, 586:A86, January 2016.

Talks

First Stars V, Title: *Forming the first quasars in Enzo*, University of Heidelberg, Germany, August 2016

Illuminating the Dark Ages: Quasars and Galaxies in the Reionization Epoch, Title: *Near Infrared signatures of the first quasars*, Max Planck Institute for Astronomy, Germany, June 2016

Dublin Workshop, Title: *Near infrared luminosities of the first quasars*, Dublin City University, Ireland, January 2017

Notation

AGN - Active Galactic Nucleus

AMR - Aaptive Mesh Refinement

BH - Black Hole

CMB - Cosmic Microwave Background

DCBH - Direct Collapse Black Hole

E-ELT - European Extremely Large Telescope

IGM - Intergalactic Medium

ISM - Interstellar Medium

JWST - James Webb Space Telescope

LW - Lyman Werner

NIR - Near Infrared

SED - Spectral Energy Distribution

SMBH - Supermassive Black Hole

SMS - Supermassive Star

SNe - Supernova Explosion

WFIRST - Wide Field Infrared Survey Telescope

Chapter 1

Introduction

Quasars, or quasi-stellar radio sources, were first identified during the 1950s as sources of radio-wave emission of unknown physical origin, resembling faint star-like points of light at visible wavelengths. Today, they are known to be active galactic nuclei (AGN) which lie at the center of distant highly luminous galaxies where the excess luminosity is non-stellar in origin. AGN are supermassive black holes (SMBHs) 10^6 - 10^9 times the mass of the Sun surrounded by a hot accretion disk that emits copious amounts of electromagnetic radiation, up to 10^{13} times the luminosity of the Sun ($\gtrsim 10^{46}$ erg s^{-1}). This huge amount of emission is powered by the gravitational infall of matter which is heated to high temperatures in a dissipative accretion disk.

The discovery of SMBHs with masses in excess of 10^9 $M_\odot$ at $z \sim 7$, when the universe was less than 5% of its current age, including ULAS J1120+0641, a 2×10^9 $M_\odot$ black hole (BH) at $z = 7.1$ (Mortlock et al., 2011), and ULAS J1342+0928, an 8.0×10^8 $M_\odot$ BH at $z = 7.5$ (Bañados et al., 2018) poses a strong challenge to theories of SMBH formation. The masses of these objects are all inferred from the width of the observed Mg II 2798 Å line (e.g., McLure & Dunlop, 2004), and are consistent with a luminosity near the Eddington limit , i.e the maximum luminosity of an accreting BH assuming spherically symmetric mass accretion (see section 1.4.1).

The question of how black holes reached billions solar masses by $z \sim 7$,

when the universe was only $\sim$ 800 Myr old, remains unsolved since a timing problem exists if they grew under conventional accretion scenarios, i.e. via Eddington accretion. Numerical modelling of their formation and growth with realistic primordial gas physics and radiative feedback, along with observational follow-up by new telescopes, is required in order to put constraints on their seeding mechanisms and growth histories. In this thesis, we seek to provide realistic observational predictions for quasars and supermassive primordial stars, that in time can be verified by observations, which will help improve our understanding of the formation of SMBHs.

In this chapter, we give a brief introduction to structure formation in the early universe, before describing the formation of the first metal-free stars, a potential progenitor for SMBH seeds. We then describe the three most popular formation scenarios for SMBH seeds, before focusing our attention on the promising direct collapse black hole scenario.

1.1 The early universe

The seeds for large-scale structure formation in the universe were sown early on by tiny inhomogeneities in the primordial plasma, when the universe was still radiation dominated. These grew through self-gravity to form the present day galaxies and galaxy clusters, including the formation sites of the first SMBHs. Around 380,000 years after the Big Bang ($z \sim 1400$) the universe had cooled and expanded sufficiently for free electrons and protons to combine globally to form the first neutral atoms: hydrogen, helium, and trace amounts of lithium, a process known as recombination. The universe also became transparent for the first time since photons with energies $h\nu < 13.6$ eV were able to travel freely without scattering off of free electrons, which is known as photon decoupling.

As the universe continued to expand, the wavelengths of these photons were stretched to form the cosmic microwave background radiation (CMB) we observe today with a blackbody temperature of $T = 2.725$ K. The quantum

scale fluctuations in the early universe have all left their imprints on the CMB photons in the form of temperature anisotropies. Other physical phenomena can also affect them, such as the Sachs-Wolfe effect which is a result of gravitational redshift due to interactions with the intervening matter between the surface of last scattering and the Earth. In addition, high energy electrons in galaxy clusters are able to leave an imprint upon the CMB though inverse Compton scattering by collisions with low energy CMB photons, an effect known as the Sunyaev-Zeldovich effect. The spectrum of these fluctuations, expressed in terms of spherical harmonics on the sky, contains a wealth of information on the conditions of the early universe and can be used to provide constraints on cosmological models.

1.2 Dark Ages and the growth of large scale structure

Once the wavelength of CMB photons was stretched beyond the visible and into the infrared due to cosmic expansion, the universe appeared entirely dark due to the absence of any stars, hence this period is known as the Dark Ages. Apart from CMB photons, the only other source of photons were 21 cm line photons emitted by the forbidden spin-flip transition of the ground state in neutral hydrogen.

Collisionless dark matter, which comprises over 80% of the matter in the universe, gradually pooled itself into filaments, sheets, and haloes due to gravitational mergers and instabilities, with large voids formed in between. The patchiness of the dark matter distribution at $z \sim 1400$, as indicated by the temperature anisotropies observed by the Planck satellite for example, became increasingly pronounced due to gravitational collapse. Considering the power in the CMB spectrum at different length scales, long wavelength perturbations in the primordial density field evolved into the most massive structures but were rare, whereas shorter wavelength ripples formed smaller but more numerous minihaloes. The theoretical halo mass function as a

function of redshift is modeled statistically by Press-Schechter (PS) formalism (Press & Schechter, 1974), and has been computationally and observationally verified to be accurate on large scales. The concept that modern galaxies and clusters of galaxies were built bottom up by mergers of smaller objects in the denser environment of the high-redshift universe is known as the hierarchical structure formation paradigm of cosmology (White & Rees, 1978).

The patchiness of the universe in this era can also be probed through observations of high redshift quasar spectra. Radiation emitted by a quasar falling at a wavelength of 1216 Å is absorbed and scattered by neutral hydrogen, since it corresponds to the energy of the electronic transition between the ground state ($n = 1$) and the first excited state ($n = 2$), i.e. the Lyman-alpha transition. Photons at this wavelength passing through the neutral intergalactic medium (IGM) will thus not be observed on Earth. For quasars observed around $z \sim 6 - 7$, their spectra blueward of the Lyman-alpha line are completely suppressed since these photons are redshifted towards the Lyman-alpha line wavelength as they travel towards us and encounter the IGM at various redshifts or distances from Earth. This effect is known as the Gunn-Peterson trough, and it indicates that the universe was still partly neutral at $z \sim 6$, which is thought to be the end of the epoch of reionization, when the universe transitioned from its neutral state to the ionized state that it remains in today (though significantly less dense than it was before decoupling). Quasars at lower redshifts of $z \sim 3$ demonstrate a series of absorption lines blueward of Lyman-alpha, known as the Lyman-alpha forest, which indicates that the photons travelled through ionized regions along filaments, and more neutral regions within voids, on scales of 2-3 Mpc, that were the precursors of modern large-scale clusters of galaxies.

1.3 The formation of the first stars

Baryonic matter, gravitationally coupled to the dark matter dynamics, coalesced along the dark matter filaments. Able to cool via emission of photons, baryonic matter collapses to higher densities than dark matter is capable of, which leads to the formation of the first clouds of mainly hydrogen gas, and from around 150 Myr after the big bang ($z \sim 20 - 30$), the formation of the first stars.

The first generation of stars in the universe, known as Population III (Pop III) stars, were responsible for ending the cosmic Dark Ages and played their role in reheating and reionizing the neutral IGM. They formed from pristine clouds of mainly hydrogen and helium gas, since heavier elements can only be synthesized in stellar interiors or in supernova explosions.

According to the Jeans criterion for gravitational collapse of self-gravitating isothermal gas spheres, there is a critical mass $M_{\rm J}$ given by

$$M_{\rm J} \approx 50 M_{\odot} \mu^{-2} \left(\frac{n}{1{\rm cm}^{-3}}\right)^{-1/2} \left(\frac{T}{1K}\right)^{3/2}, \tag{1.1}$$

where n is the particle number density, T is the gas temperature, and μ is the mean molecular weight of the gas particles, which takes a value of 1.22 for primordial atomic gas and 2.33 for molecular gas. If the critical mass is exceeded, gravity overwhelms pressure gradients and the system collapses, otherwise if the mass is smaller the sphere remains supported by pressure against collapse. Therefore, to trigger star formation in an otherwise stable medium, either the density needs to increase (say, due to an external compression by a shock wave from a nearby supernova explosion) or the temperature needs to decrease (by some cooling process). In other words, if the free-fall time is smaller than the sound crossing time, $t_{\rm ff} < t_{\rm sound}$ then the system collapses, otherwise sound waves travel fast enough to wipe out inhomogeneities and the system is stable.

The first stars are expected to form in dark matter minihaloes of typical mass $\sim 10^6\ M_{\odot}$ at redshifts $z \sim 20 - 30$, as confirmed by various simulations (Abel et al., 1998; Bromm et al., 2002; Yoshida et al., 2003), see also reviews

by (Bromm et al., 2009; Bromm & Yoshida, 2011). Less massive haloes could not accumulate the amount of gas required for molecular hydrogen to form and trigger star formation, whereas haloes above 10^7 $M_\odot$ had virial temperatures too high for efficient molecular hydrogen production, a vital gas coolant.

As gas collapses onto the centre of the halo and is adiabatically compressed, the temperature rises due to atomic collisions. A process of virialization occurs, whereby the bulk velocity of the gas is converted to disordered motion. Once a sphere of matter ceases to collapse and reaches a stable state, it is said to have reached virial equilibrium or be virialized. Within the virial radius, the sphere obeys the virial theorem, which states that the average kinetic energy equals half of the average negative potential energy. The virial temperature of the gas depends on the depth of the potential well, and hence on the dark matter mass of the halo. As the gas temperature rises, it becomes more stable due to the increase in pressure support, and therefore requires a means of cooling in order for collapse to occur.

Cooling channels can only be activated once the particles collide with sufficient energy to impart the transition energy of a radiative line to each other. Around temperatures of $\sim 10^4$ K, collisions can populate the first excited electronic states of H which then de-excite by emitting Lyα photons. Typical gas temperatures in minihaloes of at most around $\sim 10^3$ K are however below the threshold for efficient cooling due to atomic hydrogen (Bromm & Loeb, 2003). In order to reach lower temperatures, molecular hydrogen (H_2) is required.

At low densities, H_2 forms mainly via the H^- channel, which requires free electrons (left over from the era of recombination or from collisional ionization in virial shocks):

$$H + e^- \rightarrow H^- + \gamma \tag{1.2}$$

$$H^- + H \rightarrow H_2 + e^- \tag{1.3}$$

This can lead to a molecular abundance as high as 10^{-5}, which is sufficient

to cool the gas through its many low-energy rotational and vibrational emission lines (ro-vibrational modes), even in competition with the compressional heating during the collapse, reaching a minimum temperature of ~ 200 K at a density of $n \sim 10^4$ cm^{-3}. This is the density at which the gas encounters the quasi-hydrostatic 'loitering phase', at which the H_2 cooling rate saturates, becoming less efficient towards higher densities.

Once the gas has reached densities higher than $\sim 10^8$ cm^{-3}, and in the absence of dust grains, runaway H_2 formation occurs via three-body reactions:

$$H + H + H \rightarrow H_2 + H \tag{1.4}$$

$$H + H + H_2 \rightarrow H_2 + H_2 \tag{1.5}$$

upon which the gas becomes fully molecular by $n \sim 10^{12}$ cm^{-3}. The gas remains roughly isothermal at $T \sim 1000$ K over several decades in density as collapse proceeds, due to the approximate balance between H_2 formation (release of its binding energy) and compressional heating, and enhanced H_2 cooling.

At increasingly high densities of $n > 10^{12}$ cm^{-3} the cloud becomes optically thick, including to the ro-vibrational lines of H_2, allowing the temperature of the gas to exceed $T \sim 2000$ K at $n \sim 10^{16}$ cm^{-3}. At this point, H_2 is being collisionally dissociated, in reactions that revert the previous three-body formation processes. In turn, the corresponding removal of the molecular binding energy from the thermal reservoir of the gas provides a final cooling channel in the otherwise already optically-thick gas.

At the end of the initial collapse a small protostellar hydrostatic core forms at the centre of the minihalo of $\sim 10^{-3}\ M_\odot$ surrounded by an accretion disk, which grows under accretion rates $\lesssim 0.0001 M_\odot$ yr^{-1}, typically two orders of magnitude higher than those in present-day molecular clouds (due to the higher temperatures in primordial star-forming clouds thanks to its limited cooling ability). More recent simulations (Turk et al., 2009; Stacy et al., 2010; Clark et al., 2011; Greif et al., 2011b, 2012) suggest that instead of a single high-mass star forming at the centre on the order of $\sim 100\ M_\odot$

the accretion disk around the protostar may fragment due to gravitational instability resulting in a small cluster of stars with a wide range of masses. According to (Hosokawa et al., 2011; Hirano et al., 2014, 2015) however, even in the absence of fragmentation ionizing UV radiation from the nascent star terminates accretion onto the star at final masses of 30 - 600 $M_{\odot}$. Therefore the mass spectrum of the resulting Pop III stars is expected to range from $\sim 1\ M_{\odot}$ up to $\sim 600\ M_{\odot}$, far higher than stars found in our Galaxy today.

1.4 The formation of SMBH seeds

The first summary of possible SMBH formation pathways was laid out in the Halley Lecture of 1978 at Oxford University (Rees, 1978), in which various hypothesized progenitor objects were suggested within the so-called Rees diagram, including supermassive stars and dense stellar clusters, among others (see Figure 1.1). Many of the channels indicated in the diagram remain plausible but unproven till this day, and it is unclear how often each channel may be realized in nature.

Alternative channels for producing massive seeds, including massive high redshift galaxy mergers (Mayer et al., 2010; Mayer & Bonoli, 2019) and the disruption of dense stellar clusters (e.g. Begelman & Rees, 1978; Katz et al., 2015; Sakurai et al., 2017) have also been the subject of significant investigation, although questions remain regarding the nature of the remnants they produce (see e.g. Latif & Ferrara, 2016, for a through discussion). Yet other more exotic channels, such as the growth of primordial black holes (Zel'dovich & Novikov, 1967), or intermediate-mass black holes formed from dissipative dark matter (D'Amico et al., 2018), remain somewhat speculative at the present time, and require further study.

Below we will discuss the three most popular massive BH seed formation scenarios in the literature (Latif & Ferrara, 2016): (i) core-collapse of massive Pop III stars, (ii) runaway collisions in dense nuclear star clusters, and (iii) catastrophic baryon collapse in pristine, atomically-cooled haloes and

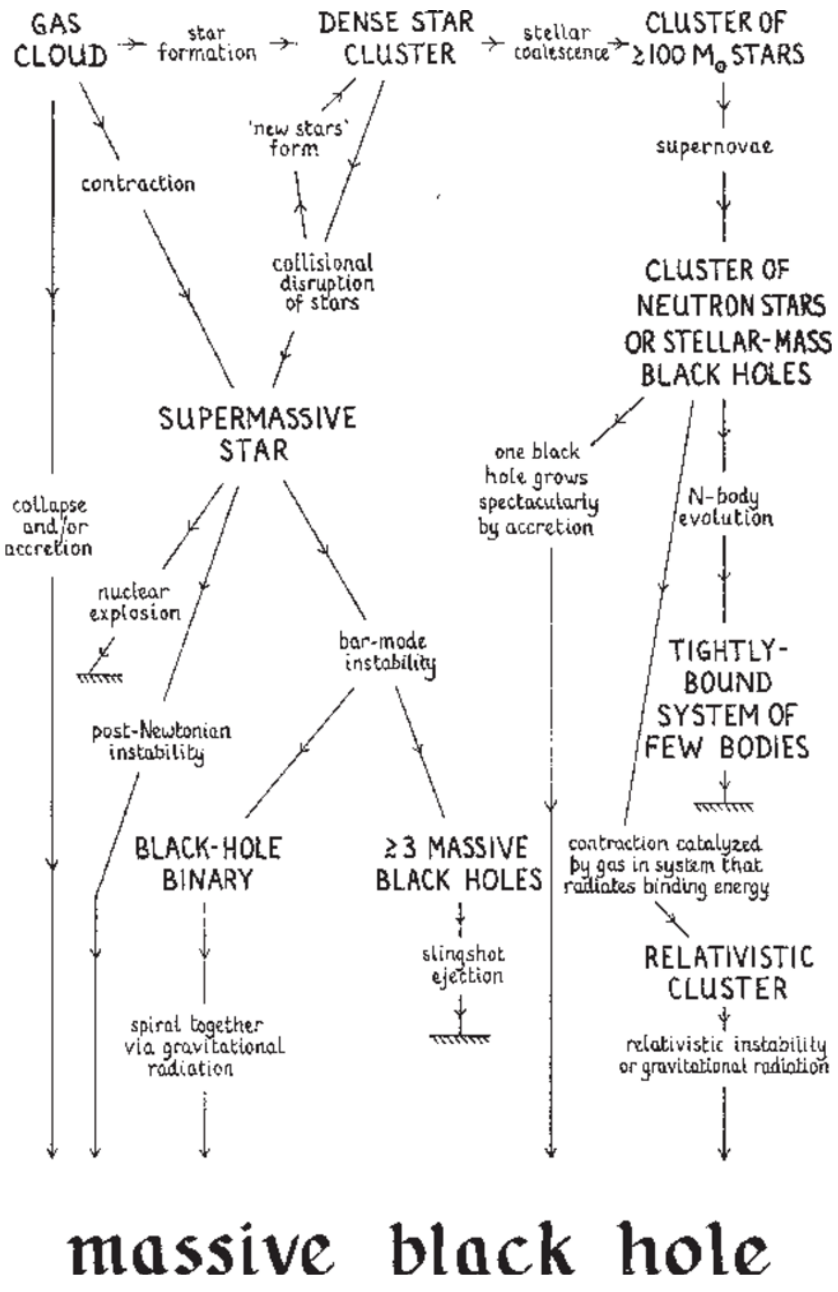

Figure 1.1: Original diagram from Rees (1978) outlining the possible formation pathways for SMBHs.

the formation of direct-collapse black holes (DCBHs). The latter channel, considered one of the most promising, is the model we adopt in our own work. The three channels are summarized in Figure 1.2, which all start from a pre-galactic DM halo with $T_{\rm vir} \gtrsim 10^4$.

1.4.1 The mass growth of BHs

Gas falling into a BH loses potential energy, which is converted into kinetic energy. Since the gas tends to have a non-zero angular momentum it forms a rotationally supported disk, and heats up due to friction between gas particles. According to the virial theorem, half of the potential energy released is converted into kinetic energy, and the other half is converted into internal (thermal) energy. Most of this energy is generated in the innermost region of the disk, close to the Schwarzschild radius, where the temperature is highest. This energy propagates outwards and can interact with infalling matter by absorption or scattering, transferring momentum to the matter. In order for matter to fall onto the SMBH, this outwards radiation pressure force must be smaller than the gravitational force. From this condition we can derive a minimum mass for the SMBH, required for its gravity to dominate the total force at a given luminosity.

In what follows we consider a fully ionized gas so that the interaction between radiation and the infalling plasma is mainly due to the scattering of photons by free electrons, i,e, Thomson scattering. The flux, i.e. the radiation energy that flows through a unit area at a distance r from the central source per unit time, is given by $S = L/4\pi r^2$, where L is the luminosity of the source. Since the momentum carried by a photon is $p = E/c$, then S/c is the momentum of photons flowing through this unit area per unit time. Thus the momentum transfer to an electron per unit time, i.e. the radiation force, is given by

$$F_{\rm rad} = \sigma_{\rm T} \frac{L}{4\pi r^2 c}, \tag{1.6}$$

where $\sigma_{\rm e}$ is the Thomson scattering cross-section.

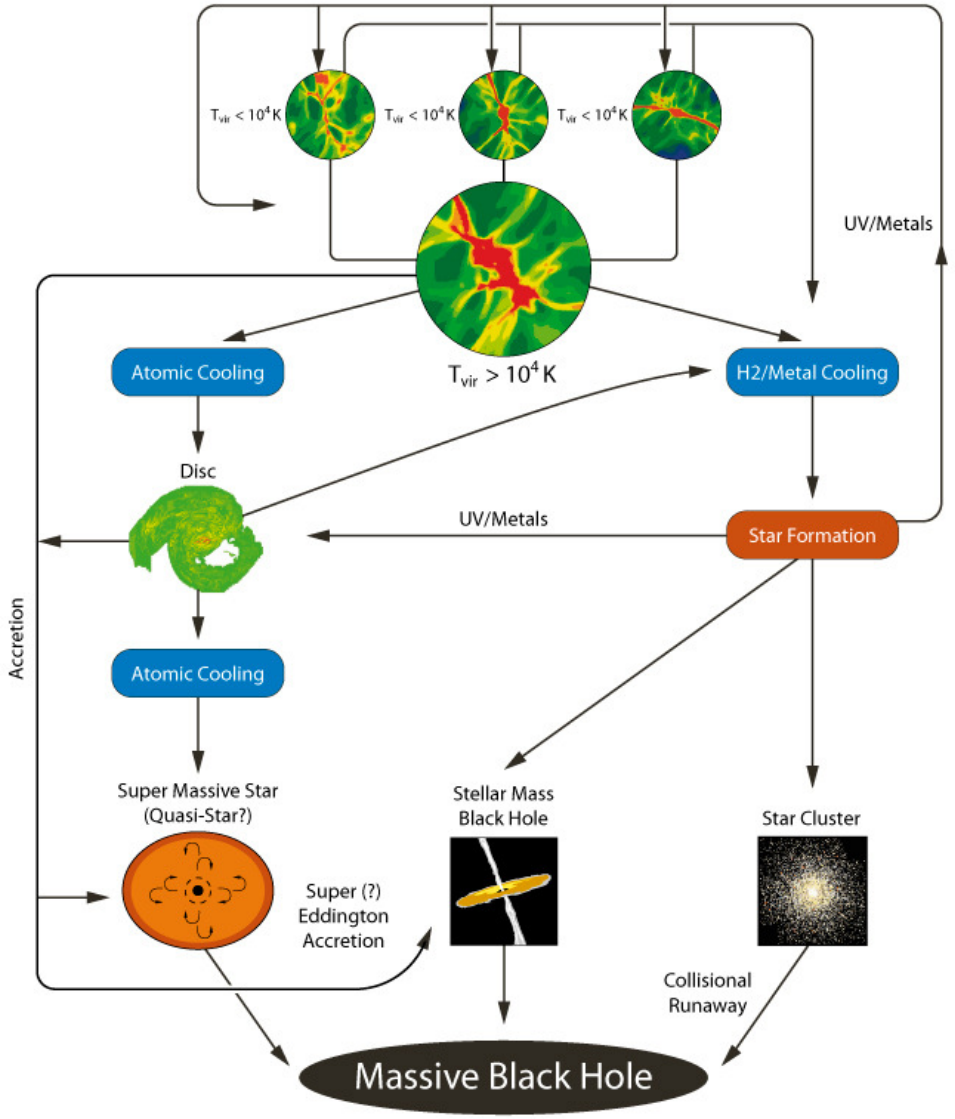

Figure 1.2: Summary of the possible pathways to massive black holes via a stellar seed black hole, a quasi star or via a nuclear star cluster in DM haloes with $T_{\rm vir} \gtrsim 10^4$ K. Adopted from Regan & Haehnelt (2009b)

The gravitational force acting on an electron-proton pair is

$$F_{\rm grav} = \frac{GM_{\rm BH}(m_{\rm p} + m_{\rm e})}{r^2} \approx \frac{GM_{\rm BH}m_{\rm p}}{r^2}, \tag{1.7}$$

where $M_{\rm BH}$ is the BH mass and $m_{\rm e}$ and $m_{\rm p}$ are the mass of the electron and proton respectively. The electron's mass may be neglected since it is nearly 2000 smaller than the proton mass. The condition for dominance of gravity can thus be written as

$$\begin{aligned} F_{\rm rad} &< F_{\rm grav} \\ \frac{\sigma_{\rm T} L}{4\pi r^2 c} &< \frac{GM_{\rm BH}m_{\rm p}}{r^2}, \end{aligned} \tag{1.8}$$

or

$$L < \frac{4\pi G c m_{\rm p}}{\sigma_{\rm T}} M_{\rm BH} =: L_{\rm E}, \tag{1.9}$$

where we have defined the Eddington luminosity $L_{\rm E}$ of a BH of mass $M_{\rm BH}$, which is the bolometric luminosity since it is independent of photon frequency. We can use this equation to place a lower limit on $M_{\rm BH}$ from the observed luminosity L.

The above definition of the Eddington luminosity assumes that the emission of radiation is isotropic. This luminosity can be exceeded in non-spherically symmetric models, where for example the mass accretion occurs primarily equatorially in a disk, but the radiation emerges primarily along the disk axis.

If the conversion of infalling mass into energy takes place with an efficiency ϵ, the accretion rate $\dot{m}$ can be determined from

$$\dot{m} = \frac{L}{\epsilon c^2}, \tag{1.10}$$

where ϵ has a typical value of 0.1 for radiatively efficient thin-disk accretion. We can then define the Eddington accretion rate as the maximum accretion rate if isotropic emission is assumed, given by

$$\dot{m}_{\rm E} = \frac{L_{\rm E}}{\epsilon c^2}. \tag{1.11}$$

At an accretion rate of $\dot{m}$, the growth rate of the BH is $\dot{M}_{\rm BH} = (1-\epsilon)\dot{m}$, since a fraction ϵ of the accretion rate is converted into luminosity, and thus does not contribute to the increase of the BH mass. Assuming that the BH accretes persistently at the Eddington rate at constant radiative efficiency ϵ, we can estimate the time required for it to grow from an initial seed mass $M_{\rm BH}(0)$ to a mass $M_{\rm BH}(t)$:

$$\dot{M}_{\rm BH} = \frac{(1-\epsilon)}{\epsilon}\frac{4\pi G m_{\rm p}}{c\sigma_{\rm T}} M_{\rm BH}. \tag{1.12}$$

Integration of equation 1.12 yields the growth time

$$t_{\rm gr} \approx 0.45 \frac{\epsilon}{(1-\epsilon)} \ln\left(\frac{M_{\rm BH}(t)}{M_{\rm BH}(0)}\right) \text{Gyr}. \tag{1.13}$$

1.4.2 Stellar mass BHs

High redshift quasars may have formed from the BH progenitors of Pop III stars, which are expected to have typical masses of a few tens to hundreds of solar masses. Stars with masses below 9 $M_\odot$ do not have cores massive enough to collapse to a BH, but instead end their lives as white dwarfs, whereas stars between 9 - 25 $M_\odot$ end their lives as neutron stars. Stars with masses between 40 - 140$M_\odot$ and above 260 $M_\odot$ are expected to directly collapse into BHs of similar masses (Heger & Woosley, 2002; Heger et al., 2003). A summary of the fate of single stars as a function of their initial mass and metallicity is shown in Figure 1.3

A timing problem exists for the growth of light stellar mass BH seeds if they are to form the observed high-z quasars. Even in the optimistic scenario where a BH which forms at $z \sim 25$ grows persistently at the Eddington rate for its entire lifetime, equation 1.13 shows that producing a $\sim 10^9$ $M_\odot$ quasar from a typical Pop III BH remnant of 10 - 100 $M_\odot$ would require an accretion time greater than the age of the universe at $z \sim 7$.

This timing problem might be alleviated in the case of significantly lower radiative efficiencies via slim-disk accretion, in which extended periods of

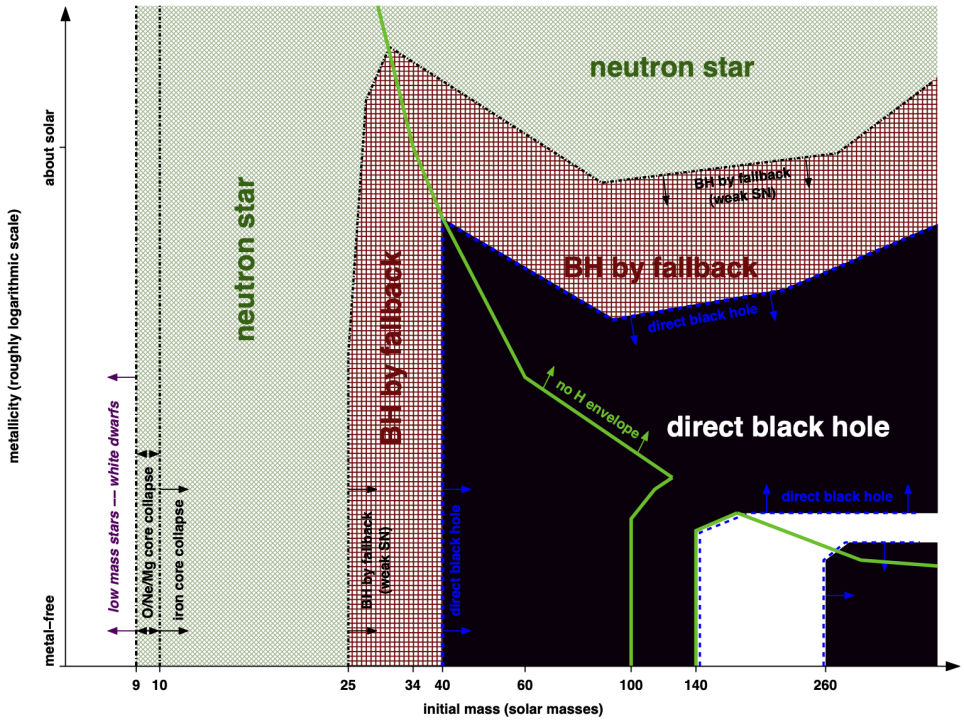

Figure 1.3: The fate of single stars as a function of their initial mass and initial metallicity. Tracks for the formation of DCBHs from the stars are highlighted in black whilst the white region in the bottom right indicates the range for a pair instability supernova. Adopted from (Heger et al., 2003)

highly super-Eddington accretion rates may be achieved, as shown in Figure 1.4 (Inayoshi et al., 2016). They found that accretion rates of up to $\sim$ 8000 $\dot{M}_{\rm E}$ are possible for BH seed masses $> 10^4$ $M_\odot$ for an ambient gas density of 10^5 cm^{-3} and temperature $\sim$ 8000 K. Photons are trapped close to the BH due to electron scattering in their 1D simulations, limiting the emergent luminosity to less than Eddington, and preventing the radiation from affecting the gas dynamics at larger scales. Furthermore, in the case of early efficient super-critical growth, it is possible to achieve a BH mass comparable to that predicted by the direct collapse scenario in a few Myr (Madau et al., 2014; Lupi et al., 2016). This is evident in Figure 1.5, where a 100 $M_\odot$ BH seed accreting intermittently at $\dot{m}/\dot{m}_{\rm E} = 3 - 4$ with a duty cycle of 0.5 reaches a mass of $\sim 10^9$ $M_\odot$ by $z \sim 8 - 9$. The accreted gas must however efficiently lose angular momentum to enable super-Eddington growth (Pezzulli et al., 2017).

Even if such modes of accretion could occur, it is not clear that the BH would encounter enough gas to become a SMBH by $z \sim 7$. Most stellar mass Pop III BHs were likely to have been "born starving" in low densities, unable to grow substantially via accretion early in the universe. This is because in higher densities the luminous stellar progenitors of the BHs emit copious ionizing radiation for a few Myr before their collapse, which would heat the surrounding gas above the virial temperature of the host dark matter halo, inhibiting collapse. Pop III BHs would then later require extended periods of super-Eddington accretion to reach 10^9 $M_\odot$ by $z \sim 7$ to overcome the low duty cycles imposed by their strong ionizing negative feedback which is able to photo-evaporate the gas in the host halo (e.g., Whalen et al., 2004; Milosavljević et al., 2009b,a; Park & Ricotti, 2011, 2012, 2013; Madau et al., 2014; Volonteri et al., 2015). Here the duty cycle is defined as the fraction of time spent accreting during the total evolutionary time of the system. Additionally, many low-mass Pop III BH seeds may also be ejected from their birth haloes, and thus their fuel supplies, by asymmetries in their core-collapse engines (Whalen & Fryer, 2012).

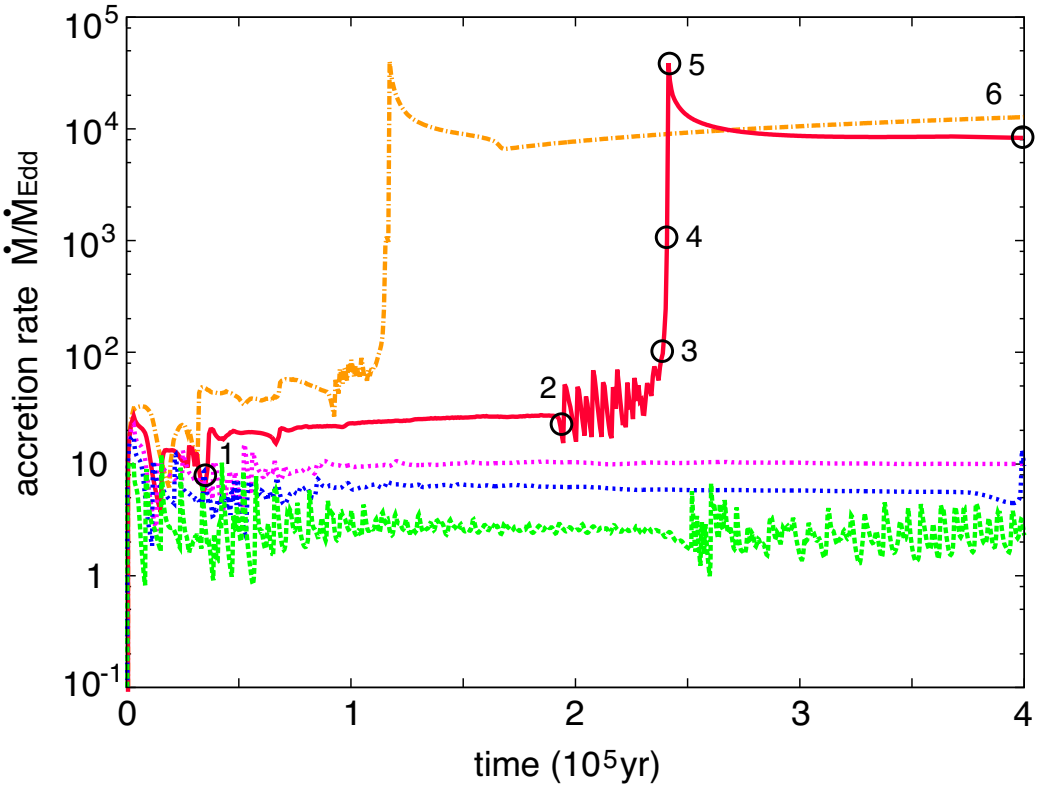

Figure 1.4: Accretion rate history for $M_{\rm BH} = 10^3$ (green long dashed), 3×10^3 (blue short dashed), 5×10^3 (magenta dotted), 10^4 (red solid), and 2×10^4 $M_\odot$(orange dot-dashed). The radiative efficiency is assumed to be $\epsilon = 3/(10 + 3\dot{m})$ (the trapping model). The density of the ambient gas is 10^5 cm^{-3}. For $M_{\rm BH} < 10^4$, the average accretion rate is limited to $\dot{m} \lesssim 10$. For higher BH mass ($M_{\rm BH} \geq 10^4$ $M_\odot$), a big jump of the accretion rate occurs and the accretion rate approaches a constant value, where $\dot{M} \simeq 8000\dot{M}_{\rm Edd}$. Adopted from Inayoshi et al. (2016).

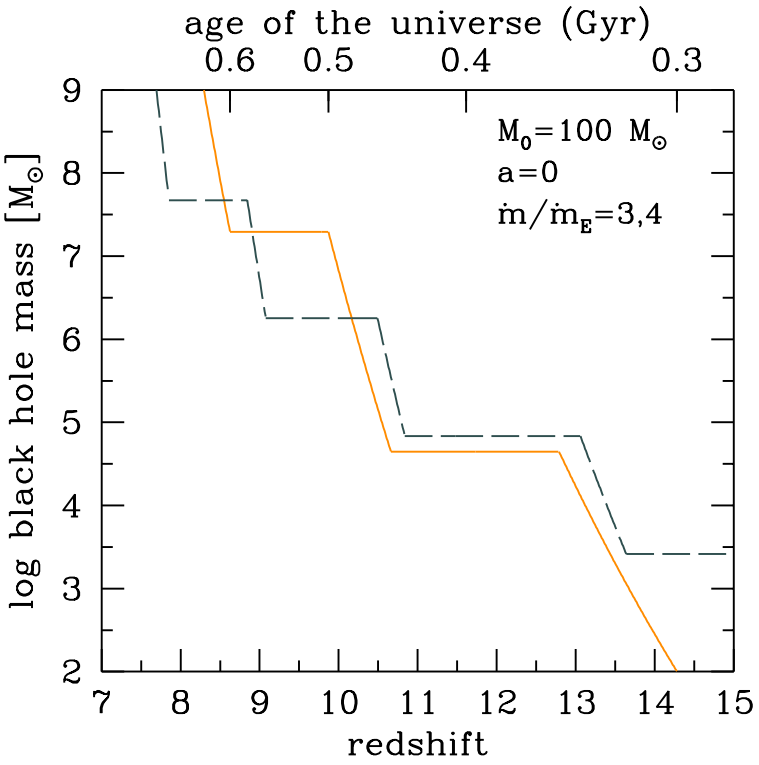

Figure 1.5: Mass assembly history of a seed, non-rotating BH with $M_0 = 100$ $M_\odot$ accreting intermittently at $\dot{m}/\dot{m}_E = 3$ with a duty cycle of 0.5 (*orange solid line*) and at $\dot{m}/\dot{m}_E = 4$ with a duty cycle of 0.2 (*gray dashed line*). In both cases the period of quiescence is 100 Myr. Adopted from Madau et al. (2014).

1.4.3 BH seeds from dense stellar clusters

The first generation of stars began to pollute the primordial Universe with the first heavy elements when they died in supernova explosions. This led to the formation of the second generation of stars known as Population II (Pop II) stars, which are metal poor and more similar to those found in our local Universe, i.e. with lower masses and longer lifetimes than Pop III stars.

As was described in section 1.3, Pop III stars tend to form as clusters in small groups, which may prohibit collisional runaway (Bromm et al., 2002; Turk et al., 2009; Stacy et al., 2010). The conditions needed to initiate the process of collisional runaway have however been observed in the local Universe, for example in the Milky Way. If this mode of star formation occurred at early enough epochs, the higher densities in the early Universe may have caused many of the stars in the cluster to strongly interact.

The two conditions required for the formation of a dense, bound star cluster are a metal enriched birth cloud and a high star formation efficiency. The first ensures that the birth cloud will fragment efficiently into a Population II star cluster with many stars. The estimated metallicity for efficient fragmentation is $Z \gtrsim 10^{-4} Z_{\odot}$ or $Z \gtrsim 10^{-6} Z_{\odot}$ in the presence of dust (Omukai et al., 2005; Schneider et al., 2012). The second criterion ensures that a bound star cluster actually forms so that collisional runaway can ensue, otherwise the stars will become unbound before they can collide or merge.

After formation of the star cluster, the massive stars sink to the center of the cluster due to dynamical friction. This increases the collision/merger probability of stars in the cluster as the cross section of these stars is much larger than their lower mass counterparts. Once a collision or merger has occurred, the cross section of the newly formed star increases thus enhancing the probability for a future collision or merger. The star with the largest cross section is most likely to dominate all subsequent collisions or mergers in the cluster, and forms a single massive star. Collisions and mergers will cease once the collision/merger time scale becomes larger than the main sequence lifetime of the massive star, which may reach a mass of up to a few 1000

$M_\odot$ (Devecchi & Volonteri, 2009; Reinoso et al., 2018; Boekholt et al., 2018). Figure 1.6 shows the time evolution of the most massive star in a recent simulation of a dense Pop III protostellar cluster for 6 different accretion models, which reaches $10^4 - 10^5$ $M_\odot$ within 40-60 crossing times. The star then evolves off the main sequence, and depending on its mass and metallicity, may directly collapse to an IMBH with minimal mass loss (Heger et al., 2003). Alternatively, if the star undergoes few collisions reaching a mass of $150 < M < 260$ $M_\odot$, it will likely result in a pair-instability supernova, whereas if it remains below 150 $M_\odot$ the star cluster evolves normally.

It is unlikely that the birth clouds in which these star clusters might form at high redshift will be observed in the near future, therefore understanding their initial conditions relies on cosmological simulations and analytic modeling. Modelling such systems numerically is challenging however due to their highly chaotic behaviour. This is compounded by the requirement to correctly model the processes of stellar evolution (single and binary, including that of a merger remnant), stellar mergers/collisions, the gas dynamics, and the gravitational effects due to the larger galaxy within which the star cluster is embedded. Current simulations can only resolve the scales needed to address these issues for single objects, limiting the ability to make general statements. It remains an open question whether these systems can accrete efficiently enough to grow SMBHs within the first billion years of the Universe. Some analytical work suggests that for star clusters with strong gas inflows, certain conditions may lead to super-Eddington growth (Alexander & Natarajan, 2014), however it is doubtful that these BHs would encounter enough gas to accrete to become SMBHs.

1.4.4 Direct collapse black holes

Another model for producing both large seed masses ($\sim 10^5 M_\odot$) and rapid accretion rates that is currently of great interest is the so-called atomically-cooled halo scenario (Bromm & Loeb, 2003; Dijkstra et al., 2008; Wise et al., 2008; Regan & Haehnelt, 2009a,b). Atomic hydrogen cooling via Lyman-

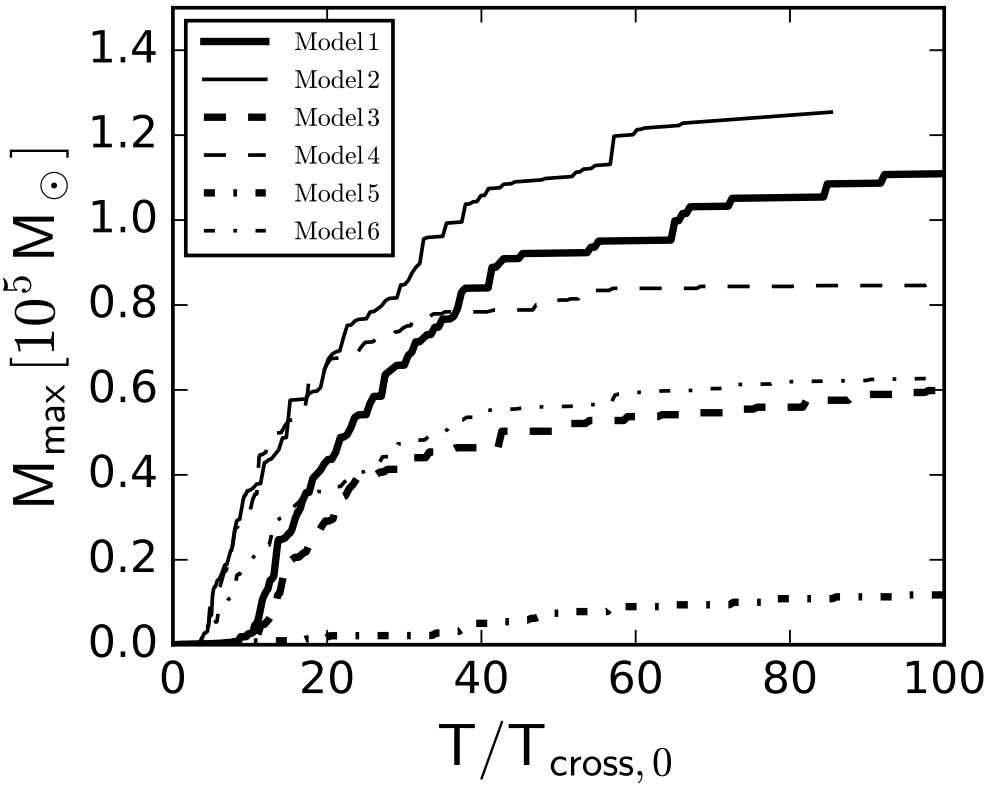

Figure 1.6: Time evolution of the maximum mass in a stellar cluster system for six different accretion models. The models vary by whether the gas reservoir is infinite or finite, and whether a position or time dependent accretion model is used. Except for Model 5, all models efficiently convert at least half of the initial gas mass into a single massive object. Adopted from Boekholt et al. (2018).

alpha lines can cool the gas in the halo down to $\sim$ 8000 K, whereas H_2 can cool the gas via rotational-vibrational transitions down to $\sim$ 200 K. Comparing the Jeans mass, M_J, of a cloud at a number density of 10^3 cm^{-3}, H_2 cooling at 200 K leads to a $M_J \sim 10^3\ M_\odot$, whereas atomic H cooling at 8000 K leads to a much larger $M_J \sim 10^5\ M_\odot$. Therefore the presence of a H_2 dissociating background LW flux $J_{\rm BG} \gtrsim 100\ J_{21}$, expected from a population of Pop III stars in the early universe, can delay the onset of cooling and fragmentation in a pristine halo and hence the formation of Pop III stars. J_{21} is the intensity of background radiation in units of 10^{-21} erg s^{-1} cm^{-2} sr^{-1} Hz^{-1}.

As explained in section 1.3, at low densities (n $< 10^8$ cm^{-3}) H_2 forms mainly via the H^- channel (Eq. 1.3). The two most important radiative reactions that can suppress the formation of H_2 in the collapsing gas are the photodissociation of H_2 and photodetachment of H^-. The LW photons $\gamma_{\rm LW}$, with energies of $11.2 \leq h\nu < 13.6$ eV, can be absorbed in the LW bands of H_2 and photo-dissociate it shortly after putting it into an excited state via the Solomon process (Omukai, 2001)

$$H_2 + \gamma_{\rm LW} \rightarrow H + H. \tag{1.14}$$

Lower energy photons with energy greater than 0.76 eV photodetach H^- via

$$H^- + \gamma_{0.76} \rightarrow H + e^-. \tag{1.15}$$

Stars emitting a hard spectrum of $T_{\rm rad} = 10^5$ K are more efficient at directly dissociating H_2, whereas stars with a softer spectrum with $T_{\rm rad} = 10^4$ K are more effective in the photodetachment of H^-.

It is important that the halo remains unpolluted by metals until it reaches the atomic-cooling regime ($> 10^7 M_\odot$), since metal contamination by supernova winds will rapidly cool the collapsing gas to a few tens of Kelvins, radiating away its thermal energy and resulting in strong fragmentation and a small Jeans mass.

Supersonic baryonic streaming motions relative to dark matter within some regions in the early universe in low mass haloes may provide another

means to suppress fragmentation and star formation in low mass haloes (Tseliakhovich & Hirata, 2010). Prior to recombination, baryons were tightly coupled to photons resulting in a standing acoustic wave pattern (Sunyaev & Zeldovich, 1970). This in turn leads to oscillations between baryons and dark matter with relative streaming velocities of around 30 km s^{-1} which decay linearly with z, and coherence lengths of 10 - 100 Mpc at $z \approx 1000$. After recombination, since baryons are no longer coupled to photons, their sound speed drops to ~ 6 kms^{-1}, which makes them supersonic with respect to the dark matter. These motions reduce the baryon overdensity, delaying the onset of cooling, leading to a larger critical mass for collapse, which can help promote the growth of a DCBH seed (Hirano et al., 2017; Schauer et al., 2017). Such motions may also collisionally dissociate H_2 molecules and avoid metal enrichment by suppressing in-situ star formation (Tanaka et al., 2013; Tanaka & Li, 2014). This mechanism may primarily act as a catalyst only within the atomically-cooled halo model however (Schauer et al., 2017), and may not occur in any given halo (Greif et al., 2011a; Stacy et al., 2011; Latif et al., 2014a) – see also (Inayoshi & Omukai, 2012; Inayoshi et al., 2015).

The halo collapses and heats up while accumulating mass until Lyman-α line cooling becomes efficient. This occurs when the virial temperature of the halo reaches $\gtrsim 10^4$ K, where the cooling function rises sharply by several orders of magnitude because the number of free electrons able to excite hydrogen greatly increases at this temperature (Spitzer, 1978). A rapid baryon collapse then ensues as the gas collapses isothermally at $\sim 10^4$ K, leading to extremely high densities at the centre of the halo and infall rates of up to $\sim$ 0.1-1 $M_\odot$/yr. Maintaining the gas temperature $\sim$ 8000 K is important for high accretion rates, as the accretion rate $\dot{M} \propto c_s^3/G \sim 0.1\ M_\odot yr^{-1}(T/8000\ K)^{3/2}$, where c_s is the thermal sound speed (Bromm & Loeb, 2003). Alternatively, high accretion rates may be achieved through highly dynamical processes such as the"bars within bars" instability (Begelman et al., 2006) or galaxy mergers (Mayer et al., 2010).

To understand the basic thermodynamical framework, the density - tem-

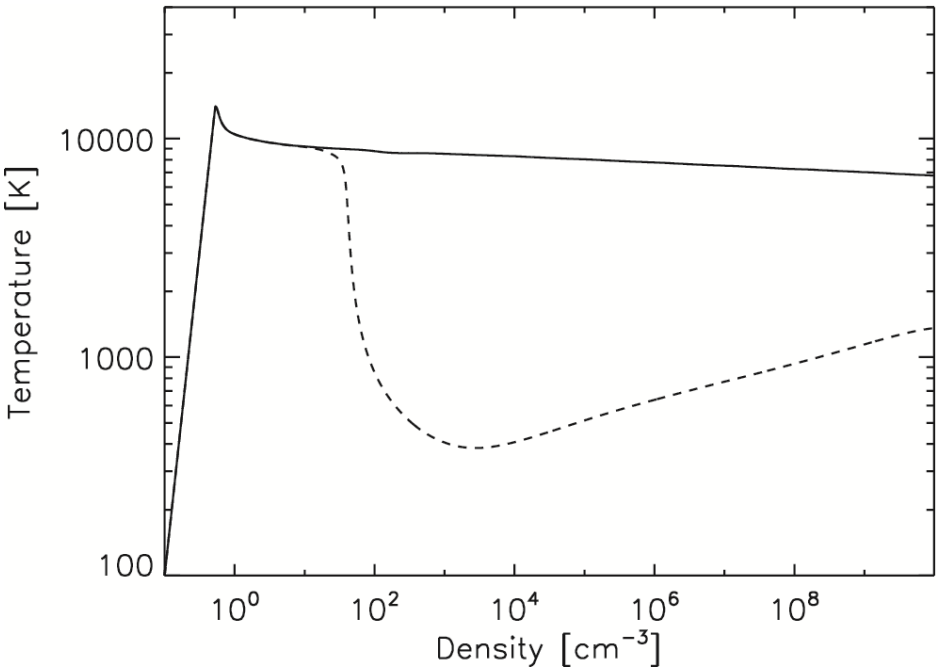

Figure 1.7: Density-temperature diagram for primordial gas collapse. Cooling via atomic H leads to a DCBH (solid), while cooling via molecular hydrogen leads to Pop. III stars (dashed). Figure taken from Agarwal et al. (2016a)

perature diagram for gas undergoing collapse and cooling via H_2 (leading to Pop III stars, dashed line) vs. cooling via H (leading to a DCBH, solid line) is shown in Figure 1.7.

At densities of 10^8 cm^{-3}, cooling due to H^- comes into play and brings the gas temperature down to 5000 K (Van Borm et al., 2014). Above 10^{16} cm^{-3}, the gas cloud becomes optically thick to both Lyman-α and H^- cooling, and the temperature starts to rise. Collisional ionization cooling becomes important and maintains the gas temperature close to 10^4 K. Eventually, at densities higher than 10^{20} cm^{-3}, the gas cloud becomes completely opaque and collapses adiabatically. The density-temperature diagram extending up to $n \sim 10^{20}$ cm^{-3} displaying the temperature evolution for collapsing primordial gas irradiated with a power-law type spectrum is shown in Figure

1.8

According to stellar evolution calculations, the high accretion rates of 0.1 - 1 $M_{\odot}$/yr lead to the formation of a metal-free supermassive star (SMS) of mass $\gtrsim 10^4$ $M_{\odot}$ which will later undergo runaway collapse through a general relativistic instability due to the relativistic contribution of thermal photons to gravity in the core of the star, leaving behind a massive DCBH that can retain up to 90% of its Jeans mass and reach 10^4 - 10^6 $M_{\odot}$ (Hosokawa et al., 2013; Umeda et al., 2016; Woods et al., 2017; Agarwal et al., 2016a; Regan et al., 2017). Alternatively, the SMS may evolve towards a zero age main sequence (ZAMS) hydrogen fusing star and later collapse into a SMBH (Ferrara et al., 2014). Under accretion rates of $\gtrsim$ 0.1 $M_{\odot}$/yr, the radius of the star monotonically increases with mass due to the shorter accretion time compared with the Kelvin-Helmholtz contraction timescale (Hosokawa et al., 2013). Consequently, the star's surface temperature remains as low as 5000 K and they produce weak UV stellar feedback. The Kelvin-Helmholtz contraction timescale refers to the time required for a star to radiate away its gravitational binding energy at a given luminosity, if its nuclear energy sources were completely turned off.

A sub-class of DCBH models envisages the formation of an intermediate stage known as a quasi-star, in which the 'star' is powered by the accretion of a massive envelope onto a central BH seed (Begelman et al., 2008). It forms due to the fact that the accretion timescale is considerably shorter than the nuclear burning timescale and therefore the core collapses into a BH. In such an object gas may accrete onto the central BH at super-Eddington rates, however the overall accretion is limited by the Eddington rate of a quasi-star.

In addition to the LW background, an intense burst of LW radiation from a neighbouring star-bursting proto-galaxy, just before the gas cloud undergoes gravitational collapse, is required to fully suppress star formation. The global background radiation field is sufficient to delay star formation but will not entirely prevent the formation of H_2 as the halo mass increases. For

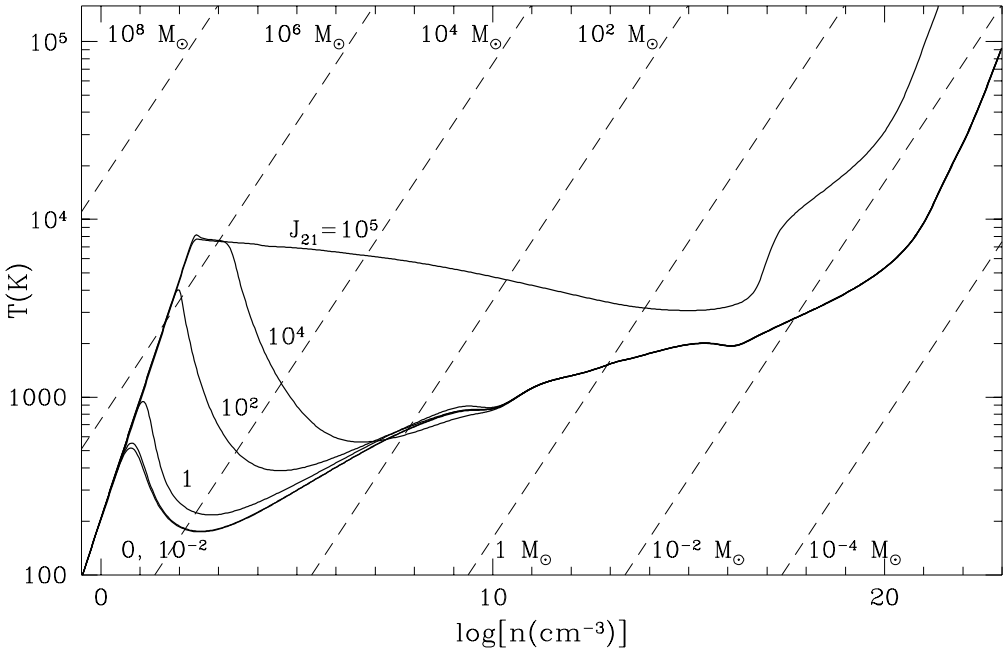

Figure 1.8: Density-temperature diagram for the collapse of primordial gas irradiated by Far UV radiation ($h\nu < 13.6$ eV). The evolutionary tracks are drawn for various values of J_{21}, where the highest value corresponds to the atomically cooling track. The dashed lines indicate a constant Jeans mass. Taken from (Omukai, 2001).

instance, detailed studies (Shang et al., 2010; Latif et al., 2014b) have shown that in the presence of a LW background, only the molecular hydrogen in the outer regions of minihaloes is dissociated and a considerable fraction of molecular hydrogen (0.001) still exists in the central region of the haloes. In order to completely suppress Pop III star formation, it is essential to lower the H_2 fraction to 10^{-8} which can be achieved by extremely high values of the LW specific intensity.

Photo-evaporation from photons with $E > 13.6$ eV due to neighbouring star-bursting haloes can limit the time available for creating a pristine atomic cooling halo using a nearby neighbour. Therefore, in order to form an atomic cooling halo, the atomically cooling and star-bursting halo need to be sufficiently close together and tightly synchronised in time. Regan et al. (2017) define the synchronisation time as the time between when the star-burst galaxy is turned on and when the gas in the atomically cooling halo would have collapsed to form a Pop III star in the absence of the star-burst galaxy. Short synchronisation times reduce the probability of metal pollution and/or photo-evaporation from the star-burst galaxy. An illustration of the synchronised haloes scenario is shown in Figure 1.9.

The critical value for the flux in the LW bands $J_{\rm crit}$, required for the complete quenching of H_2, is determined by the shape of the radiation spectrum. The value of $J_{\rm crit}$ is thus the key quantity that controls the efficiency of the DCBH formation process, and sets the threshold above which a halo with $T_{\rm vir} > 10^4$ K can directly collapse to an SMBH seed (Agarwal et al., 2016a). Below this value, the gas is susceptible to fragmentation due to efficient H_2 cooling and the mass infall rates towards the centre are generally lower.

The values for $J_{\rm crit}$ quoted in the literature span several orders of magnitude (see e.g. Table 1 in Agarwal et al., 2016a), ranging from $J_{\rm crit} = 0.5\ J_{21}$ (Agarwal & Khochfar, 2015) up to $\sim 10^5\ J_{21}$ (Omukai, 2001). There are most likely a distribution of critical values depending on e.g. the spectral shape of the stellar population (Shang et al., 2010), the anisotropy of the illuminating flux (Regan et al., 2014), the treatment of H_2 self-shielding (Wolcott-Green

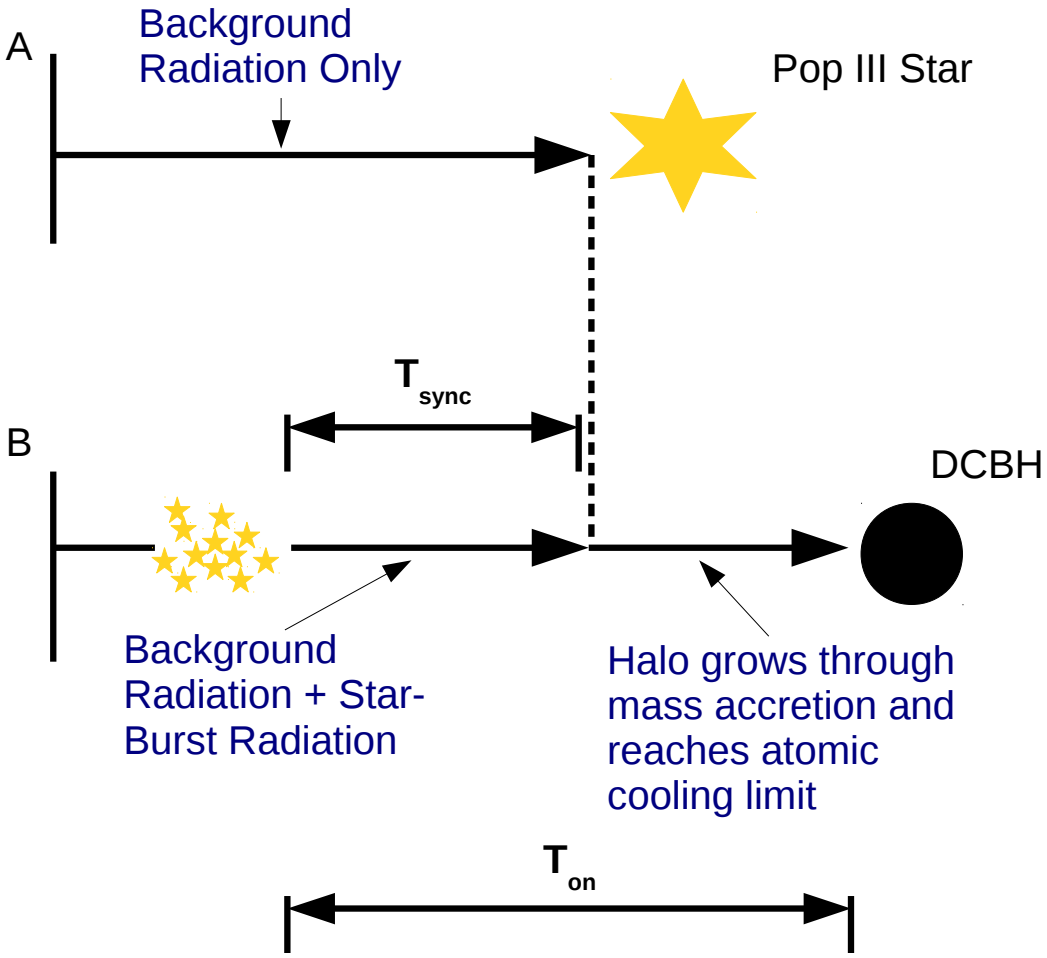

Figure 1.9: The synchronised haloes scenario. In case A, with only a background LW radiation field, a (delayed) Pop III star forms due to H_2 cooling. In case B, a DCBH can form in an atomically cooling halo if a nearby star-burst galaxy and the radiation background provide the critical LW flux required. T_{sync} is defined as the time between the star-burst turning on and the point at which a Pop III would have formed. T_{on} is the time taken for an atomic cooling halo to collapse and form a DCBH (or the minimum time the source must shine for). Adopted from Regan et al. (2017).

et al., 2011), the details of the chemistry model (Glover, 2015), and the star formation history (Agarwal et al., 2016b). Current estimates for $J_{\rm crit}$ are at least an order of magnitude higher than the mean background, which implies that direct collapse sites will preferentially be found close to the first galaxies (Agarwal et al., 2012). However, any theoretical model that attempts to explore the abundance of such sites is extremely sensitive to the choice of $J_{\rm crit}$. For example, an order of magnitude increase in $J_{\rm crit}$ can reduce the DCBH number density at $z = 6$ by three orders of magnitude (Dijkstra et al., 2008; Latif et al., 2014b). This emphasizes the need to understand and calculate the value of $J_{\rm crit}$ produced by galaxies composed of Pop III stars in the early Universe.

DCBHs have the ability to grow at much higher rates than Pop III stellar mass BH seeds. This is because they are born with much larger masses and in much higher densities in host galaxies whose deep potential wells mean they can retain their fuel supply, even when heated by X-rays. Moreover, cosmological hydrodynamical simulations starting from first principles show that metal ejection preferentially occurs in the low density regime (Ritter et al., 2015; Pallottini et al., 2014) and neighboring haloes in higher densities may remain metal free, enabling them to reach the atomic cooling track. To reach $10^9\ M_\odot$ by $z \sim 7$, SMBH seeds must be fueled for long times, either by a succession of mergers with other gas-rich haloes (e.g., Li et al., 2007) or by unusually strong cold accretion flows, like those thought to drive rapid star formation in some galaxies at later epochs (e.g., Dekel & Birnboim, 2006; Dekel et al., 2009; Bournaud et al., 2011). There may be up to a few dozen regions per Gpc^3 with cold flows capable of forming quasars by $z \gtrsim 7$ (Di Matteo et al. 2012; Feng et al. 2014a; see also Costa et al. 2014a; Hirschmann et al. 2014).

After birth, X-rays from the nascent BH regulate its growth by heating and ionizing flows in its environment and photoevaporating cold streams outside the halo. Winds, ionizing UV and supernovae explosions (SNe) from stars later perturb flows onto the BH, either promoting or suppressing its

growth (see, e.g., Dubois et al., 2015; Habouzit et al., 2017). Stars also govern their own rates of formation because their ionizing UV can trigger or quench star formation in nearby clouds (O'Shea et al., 2005; Whalen et al., 2008a, 2010). Metals from SNe also cool gas, facilitating the formation of new stars (Kitayama & Yoshida, 2005; Whalen et al., 2008b; Ritter et al., 2012; Safranek-Shrader et al., 2014; Smith et al., 2015b; Ritter et al., 2016; Sluder et al., 2016; Chen et al., 2017a,b).

Radiation from the BH can also promote or suppress star formation in its vicinity (Machacek et al., 2003; Aykutalp et al., 2014). X-rays produce energetic photoelectrons that cause secondary ionizations that enhance free electron fractions in primordial gas. Free electrons in turn catalyze the formation of H_2 via the H^- channel, cooling and collapsing gas and creating more stars (e.g., Glover & Abel, 2008). On the other hand, radiation from the BH can also evaporate star-forming clouds and global LW backgrounds can destroy H_2, quenching star formation.

1.4.5 DCBH observational signatures

Newly formed massive BHs are thought to rapidly acquire an accompanying stellar component, mostly from mergers with the nearby star forming haloes which provided the required LW flux to enable direct collapse of a primordial gas cloud into a massive BH. The mass of the BH is initially large compared to its accompanying stellar mass and these galaxies, at least initially, do not obey the locally observed relation that the central BH mass of a galaxy corresponds to $\sim 0.1\%$ of its stellar mass (in the bulge). This initial stage, during which the BH is overly massive, has been referred to as the 'Obese Black Hole Galaxy' (OBG) stage (Agarwal et al., 2013). Seeding models for the formation of an OBG and a Pop III star BH are shown in Figure 1.10. Natarajan et al. (2017) provide several observational diagnostics which may help us identify galaxies in their OBG stage, including: (i) a large bolometric luminosity ($L_{\rm bol} \gtrsim 10^{44}$ erg s^{-1}, which corresponds to the Eddington luminosity of a black hole of mass $M_{BH} \sim 10^6\ M_\odot$), (ii) a large ratio of X-ray

to optical flux, and (iii) particular colors in the *James Webb Space Telescope* (*JWST*) bands.

The 'unprocessed' spectrum emitted from the BH consists of a disk and a hot coronal component. Reprocessing of ionizing radiation in the atomic hydrogen gas surrounding the accreting BH gives rise to strong recombination lines. High-energy UV ($E \gtrsim 55.4$ eV) and X-ray photons can doubly ionize Helium. Recombining doubly ionized Helium produces strong He1640 line emission. The strongest line that is produced however, is H Lyα, which can account for as much as $\sim 40\%$ of the bolometric luminosity of the accreting BH (see e.g. Dijkstra et al., 2016b).

The recombination lines contain large fluxes, but condensed into narrow spectral ranges, which can make them more easily detectable. At higher redshifts, the Lyα line redshifts into the NIR where the line is better accessible from space than from ground-based telescopes, as atmospheric OH lines contaminate ground-based observations. The Wide Field Infrared Survey Telescope (*WFIRST*) and *EUCLID* may have the sensitivity to directly detect line emission from the most massive BH seeds, and will provide interesting targets which can then be followed-up spectroscopically with e.g. NIRSpec on *JWST* and the next generation of ground-based facilities such as the *European Extremely Large Telescope* (*E-ELT*). Because *JWST* and future ground-based facilities are expected to operate deeper into the IR, they can access other redshifted hydrogen lines such as the Hα line which is expected to be a factor of ~ 8 times weaker when powered by recombination.

Another unique signature that is associated with the formation of DCBHs was discussed in Dijkstra et al. (2016a): the physical conditions that enable direct collapse: (i) the collapse of pristine gas, (ii) the (virtual) absence of H_2, (iii) the large column densities of HI gas, and (iv) suppressed fragmentation, provide optimal conditions for Lyα trapping, which can cause Lyα photons to scatter $\gtrsim 10^8 - 10^9$ times. Under these conditions the 2p level (which is the only level of atomic H excited by Lyα absorption) can be overpopulated with respect to the 2s level, and give rise to stimulated fine-structure emission with

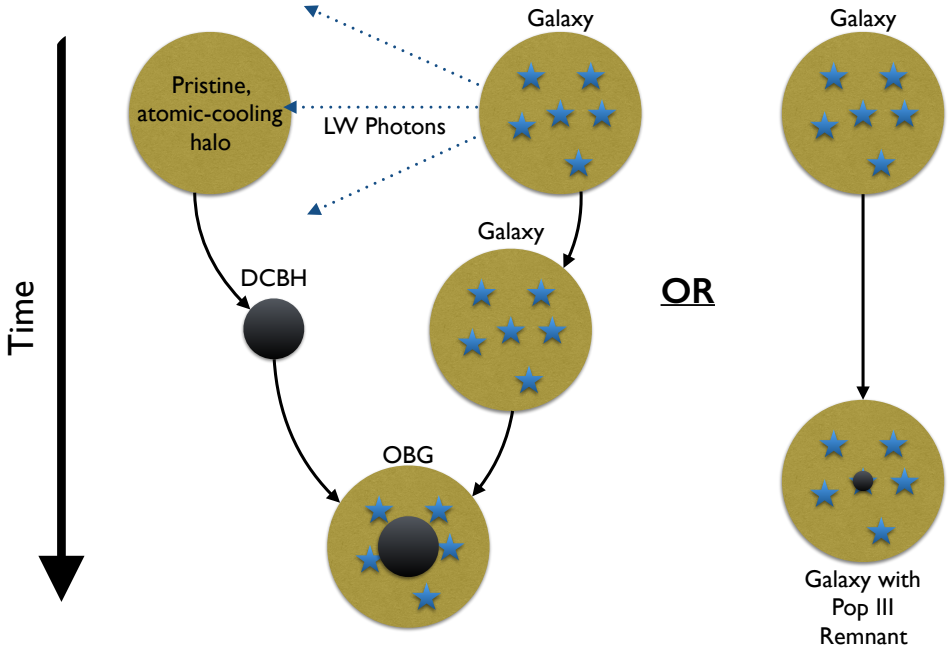

Figure 1.10: Left panel: formation of on OBG when a DCBH seed merges with its parent star forming halo. Star formation is quenched in the DCBH host halo due to LW photons from the neighbouring SF halo. However, a stellar component is accrued promptly via merging with the parent SF galaxy leading to the formation of an OBG. Right panel: sequence for a growing Pop III remnant BH seed. Adopted from Natarajan et al. (2017).

a rest-frame wavelength of 3.04 cm (Field & Partridge, 1961). This line has a broad peculiar spectral shape that makes it easy to distinguish from other lines. Dijkstra et al. (2016a) showed that gas clouds directly collapsing into massive BHs could amplify the background CMB at a level that is detectable with the *Square Kilometer Array* 1 mid-frequency instrument, which would provide a smoking-gun signature for DCBHs.

1.5 Overview

To model the formation of a primordial quasar, simulations must resolve all the complex physical processes described above deep in the host galaxy of the BH up to the scale of the cold streams in the IGM feeding its growth. These scales have now been bridged, as will be presented in later chapters, with new cosmological simulations that include X-rays from the BH and winds, ionizing UV and SNe feedback from star-forming regions, and evolve a quasar in cold flows from birth at $z \sim 20$ down to $z = 6$.

The upcoming launch of next-generation observatories such as *JWST* and *Euclid*, as well as ground-based extremely large telescopes such as *E-ELT*, promise to yield great insights into the nature and number of the most luminous objects in the early Universe. Already, observational case studies such as the Lyman-α emitter and DCBH candidate CR7 at $z = 6.6$ have provided invaluable tests for our ability to distinguish between models for luminous high-z objects (Sobral et al., 2015; Pallottini et al., 2015; Hartwig et al., 2016; Agarwal et al., 2017; Bowler et al., 2017; Pacucci et al., 2017). The ongoing search for intermediate-mass black holes (IMBHs) in the nearby Universe may soon allow us to constrain the distribution of BH seed masses (Mezcua, 2017).

With this in mind, it is clear that realistic predictions for the observational signatures of the earliest quasars, including their births, with upcoming observatories are required in order to test and constrain models for their formation and evolution. Such predictions will inform survey strategies, influence

telescope instrumental designs to maximise the chances of detection, and can provide a fingerprint to help observers identify such objects and distinguish them from other bodies. Spectral synthesis codes require the detailed physical conditions inside and surrounding the halo hosting the quasar to produce spectra. These can currently only be obtained through numerical means, and in our case through accurate multiphysics radiation-hydrodynamics cosmology codes. The results of such codes will be presented in later chapters, including synthetic source frame spectra of the quasar or SMS, from which we can calculate AB magnitudes for these objects for various filters and telescopes at various source redshifts.

In chapter 2 we describe in detail the computational tools used to simulate a SMS accretion envelope and the birth and growth of a DCBH. We also discuss the code used to post-process the simulations in order to generate realistic synthetic emitted spectra from these objects. In chapter 3, we present the modelling of red cool SMSs and predict their observational signatures in the near infrared for various source redshifts. In chapter 4, we present work on modelling hot blue SMSs with emitted SEDs modified by their stellar atmospheres, and their observational signatures in the near infrared. In chapter 5, we present the simulation of a DCBH in its cosmological environment, and discuss its observable signatures in the near infrared at birth at different source redshifts. Finally, we present our conclusions in chapter 6 and suggest ideas for future work.

Chapter 2

Numerical Simulations

In this chapter we describe the code used to simulate the formation and growth of a SMBH within its cosmological environment. We also use the same code to model the evolution of the accretion envelope surrounding a primordial SMS around $z \sim 17$. The code used to post-process these simulations to predict realistic source frame synthetic spectra for these objects will also be described, including porting data between the two codes. The procedure for initializing a cosmological simulation and finding a candidate halo for a SMBH is described, and also how a source frame spectrum is redshifted and geometrically diluted into the observer frame.

2.1 Enzo

2.1.1 Numerical methods and physics

We use the adaptive mesh refinement (AMR) radiation-hydrodynamics code Enzo (Bryan et al., 2014) with the MORAY radiation transport algorithm (Wise & Abel, 2011). The code uses comoving coordinates and includes the following physics: self-gravity, radiative cooling, chemistry, heat conduction, collisionless fluids, magnetohydrodynamics, radiation transport, and star formation, in addition to other physical effects.

Enzo has been parallelized for distributed memory platforms using the

message passing interface (MPI), in order to take advantage of the high-performance computing (HPC) clusters available today with thousands of compute cores and several gigabytes of memory per core. Enzo is executed using the PBS job scheduler through submitting a batch job script, in which the number of cores, nodes, and execution time must be specified, and which are determined by the requirements of the simulation, i.e. the physics we wish to include and the numerical resolution we wish to attain. The job is queued and will be executed once sufficient resources become available on the HPC cluster.

Enzo models baryonic matter as a fluid using an Eulerian grid-based hydrodynamic solver called the piecewise parabolic method (PPM), which is spatially third-order accurate and uses a nonlinear Riemann solver for shock capturing. In contrast to static Euclerian solvers, Enzo can adaptively add and modify additional, finer meshes ("grids") over regions that require higher resolution. Collisionless matter, including dark matter and stars, is modelled with particles that interact with the baryons only via gravity. MORAY is a photon-conserving radiative transfer algorithm that is based on an adaptive ray-tracing method utilizing the HEALPix pixelization of a sphere (Abel & Wandelt, 2002). Photons are integrated outward from sources using an adaptive timestepping scheme that preserves accuracy in ionization fronts even in the optically-thin limit. This has been coupled to the chemistry and cooling network to provide ionization and heating rates on a cell-by-cell basis.

X-ray and ionizing UV transport in MORAY includes radiation pressure on gas due to photoionizations and is self-consistently coupled to hydrodynamics and nine-species nonequilibrium primordial gas chemistry (H, H+, He, He+, He++, e-, H-, H_2, H_2^+) in Enzo. Secondary ionizations due to energetic photoelectrons and Compton heating by X-rays (where X-ray photons scatter inelastically off of electrons thereby transferring energy to them) are taken into account in the chemistry and energy equations along with the usual primordial gas cooling processes: collisional excitational (free electron impact knocks a bound electron to an excited state; it decays, emitting a

photon, also known as bound-bound emission) and collisional ionizational (free electron impact ionizes a formerly bound electron, taking energy from the free electron) cooling by H and He, recombinational cooling (free electron recombines with an ion; the binding energy and the free electron's kinetic energy is radiated away, also known as free-bound emission), bremsstrahlung cooling (or free-free emission, where a free electron is accelerated by an ion, emitting a photon), H_2 cooling, and inverse Compton cooling by the cosmic microwave background (where CMB photons are scattered to higher energies due to collisions with energetic electrons, resulting in the Sunyaev-Zel'dovich effect). Note that the processes responsible for cooling the gas depend on the gas temperature, as well as the density and metallicity.

2.1.2 Physical Equations

Enzo solves the Eulerian equations of ideal magnetohydrodynamics (MHD) including gravity, in a coordinate system comoving with the cosmological expansion. In our case, we work in the purely hydrodynamic limit with no magnetic field to reduce numerical complexity (although we will include magnetic fields in future work), thus the equations are:

$$\frac{\partial \rho}{\partial t} + \frac{1}{a}\boldsymbol{\nabla} \cdot (\rho \mathbf{v}) = 0, \tag{2.1}$$

$$\frac{\partial \rho \mathbf{v}}{\partial t} + \frac{1}{a}\boldsymbol{\nabla} \cdot (\rho \mathbf{v}\mathbf{v} + \mathbf{I}p^*) = -\frac{\dot{a}}{a}\rho \mathbf{v} - \frac{1}{a}\rho \boldsymbol{\nabla}\phi, \tag{2.2}$$

$$\frac{\partial E}{\partial t} + \frac{1}{a}\boldsymbol{\nabla} \cdot [(E + p^*)\mathbf{v}] = -\frac{\dot{a}}{a}(2E) - \frac{\rho}{a}\mathbf{v} \cdot \boldsymbol{\nabla}\phi - \Lambda + \Gamma + \frac{1}{a^2}\boldsymbol{\nabla} \cdot \mathbf{F}_{\mathrm{cond}}. \tag{2.3}$$

In these equations, E, ρ, and $\mathbf{v}$ are the comoving total fluid energy density, comoving gas density, and peculiar velocity, respectively. The matrix $\mathbf{I}$ is the identity matrix, and a is the cosmological expansion parameter. The first equation represents conservation of mass, the second conservation of momentum, and the third conservation of total (kinetic plus thermal) fluid

energy. Terms representing radiative cooling (Λ) and heating (Γ) enter on the right-hand side of the energy equation (2.3), as does the flux due to thermal heat conduction ($\mathbf{F}_{\rm cond}$).

The comoving total fluid energy density E is given by

$$E = e + \frac{\rho v^2}{2}, \tag{2.4}$$

where e is the comoving thermal energy density. The equations are closed by an equation of state and Poisson's equation for the gravitational potential ϕ:

$$e = \frac{p}{(\gamma - 1)}, \tag{2.5}$$

$$\nabla^2\phi = \frac{4\pi G}{a}\left(\rho_{\rm total} - \rho_0\right) \tag{2.6}$$

The equation of state is shown here for an ideal gas with a ratio of specific heats γ . The gravitational potential ϕ is sourced by the total mass density contrast, where $\rho_{\rm total} = \rho_{\rm gas} + \rho_{\rm dm} + \rho_{\rm stars}$ and ρ_0 is the mean density.

The expansion parameter $a \equiv 1/(1+z)$ follows the expansion of a smooth, homogeneous background, where z, the redshift, is a function only of t. All spatial derivatives are determined with respect to the comoving position $\mathbf{x}$, which removes the universal expansion from the coordinate system. The evolution of $a(t)$ is governed by the second Friedmann equation for the expansion of a spatially homogeneous and isotropic Universe

$$\frac{\ddot{a}}{a} = -\frac{4\pi G}{3a^3}(\rho_0 + 3p_0/c^2) + \Lambda_c c^2/3. \tag{2.7}$$

Here ρ_0 is the mean comoving mass density (including both baryonic and dark matter), p_0 is the comoving background pressure contribution, and Λ_c is the cosmological constant. This system of equations is limited to the non-relativistic regime and assumes that curvature effects are not important - both assumptions are reasonable as long as the size of the simulated region is small compared to the radius of curvature and the Hubble length c/H, where c is the speed of light and $H = \dot{a}/a$ is the Hubble constant.

Any collisionless components including dark matter, stars and BHs, are modelled as N-body particles whose dynamics are governed by Newton's

equations in comoving coordinates, and contribute to the gravitational potential through Poisson's equation. Additionally, Enzo can solve the mass conservation equations for a set of up to 12 chemical species (H, H+, He, He+, He++, e-, H-, H_2, H_2^+, HD, D, D^+) and their reactions, where destruction/creation rates due to photoionizations and/or photodissociations are tracked. Lastly, Enzo can also track the advection of one or more comoving metal density fields, which can contribute to the radiative cooling and star formation processes.

2.1.3 Simulation box size

When setting up an Enzo simulation, the size of the simulation box must be chosen carefully in order for it to contain sufficient mass to form the type of objects of interest. For instance, in order to form a SMBH on the order of 10^9 $M_\odot$ by redshift 6, we need a halo that can reach 10^8 $M_\odot$ i.e. the mass threshold for atomic cooling to take place, by redshifts ~ 20. This requires the total mass of the cosmological box to be about 1000 times larger than the atomic cooling mass threshold, since only a small percentage of the initial mass can form massive haloes by such redshifts.

Additionally, the halo mass should be less than the mass within a fraction of 0.2^3 of the box volume. This corresponds to the extent of finer nested grids that are implemented when generating initial conditions, which due to memory limitations cannot be extended to the entire box. This ensures that the SMBH host halo lies entirely within the region with the highest dark matter (DM) particle resolution (i.e. lowest mass DM particles), so that it is comprised of sufficiently many particles for a halo finder to locate it.

2.1.4 Random seed sifting

To launch a simulation we first require appropriate initial conditions for it to start from. The simulation must start from a redshift at which the Universe was still described by the linear matter power spectrum, i.e. in which

the matter fluctuations were still gaussian in distribution, which is no longer the case at late times when bound structures begin to form under gravitational collapse. A redshift of 200 was chosen as the starting point to ensure that this condition applies. The grid is initialized with gaussian primordial density fluctuations at $z = 200$ using the cosmological initial condition code for a hierarchical set of nested regions MUSIC (Hahn & Abel, 2011), with cosmological parameters taken from the second-year *Planck* best fit lowP+lensing+BAO+JLA+H_0: $\Omega_M = 0.308$, $\Omega_\Lambda = 0.691$, $\Omega_b = 0.0223$, $h = 0.677$, $\sigma_8 = 0.816$, and $n = 0.968$ (Planck Collaboration et al., 2016).

In order to generate the initial conditions a set of random seeds, i.e. integers, must be specified in the MUSIC input file, amongst other quantities such as the number of nested grids and their extent over the simulation box. Changing a single digit in the random seeds changes the initial conditions, and hence alters the entire course of the simulation.

Given that there are only about a dozen regions in the Universe per cubic Gpc with reservoirs capable of sustaining rapid quasar growth in the manner which might lead to the formation of a 10^9 $M_\odot$ SMBH by $z \sim 6$, no single 100 Mpc on a side box chosen at random would be expected to enclose one. With this box size (justified in section 2.1.5 for quasar simulations), it is therefore necessary to perform a random seed search to test multiple sets of random seeds at lower resolution until a halo is obtained that exceeds 10^{12} $M_\odot$ by $z \sim 7$ and was the product of at most a few major mergers, i.e., with other haloes similar in mass to the host halo (Trenti et al., 2008).

This was accomplished by running dark matter only runs with no nested grids down to $z = 7$, and then using the HOP halo finder run in parallel on multiple cores on the HPC cluster to speed up the computation time. The HOP algorithm works by estimating the local density at each DM particle using a smoothing kernel. It then builds chains of linked particles by 'hopping' from one particle to its densest neighbour. A particle which is its own densest neighbour is the end of the chain. All chains that share the same densest particle are then grouped together, where groups are included, linked

together, or discarded depending on an over-density threshold value of 140 times the mean density. The halo finder returns the coordinates of the halo centre, the coordinates of the maximum density, the halo radius, and the total mass of the haloes which it is able to find. Once the desired halo was located at $z = 7$, the simulation was restarted at $z = 200$ using the same initial conditions, but with nested grids centred on the coordinates of the 10^{12} $M_{\odot}$ halo at $z = 7$, and run again down to $z = 7$ to ensure that the same halo does indeed still lie within the nested grids. Snapshots from the simulation at regular redshift intervals can also be outputted and running the halo finder on them enables the growth and merger history of the halo to be traced.

2.1.5 Quasar simulation

This subsection describes the Enzo simulation performed by (Smidt et al., 2018) which was post-processed to calculate observational signatures for a DCBH at birth in chapter 5.

In order to simulate a quasar from birth down to $z \sim 6$, the box size must be large enough to enclose the cold flows feeding the quasar on cosmological scales whilst also resolving gas flows, photoionization and star formation deep within its host galaxy. These sub-galactic scale phenomena also depend upon the AMR hierarchy refinement parameters, which must be specified by the user. Enabling a higher maximum refinement level increases the spatial resolution in regions where the gas collapses at small scales. This means that the hydro solver accuracy will be increased, however it also has significant implications on the computing resources required, hence a careful compromise must be sought between accuracy and execution time. Given these considerations, the box size was chosen to be 100 h^{-1} Mpc (comoving) on a side, with a 256^3 root grid and three nested 25 h^{-1} Mpc grids that are centered on the host halo for an effective resolution of 2048^3. These grids yield an initial dark matter particle resolution of 8.41×10^6 h^{-1} $M_{\odot}$.

Having performed the random seed search described in section 2.1.4 to

obtain a halo which is capable of hosting a 10^9 $M_\odot$ quasar by $z = 6$, and confirmed that it grows mainly via accretion and mergers only with low mass haloes, we must find the point in time at which the halo crosses the atomic cooling threshold ($\sim 10^8$ $M_\odot$), expected around $z \sim 20 - 18$, and begins to cool and collapse. In nature, the halo collapse proceeds rapidly, leading to the formation of a supermassive star which only survives for a few Myr and then collapses to a SMBH. We use the HOP halo finder to determine when the most massive halo near the centre of the simulation box first reaches 10^8 $M_\odot$ or as close to this mass as we are able to find, since it may struggle to find haloes at high redshift when they are comprised of relatively few DM particles. Once the atomically cooling halo is identified, we use the yt Python package method "find max" to find the coordinates of the maximum density within it, which is usually close to the centre of mass of the halo, and insert a BH sink particle (i.e. a modified star particle) at those coordinates. The BH sink particle has an initial mass of 10^5 $M_\odot$, i.e. the mass expected of typical DCBH seeds. Enzo tracks the accretion rate onto it and tallies this onto the mass of the particle.

At this point additional Enzo physics is enabled, including BH feedback via X-ray emission. The bolometric luminosity of the BH is calculated using $L_\mathrm{r} = \epsilon_\mathrm{r} \dot{m}_\mathrm{BH} c^2$, where ϵ_r, the mean radiative efficiency, is taken to be 0.1, and $\dot{m}_\mathrm{BH}$ is the accretion rate onto the BH. This luminosity is all in the form of 1 keV photons to maximize the heating of gas because at higher energies they have smaller ionization cross sections and at lower energies they deposit less energy per ionization (Xu et al., 2014; Hummel et al., 2016). This energy is also consistent with new observations showing 90% of the X-ray flux of J1120 , a 2×10^9 $M_\odot$ BH at $z = 7.1$, to be at 0.5 - 2 keV (Nanni et al., 2017).

Since our simulations are unable to resolve the accretion disk around the BH we use an alpha disk model to compute accretion rates to approximate angular momentum transport out of the disk on subgrid scales (DeBuhr et al., 2010). This model estimates the accretion rate onto the BH from the

surrounding gas, due to viscous transport of angular momentum, using

$$\dot{M}_{vis} = 3\pi\alpha\Sigma\frac{c_s^2}{\Omega}\,, \tag{2.8}$$

where Σ is the mean surface density of the gas in the disk, Ω is its angular rotational frequency, c_s is the sound speed, and the free parameter α is the dimensionless viscosity, which takes a fiducial value of 0.05. We use this rather than standard spherically symmetric Bondi-Hoyle accretion (Bondi & Hoyle, 1944) which assumes that the BH's impact on its host galaxy can be approximated by depositing thermal energy released by accretion back into the surrounding gas. This however would require that the gas fuelling the central BH has very little angular momentum, which isn't necessarily true in gas-rich rotationally supported disc galaxies, and the dominant form of feedback for the majority of the gas in an AGN host galaxy is expected to be momentum injection (radiation pressure) rather than energy injection (heating). We also approximate a disk wind by depositing $10^{-4}\ L_r$ as thermal energy above and below the midplane of the BH perpendicular to its angular momentum vector (Ciotti et al., 2009).

The formation of star particles is also permitted, which can provide feedback through the emission of UV photons. We use a stochastic prescription for star formation that is based on Cen & Ostriker (1992) (hereafter CO92) but is slightly modified to accommodate a minimum star particle mass to avoid having too many low-mass particles (section 8.2.2 of Bryan et al., 2014). The algorithm tallies the mass accumulated in a region until it exceeds the minimum star particle mass, at which point it creates a star particle there if the conditions for star formation in CO92 have also been met. This accumulated mass exceeds the minimum mass at random times so particles are formed sporadically. Furthermore, the particles will have a range of masses because the CO92 criteria might not be satisfied when the accumulated mass in a region exceeds the minimum mass, so it will grow in mass until they are met. We adopt a minimum star particle mass of $10^7\ M_\odot$.

Star particles are assigned a Salpeter initial mass function (IMF) for simplicity and are tagged as sources of ionizing UV photons, which are prop-

agated throughout the simulation box by MORAY. Each particle emits photons at four energies: 12.6 eV (LW photons), 21.62 eV (the average energy of UV photons from massive, low-metallicity stars), 30 eV (He I ionizing photons), and 60 eV (He II ionizing photons). The relative numbers of photons apportioned to these bins was determined from the time averaged fits for the zero metallicity, no mass-loss tracks in Table 6 of Schaerer (2002). The particles also deposit momentum and metals from stellar winds into the ISM over their lifetimes. SN feedback is modeled as thermal energy, with 10^{51} erg deposited per explosion assuming one SN per 200 $M_{\odot}$ of stars formed. Cooling by metals from SNe is included with rates from Glover & Jappsen (2007), assuming solar yields that are consistent with our chosen IMF. Our models also have a uniform Lyman-Werner background due to early stars that evolves with redshift.

The simulation is run down to a final redshift of 6, at which point the Universe becomes fully ionized, whose effect on the cold streams is not included in our models. To monitor the quasar's evolution, a series of snapshots in time are saved, known data dumps, which are output at regular or arbitrary redshift intervals, and include all the information in the simulation domain at that time. Using yt, various plots can be created for analysis, including 1D profile plots for any quantity Enzo tracks vs radius from the halo centre, 2D slice plots where a density weighted average of the quantity is calculated projected along a given axis (as shown in Figure 2.1), or even animated 3D volume rending is possible. The data in the 1D profiles for the temperature, density, metallicity may then be exported to the Cloudy code in order to calculate synthetic spectra.

2.1.6 SMS envelope simulation

This subsection describes the Enzo simulation which was post-processed to calculate observable signatures for a cool red and hot blue supermassive star in chapters 3 and 4, respectively.

In order to simulate the $\sim 10^8$ $M_{\odot}$ halo that hosts a supermassive pri-

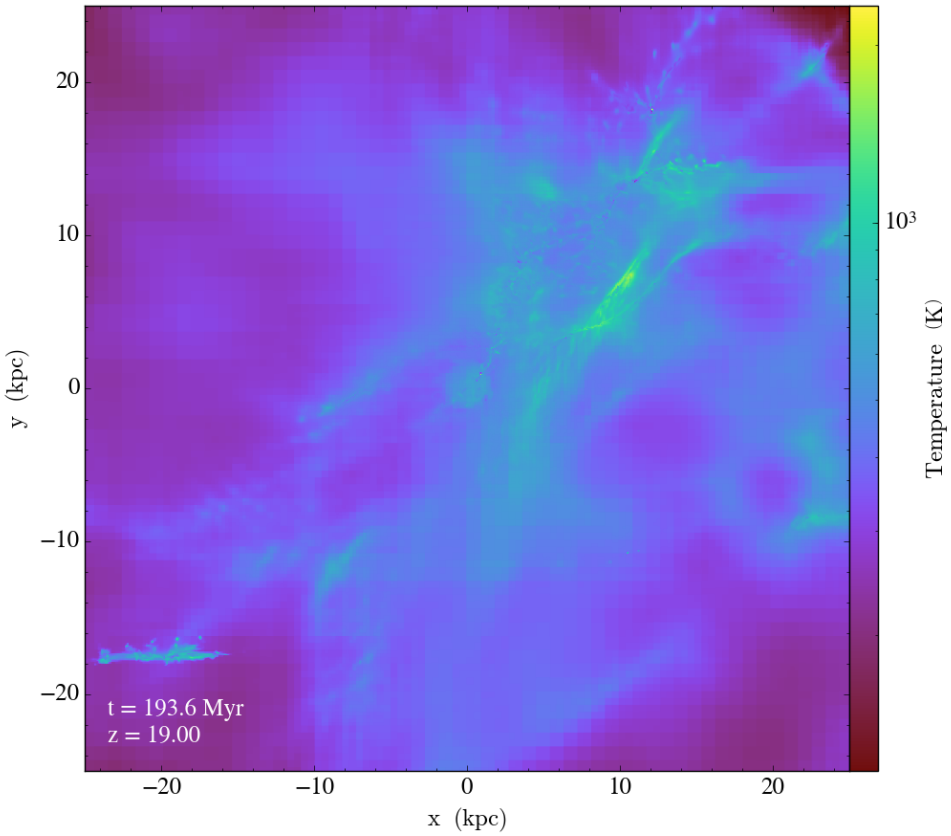

Figure 2.1: 2D temperature slice projected along the z axis, weighted by density, for a quasar at $z = 19$. The quasar is almost visible as a dot at the centre of the slice, surrounded by gas flows of varying temperature.

mordial star, it is sufficient if the simulation box only encloses the host halo without the cold gas flows that feed it. In this case, rather than the effect of the large scale cosmological environment on the host halo, we are interested in the formation, evolution, and dynamics of the atomically cooled disk that forms at the centre of the halo, which has a typical diameter of only a few parsecs, and its influence on the host halo, hence a box size of 1.5 h^{-1} Mpc (comoving) on a side was sufficient.

The halo was evolved in Enzo from an initial redshift of $z = 200$ and the simulation was halted at $z = 17.8$, when the halo reaches a mass of 2.7×10^7 $M_\odot$ and begins to atomically cool and collapse. No star particle was inserted at the centre of the halo where it would reside in nature, however this will hopefully be performed in future simulations. Given the smaller simulation box size, we were able to increase the AMR maximum refinement level compared to the quasar simulation. The host halo was therefore centered in three nested grids for an initial effective resolution of 2048^3, and we allow up to 15 levels of refinement for a maximum spatial resolution of 0.014 pc in order to model the accretion disk of diameter 1 pc.

Accretion onto the centre of the disk, where the supermassive star would reside in nature but is absent in our simulation, was calculated directly rather than through a subgrid model, since there was no star particle for which a subgrid accretion model could be used for. The accretion rate was calculated simply by constructing a sphere with a radius of 0.136 pc which encloses the region where the star would be, and dividing the difference in mass within the sphere between snapshots by the time interval.

To approximate the presence of a strong LW background, we evolve the halo without H_2, just H, H^+, e^-, He, He^+ and He^{++} (Smith et al., 2017a). Cooling by collisional ionization and excitation of H and He, bremsstrahlung, and inverse Compton scattering are all included in the energy equation.

2.2 Other simulation campaigns

Di Matteo et al. (2012) conducted their 'Massive Black' (MB) simulations, based on a modified version of GADGET2 Springel (2005), a smoothed particle hydrodynamics (SPH)-based code. They used a 533 Mpc h^{-1} on a side (in comoving units) box, and their run included gravity, hydrodynamics, and subgrid models for star formation, black holes, and various feedback processes. They found 10 BHs in the volume that grew to 10^9 $M_\odot$ by $z \sim 6$, which formed at the intersection of cold accretion streams. They tracked the gas that is eventually accreted by the BH at $z = 6$ for some of the most massive BHs, during which time Eddington accretion is attained and sustained. They found that a bubble of hot gas created by BH feedback and mostly contained within the host halo is abruptly expelled as a wind for $z \lesssim 6$, leading to self-regulated BH growth, however the cold streams feeding the BH growth are only somewhat disrupted at $z \lesssim 6$, allowing the BH to reach billions of solar masses before then.

Feng et al. (2014b) re-simulated three haloes which host $\sim 10^9$ $M_\odot$ BHs from the MB $\sim$ Gpc volume simulation above. This was done since although the mass resolution of MB is sufficient to resolve the haloes of the first quasars, the spatial resolution was insufficient to follow gas inflows below sub-kpc scales, and also experimenting with different hydrodynamics and feedback numerical schemes is too costly with very large simulations. They also found the growth history of their central SMBHs to be consistent with a sustained Eddington-limited growth provided by accretion streams that penetrate into the innermost region of the galaxies undisrupted, despite differences in resolution, SPH formulation, and AGN feedback prescription.

Costa et al. (2014b) re-simulated the six most massive haloes at $z = 6$ from the dark matter-only Millennium simulation Springel et al. (2005), which was $500h^{-1}$ comoving Mpc on a side, i.e. large enough to contain a few bright quasars. They also simulated six regions of moderate/intermediate overdenisty and and six regions of average overdensity. They found that BHs could grow to 10^9 $M_\odot$ by $z \sim 6$ only in the most overdense regions

with haloes at the intersection of massive filaments, without invoking super-Eddington accretion, whereas BHs in average regions only grew to $\sim 10^6$ $M_\odot$. The BH growth becomes feedback limited from $z \sim 8$, resulting in short bursts of accretion at the Eddington limit and strong energy-driven AGN winds, along with longer phases of more moderate accretion. They also produced rest-frame UV images of the simulated galaxies in order to test whether the required host halo masses are consistent with the observed galaxy environments of $z \sim 6$ quasars. Without strong stellar feedback, they predicted a factor of 10 or more bright galaxies than observed, however including supernova-driven galactic winds predicted a number consistent with observations, indicating that stellar feedback was already very efficient at high redshifts.

Sijacki et al. (2009) selected the most massive halo at $z = 6$ from the Millenium simulation, and re-simulated its formation at much higher resolution including gas physics and a model for BH seeding, growth and feedback. Assuming 10^5 $M_\odot$ BH seeds being seeded in $\sim 10^9 - 10^{10}$ $M_\odot$ dark matter haloes around $z \sim 15$, their simulated SMBHs are consistent with observations of $z = 6$ quasars in terms of the estimated BH masses and bolometric luminosities, the amount of star formation occurring within the host halo, and the presence of highly enriched gas in the innermost regions of the host galaxy. They also incorporated prescriptions for BH recoils caused by gravitational wave emission during BH merger events, including models with spinning BHs. They found that although BH kicks can expel a substantial fraction of low-mass BHs, they do not significantly affect the build-up of the SMBHs.

2.3 Cloudy

The densities of molecular gas found in our planet's atmosphere, or hot ionized plasma found in the interior of stars, give rise to collision timescales between particles of a few nanoseconds. There is insufficient time therefore

to radiate away any excess energy picked up during collisions, whereas in diffuse plasmas where collision timescales can range up to several million years, atoms are free to return to the ground state before the next collision. This gives rise to a dynamic balance between collisional excitations and de-excitations known as local thermodynamic equilibrium (LTE) in media with number densities above $\sim 10^{12}$ to 10^{17} cm^{-3}, depending on the gas temperature. In this case the number density of atoms or molecules in any excited state is given by the Boltzmann equilibrium, and the energy of each species will be distributed according to the Maxwell Distribution.

In many astronomical environments however the density is too low for equilibrium thermodynamics to apply, and the populations of excited states are determined by the balance between collisions from low-lying levels and radiative decay. The ionization, molecular state, level populations, kinetic temperature, and the resulting spectrum of a photoionized gas are thus the result of a host of microphysical processes. As a result the spectrum reveals much about the properties of an object such as their chemical composition or insights into their structural evolution, but it also means that modeling it is a complex task. Analytical results are only possible in limited cases, so numerical simulations must be used.

We use Cloudy, a non-local thermodynamic equilibrium (NLTE) spectral synthesis and plasma simulation code, to simulate astrophysical environments and predict their spectra and the intensities of a very large number of spectral lines. It solves the equations of radiative transfer, statistical and thermal equilibrium, ionization and recombination, and heating and cooling to calculate the excitation and ionization state of a photoionized cloud.

Cloudy treats the lightest 30 elements in detail, where elements heavier than He are classed as metals. All stages of ionization are treated, and all published charge exchange, radiative recombination, and dielectronic recombination processes are included as recombination mechanisms. Photoionization from valence and inner shells and many excited states, as well as collisional ionization by both thermal and supra-thermal electrons, and charge

transfer, are included as ionization mechanisms. Molecules are also included in the chemistry, and various grain abundance sets can be specified.

2.3.1 Setting up calculations

In order to make predictions, Cloudy fundamentally requires only three things to be specified: 1. the shape and intensity of the external radiation field striking the cloud, originating from the central illuminating source, i.e. the SMBH or SMS, 2. the chemical composition and grain content (if any) of the gas, and 3. the geometry of the gas, including its radial extent and the dependence of density on radius.

Data on the physical conditions of the gas required by Cloudy to calculate synthetic spectra is extracted from the Enzo simulations using yt, a Python analysis and visualization package for volumetric data. yt is able to read the HDF5 grid hierarchy of the output files generated by Enzo and visualize any field that it tracks with 1 or 2D plots or even 3D volume renders. For each snapshot in time saved from the simulation, yt is used to extract spherically averaged 1D profiles with bins that are uniformly partitioned in log radius space and weighted by cell mass for the hydrogen number density, gas temperature, and metallicity in units of solar metallicity. The profiles in each case are centred on the x,y,z coordinates of the MBH particle, or the centre of the accretion disk where the SMS would be located.

The outer boundary of these profiles is always the edge of the H II region or Strömgren sphere edge, where the temperature of the gas drops below 10^4 K. Below this temperature, hydrogen gas is able to recombine into its neutral form and all ionizing radiation is attenuated, therefore cutting the profiles at 4000 K ensures that we are working with a radiation-bounded cloud. To help locate the edge of the H II region, phase plots weighted by cell mass for the temperature and H II fraction vs radius can be made, examples of which are shown in Figure 2.2. These show, at each radius, the entire distribution of values for the gas temperature or ionized fraction, rather than a single averaged value displayed in 1D profile plots, which provides a fuller picture

of the gas properties. Deciding where to cut the profiles at the H II region edge may be better informed therefore, for example cutting it where the gas temperature first drops to 10^4 K might be premature if a significant fraction of the gas remains at higher temperatures and hence ionized out to larger radii.

When using Cloudy to predict quasar spectra, the photoionized cloud is split up into a series of concentric Cloudy models. Each Cloudy model corresponds to a spherical shell, with the first starting at the innermost radius of the cloud and the last going out to its exterior surface. Within each model, the physical conditions are assumed to not vary by very much. The spectrum emerging from the outer surface of a shell is calculated, which then becomes the incident spectrum to the next shell going outwards in radius, and so on. The spectrum emerging from the outermost shell of the H II region is taken to be the emitted rest frame spectrum of the quasar. This Cloudy setup is called a 'multi-model' run. When predicting supermassive star spectra, numerical errors turn out to be smaller when a single Cloudy model is used to traverse the entire H II region, and hence this setup is known as a 'single-model' run. In this case, Cloudy is able to accept physical conditions varying with radius within a single model by supplying it with the 1D profile data in the appropriate units. A schematic illustration of the two Cloudy setups is shown in Figure 2.3.

The shape of the incident radiation field to a Cloudy model must be specified between 0.0414 eV up to 100 MeV. Cloudy has a number of built-in radiation field shapes, including fundamental forms such as a blackbody, power law, or several typical AGN SEDs. The SED can also be interpolated from a table of points, or as the radiation field transmitted through a cloud and predicted by previous calculations. Note that when the incident SED is supplied as a table of points, it is interpolated to Cloudy's maximum resolution, which might be lower than that of the input data and hence some lines present there might not appear. This however does not have a significant effect on the calculation, since only very narrow lines would be

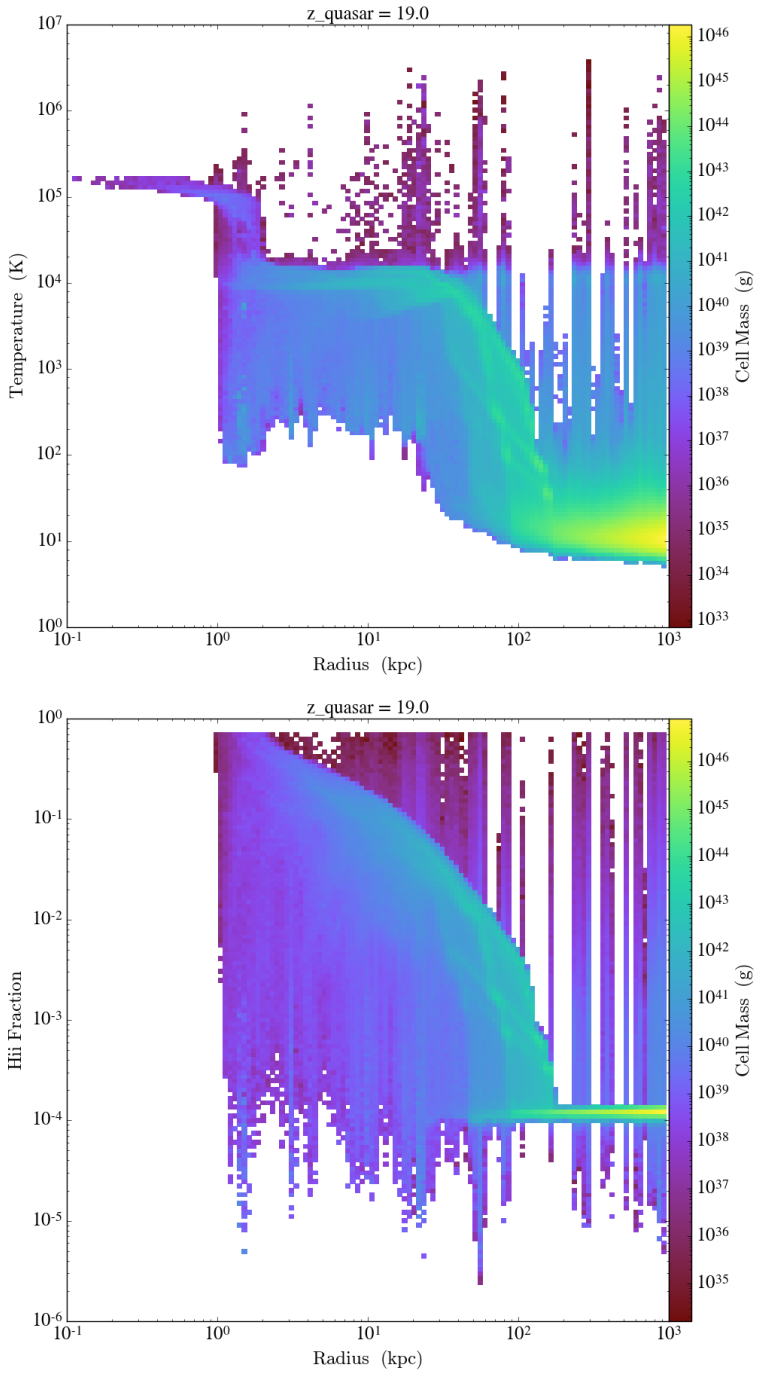

Figure 2.2: Phase plots of the gas temperature (upper panel) and ionized fraction (lower panel) for a quasar at $z = 19$

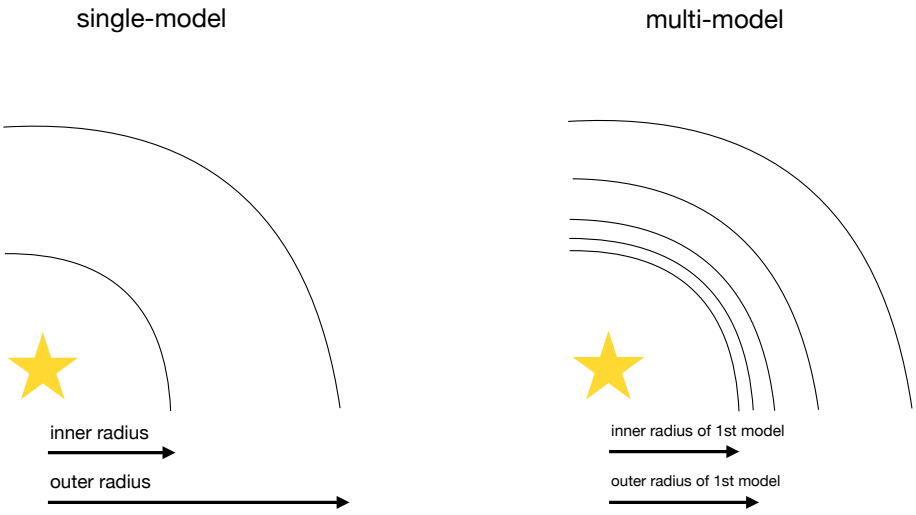

Figure 2.3: An illustration of the two approaches to modelling a cloud in the Cloudy code. In both cases each pair of arcs corresponds to a single spherical shell or Cloudy model. Left panel: using a single model to represent the entire cloud, in which the density is allowed to vary. Right panel: using multiple Cloudy models to represent the cloud, where the density is fixed for each individual model, but can vary between models.

missed. Cloudy sets the incident radiation field to zero over wavelengths where it is undefined by the user. The total power, or power per unit area in the intensity case, of the external radiation field striking the cloud must also be specified and in our case is taken as the bolometric luminosity in erg/s radiated by the central object (SMBH or SMS) into 4π steradians. Cloudy uses this value to normalise the area under the spectrum when it is integrated.

The hydrogen gas density must be specified at the illuminated face of the cloud, and is by default assumed to be constant across a model, however density gradients can also be implemented in the 'single-model' run by providing Cloudy with the 1D density profile data. The temperature of the gas can be fixed to a constant value across the model, vary with radius by providing Cloudy with 1D temperature profile data, or can remain unspecified by the user, in which case Cloudy itself calculates the temperature of the gas appropriate to the physical conditions of the cloud, e.g. the H density, chemical composition, ionization state, etc.

When the temperature is fixed at a certain value, Cloudy assumes the gas is in collisional ionization equilibrium (CIE) (sometimes called coronal equilibrium from its application to the hot coronae of stars), which is a dynamic balance at a given temperature between collisional ionization from the ground states of the various atoms and ions present in the plasma and the process of recombination from the higher ionization stages. In this equilibrium, effectively, all ions are in their ground state. Collisional ionization equilibrium is to be distinguished from the ionization balance which is achieved under conditions of local thermodynamic equilibrium. LTE is described by the Saha equation which describes a different equilibrium from the coronal approximation because in LTE, the excited states are all populated according to Boltzmann's law.

CIE assumes that two conditions apply. Firstly that the coronal approximation holds, i.e. that the plasma is optically thin to the escape of all radiation produced within its volume, photoionization can be ignored, and

only the population in the ground term of each ionic species is populated to any appreciable degree. The second requires that equilibrium among the various collisional processes has been achieved. This might not be the case, even if the conditions of coronal approximation are valid. The CIE approximation is fully valid only in very hot plasmas. The temperature at which the approximation fails depends strongly on the relative importance of the line cooling, which is a strong function of both the abundance of metals and of the thermal history of the plasma, which dominates the cooling function below $\sim 10^7$ K.

The chemical abundance of the lightest 30 elements must be fully specified for each Cloudy model. One way of doing so is through using pre-defined abundance sets, for example solar or primordial abundances, in which the number density of each element relative to H is provided. The default solar abundances can also be scaled by the metallicity in units of solar metallicity, and metallicity gradients can be implemented in the single-model runs by providing the 1D metallicity profile data. Note that only metals have their default abundances scaled since the He abundance is not enriched by star formation, so will likely not vary very much from its Big Bang nucleosynthesis (BBN) fraction, whereas metal fractions are enriched during stellar nucleosynthesis. An arbitrary abundance value for each element can also be provided, or any particular element or number of elements may be removed from the abundance set entirely.

The geometry of Cloudy models is always 1D spherical, but can be made effectively plane parallel by making the inner radius much larger than the thickness of the cloud. The covering factor, i.e. the fraction of the radiation field emitted by the central object that actually strikes nebular gas, determines whether the geometry is open or closed. In an open geometry, which we generally employ, the covering factor of the gas is small. All radiation that escapes from the illuminated face of the cloud towards the source of continuous radiation then escapes from the system without further interaction with gas. In a closed geometry with a large covering factor, the central

object is small relative to the nebula, so all diffuse fields which escape from the illuminated face of the cloud in the direction towards the central object will go on to strike the far side of the nebula. Note that these considerations make only second-order differences in the predicted emission-line spectrum, generally at the $\sim 10\%$ level.

Cloudy makes its predictions by dividing each model into a set of thin concentric shells, referred to as zones. The zones are chosen to have thicknesses that are small enough for the physical conditions across them to be assumed constant. Adaptive logic continuously adjusts the physical thicknesses of these shells to ensure this. Typically ~ 100 to 200 zones are computed in an optically thick model of an H II region.

2.3.2 Cloudy tests

There are a number of ways of trying to ascertain whether a spectrum calculated by Cloudy is physically plausible. In the first instance, sanity checks can determine whether or not a spectrum has fundamental issues.

The bolometric luminosity obtained when integrating the spectrum returned by Cloudy at the inner radius of the innermost shell (i.e. the incident spectrum to the cloud) must equal the bolometric luminosity of the source illuminating the cloud (within numerical precision). This ensures Cloudy conserves energy before any reprocessing of the spectrum has taken place. The spectrum is reprocessed by neutral hydrogen (HI) surrounding the BH, including intergalactic HI. As radiation passes through the cloud, the energy of the spectrum can increase if there is for example an energy input due to a temperature rise in the 1D profile data, which may arise from shock heating in the cloud, or supernova explosions occurring. In multi-model runs, the incident spectrum to each model may be integrated to plot the bolometric luminosity vs radius, which provides a visual means of inspecting how energy conservation fares with radius. Any rise by more than a factor of a few from the innermost value suggests issues with the calculation that should be investigated further.

Cloudy should also reproduce the shape of the incident spectrum when it is provided as a table of points. The incident spectrum returned by Cloudy can be visually compared with a plot of the input data, which should look identical barring some emission/absorption lines which may be beyond Cloudy's spectral resolution limit. Figure 2.4 shows a spectrum generated by the TLUSTY code before inputting to Cloudy (left panel) and after Cloudy has interpolated it (right panel). Note how some lines are missing from the right panel, however the spectra are nevertheless in good agreement. In addition, if a fundamental form is chosen as the incident SED, the incident SED returned by Cloudy can be inspected to ensure it peaks at the correct wavelength, i.e. obeys Wien's law, in the case of a black body spectrum, or the gradient discontinuity occurs at the correct wavelength in the case of a broken power law.

If Cloudy is set to calculate the gas temperature itself, its predictions can be compared with those predicted by Enzo via the 1D profile data. If the Cloudy temperatures are significantly lower, this would suggest that Cloudy, which is only aware of the illuminating object as the single source of heating, is missing additional heating captured by the hydrodynamics in the Enzo code due to virialization. In order to capture all the heating that is taking place, we would then construct a new temperature profile, taking whichever temperature value is highest at each radius. Figure 2.5 shows how the Enzo and Cloudy temperatures compare for a particular model.

The reason why a Cloudy calculation stopped must be understood to ensure that the predicted spectrum is not an artifact of the cloud thickness or stopping criteria. The predicted intensity will depend on thickness if the outer edge of the cloud is within a line's creation region, which is often the case for some lines in an X-ray irradiated gas, and for any radiation field and molecular or low-ionization infrared lines. Cloudy considers two geometries for defining the edge of the ionized cloud. In a radiation-bounded cloud, which we employ, the outer edge of the emitting gas is a hydrogen ionization front, and the calculation stops when the temperature falls below

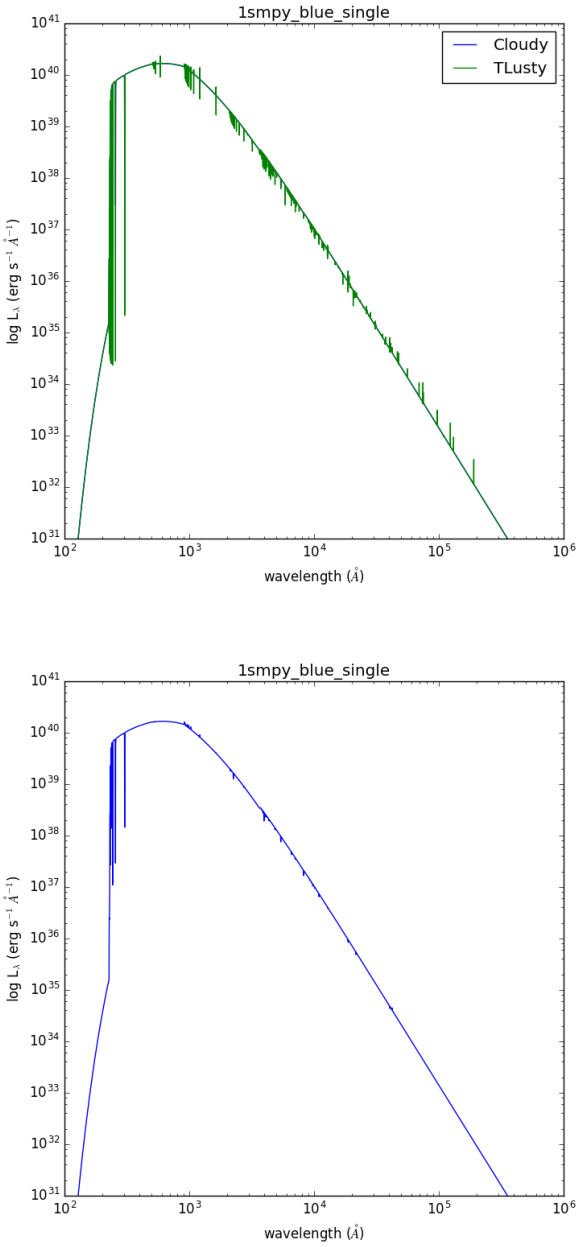

Figure 2.4: Upper Panel: A TLUSTY source frame spectrum for a hot blue metal-free supermassive star under an accretion rate of 1 $M_{\odot}$ yr^{-1}. Lower Panel: The same spectrum once it has been ported to Cloudy, with some emission and absorption lines absent.

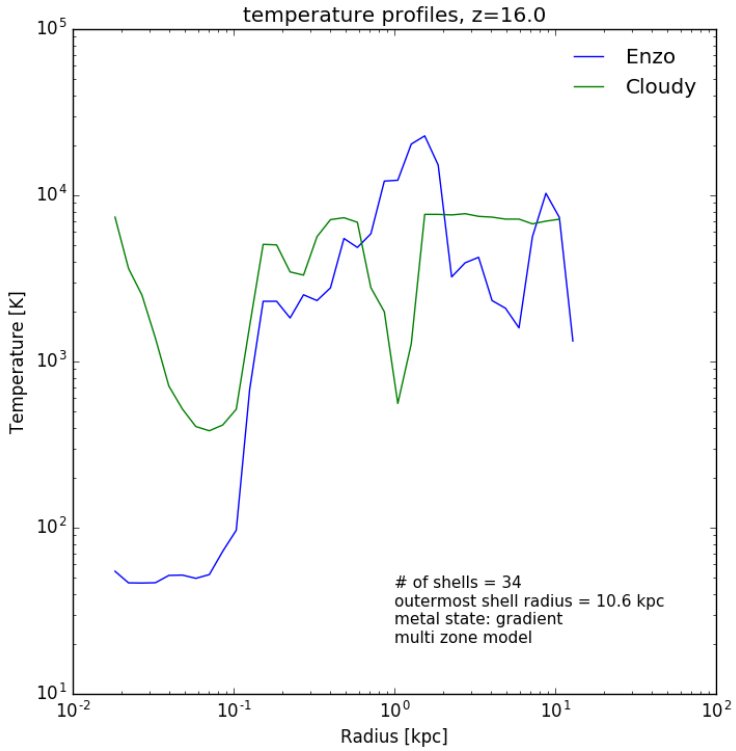

Figure 2.5: 1D profiles of a quasar H II region at $z = 16$ for the gas temperature, as calculated by Enzo (blue), and by Cloudy (green). Here Cloudy assumes that the illuminating source at the centre of the model is the only source of heating. Cloudy captures more of the heating due to the emitted radiation at shorter radii, whereas Enzo captures the hydrodynamical heating at larger radii further from the central source.

the default value of 4000 K where nearly all ionizing radiation has been attenuated. The default stopping temperature would have to be reduced to prevent the calculation stopping prematurely if we are fixing the model with a temperature below it. In a matter-bounded cloud the gas is optically thin to energetic radiation, and a column density, physical thickness, or optical depth may be specified to stop the calculation.

For multi-model Cloudy runs, the number of shells we wish to divide the cloud up into is arbitrary, although depends upon the 1D density profile data, which sets the density and width of each shell, and is limited by the resolution of the Enzo simulation. Shells can be made thinner than the profile bin width however by interpolating the profiles. It was found that on the order of 30-60 bins uniformly spaced in log radius was a good choice, to balance capturing the detail in the density profile at shorter radii with limiting numerical errors compounding in the calculation. For each Cloudy model, the bolometric luminosity of the transmitted spectrum is slightly higher than the incident one, therefore limiting the number of models is advantageous for preserving numerical accuracy. A resolution study may be preformed to find an optimal number of shells, by creating profiles with various numbers of bins and observing where the predicted spectra appear converged, i.e. stop changing their shape.

Metal enriched gas will contribute various emission lines to a spectrum, with those lines being more numerous the higher the metallicity fraction. The flux falling within a telescope filter window is therefore affected by the presence of these lines, and hence the AB magnitudes will also changed by the gas metallicity. This means that the AB magnitude at a given source redshift for a metallicity fraction between solar and primordial should lie in between the values for those metallicities. This assumes we have fixed the gas temperature, since in principle metals can affect it, and hence the contribution of nebular continuum to a filter. We can perform this check by running Cloudy with the different metal abundances and comparing the AB magnitudes at each redshift to establish a trend, as shown in Figure 2.6.

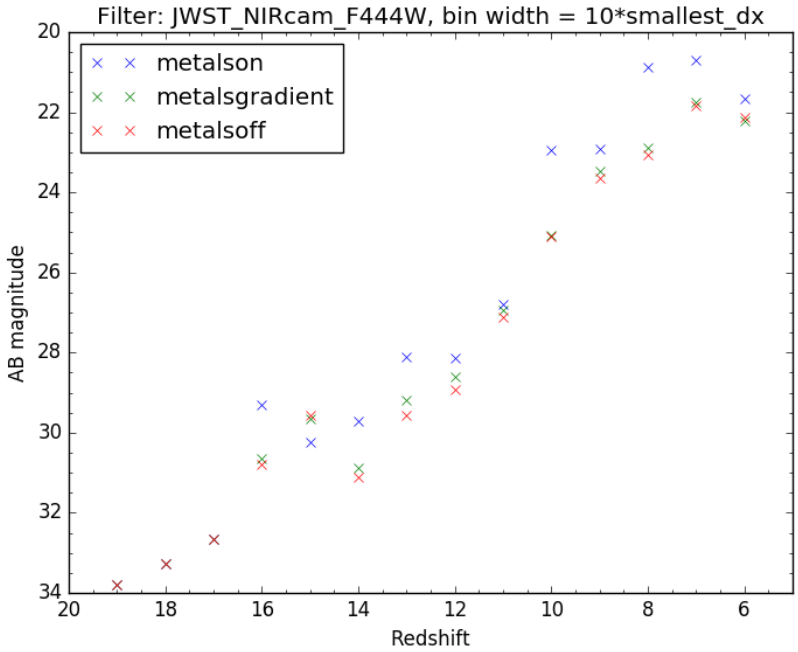

Figure 2.6: Comparing the AB magnitude in the *JWST* NIRcam F444W filter for a quasar at different source redshifts for three different sets of metal abundances in Cloudy: solar metallicity (blue crosses), Enzo 1D profile metallicities (green crosses), and a primordial metallicity (red crosses). The AB magnitudes tend to be highest for solar metallicity, and lowest for primordial metallicity gas.

Note that including a dust model in the Cloudy calculation would deplete the metal gas phase abundances to an extent, which would attenuate some metal lines, but also add new ones.

When applying the Gunn-Peterson trough to high redshift quasar spectra, we ensure that all emission bluewards of the Lyman-α line at 1216 Å is set to zero in the source frame spectrum calculated by Cloudy, including the line itself. The Lyman-α line is a prominent one which tends to lie in the near infrared when redshifted into the observer frame, and hence would contribute significantly to the AB magnitude value if not removed. The cutoff was

therefore set to 1217 Å to ensure that the line is removed in order to provide conservative brightness estimates, although note that the Lyman-α line is sometimes detected well into the reionization epoch.

Another possible reality check on the Cloudy predictions is to compare the synthetic spectra redshifted to the observer-frame and the AB magnitudes calculated for specific filters with real quasar observations at similar redshifts and wavelengths, and with a similar bolometric luminosity or inferred mass. This should provide a rough means of comparison, especially if the observed quasars possess properties close to those in our simulations. Note that quasars have currently only been observed up to redshifts ~ 7 and they tend to lie in high-metallicity and dusty environments, limiting the sample size for comparison. This should change however when the number and redshift range of sources expands with future telescopes.

To help ensure that the instrumental filter functions have been applied correctly to attenuate the observed frame spectrum, the spectrum can be plotted before and after transmission by the filter on the same axes and visually inspected. This would help identify any anomalies, which would otherwise propagate through into the AB magnitude calculation. Figure 2.7 shows a Cloudy spectrum shifted into the observed frame, before and after convolution with a filter transmission function.

In assessing the robustness of the SMS Cloudy calculation, AB magnitudes can be compared for the bare stellar spectrum, i.e. without transmission through the accretion envelope, and for transmission through both a theoretical thin envelope of uniform density and temperature with $T = 60$ K and $\rho = 10^{-26}$ g cm^{-3}, and transmission through the actual envelope as extracted from Enzo. As the radiation encounters a higher column density of gas, more flux is reprocessed to different wavelengths, and hence we might expect higher AB magnitudes for a particular filter (i.e. a dimmer object) as the envelope density increases and more flux falls at other wavelengths.

To try and debug any issues with a Cloudy spectrum for a given temperature structure, i.e. if the code is having trouble converging, we can let

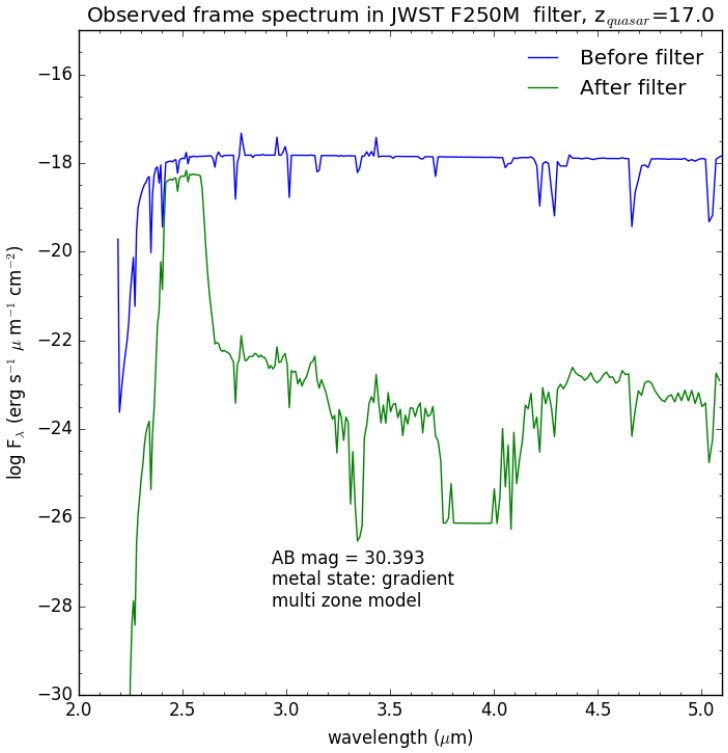

Figure 2.7: A quasar spectrum at a source redshift of $z = 17$ in the observer frame, before (blue curve) and after (green curve) transmission by the *JWST* F250M filter.

Cloudy calculate the temperature itself then compare its solution to the input values, which may shed light on what might be tripping up the calculation. Furthermore an ISM test, i.e. fixing the density to a uniform H number density of 100 cm^{-3} instead of using 1D profile data and letting Cloudy calculate the temperature should result in an emergent nebular continuum that does not drop below that of for example the input black body spectrum when modelling a supermassive star.

When creating 1D profiles from Enzo using yt, it is possible to introduce numerical artifacts into the data. This can occur if the requested number of profile bins given a certain profile radius corresponds to a spatial resolution higher than that present in the simulation. Providing a Cloudy model with a temperature or density value of zero is clearly unphysical, therefore such values must be removed from the 1D profiles before the Cloudy models are set up. Figure 2.8 shows the effect of increasing the number of bins in a 1D spherically averaged temperature profile. Note how the profile 'noise' increases with more bins since the averaging shell is thinner, therefore capturing more finely grained detail, at the expense of introducing zero-valued bins at short radii.

Whether we model the cloud using a single Cloudy model, or split the cloud up into a series of concentric shells each corresponding to a Cloudy model, is of course an arbitrary choice, however it can have an effect on the predicted spectra. Thus we can employ both approaches when starting out and compare the spectra, integrated luminosity, and calculated AB magnitudes to decide which one leads to more plausible results.

Another Cloudy sanity check which may be applied relating to chemical composition is calculating the He mass fraction, χ_{He}, from the He number density relative to H, Y_{He}, which is reported by Cloudy. Y_{He} should not vary much from its primordial value of ~ 0.24, even once metal enrichment has occurred. We start from the mass fractions:

$$\chi_{\mathrm{H}} + \chi_{\mathrm{He}} = 1, \tag{2.9}$$

where χ_{H} is the H mass fraction ≈ 0.76. This equation assumes no metals are

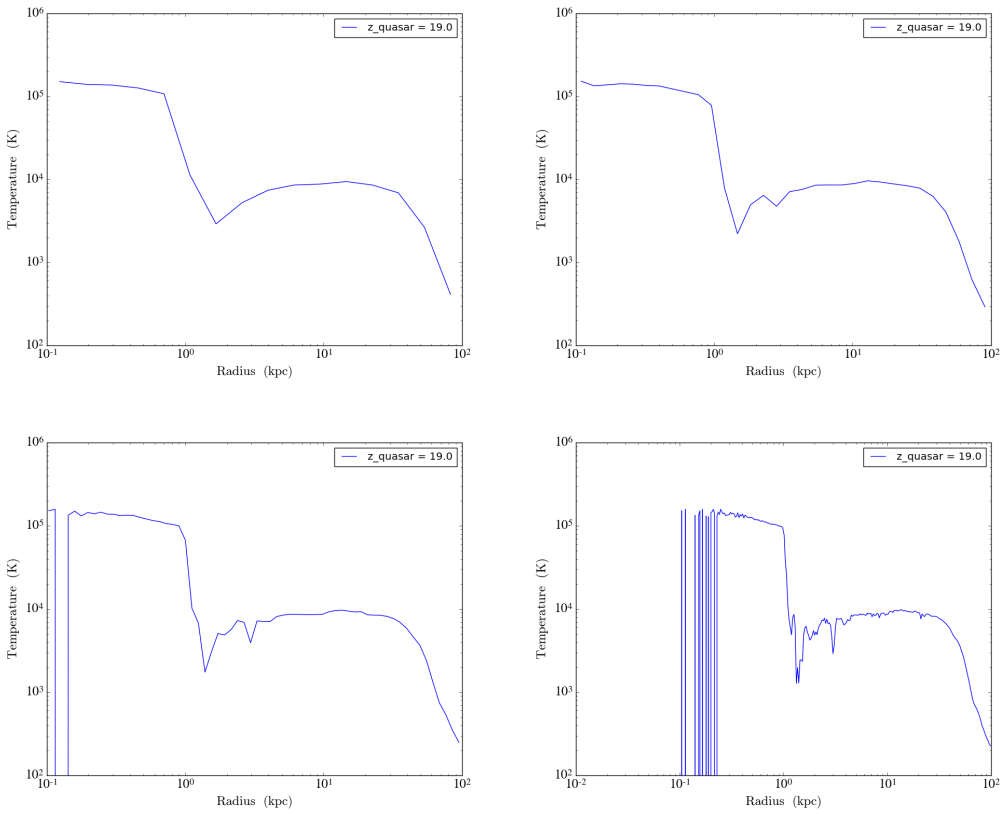

Figure 2.8: 1D spherically averaged gas temperature profiles for a quasar at $z = 19$ created with 16 bins (top left), 32 bins (top right), 64 bins (bottom left), and 256 bins (bottom right). Zero-valued bins are present for 64 and 256 bin profiles.

present which is not the case, even for primordial gas which possesses trace metal abundances as a relic of BBN, however it is a good approximation considering the metal mass fractions are relatively low even in gas around solar metallicity. To obtain $\chi_{\rm He}$ in terms of $Y_{\rm He}$, after some algebra we obtain:

$$\begin{aligned}\chi_{\rm He} = \frac{M_{\rm He}}{M_{\rm H}+M_{\rm He}} = \frac{N_{\rm He}m_{\rm He}}{N_{\rm H}m_{\rm H}+N_{\rm He}m_{\rm He}} = \frac{n_{\rm He}Vm_{\rm He}}{n_{\rm H}Vm_{\rm H}+N_{\rm He}Vm_{\rm He}} \\ = \frac{Y_{\rm He}n_{\rm H}4m_{\rm H}}{n_{\rm H}m_{\rm H}+Y_{\rm He}n_{\rm H}4m_{\rm H}} = \frac{4Y_{\rm He}}{1+4Y_{\rm He}},\end{aligned} \tag{2.10}$$

where $m_{\rm He} \approx 4m_{\rm H}$, and $Y_{\rm He} = n_{\rm He}/n_{\rm H}$. We then plug in $Y_{\rm He}$ from Cloudy and compare with its expected value of ~ 0.24.

2.4 Redshifting source spectra and calculating AB magnitudes

Cloudy computes the source frame spectrum emitted by the H II region of the quasar or SMS. To provide observable predictions, we developed a routine to calculate the AB magnitude, i.e. a measure of the total flux falling within a filter window in the observer frame. The first step is to cosmologically redshift and attenuate the source frame spectrum according to geometric dilution. The quantity $L(\lambda) = \lambda L_\lambda$ used by Cloudy in erg s^{-1} is converted to the flux density, F_λ in erg s^{-1} cm^{-2} μm^{-1} in the observer frame by

$$F(\lambda) = \frac{L\left(\frac{\lambda}{1+z}\right)}{\frac{\lambda}{1+z}(1+z)4\pi d_{\rm L}^2(z)}, \tag{2.11}$$

where λ is the wavelength in the observer frame and $d_{\rm L}(z)$ is the luminosity distance, given by

$$d_{\rm L}(z) = (1+z)c/{\rm H}_0 \int_0^z \frac{1}{\sqrt{\Omega_{\rm M}(1+z)^3+\Omega_\Lambda}} dz, \tag{2.12}$$

where $\rm H_0$ is the value of the Hubble constant today, and $\Omega_{\rm M}$ and Ω_Λ are the matter and dark energy density respectively.

Equation 2.11 is constructed to conform with the Cloudy convention for integrating the source frame spectrum that

$$\sum_{\lambda} \frac{L(\lambda)}{\lambda} \Delta\lambda = L_{\rm bol}, \tag{2.13}$$

where $\Delta\lambda$ is the width of the wavelength bins. There is an important subtlety to be aware of when converting the rest frame luminosity to observer frame flux. There is no universal way of performing this conversion, since some authors divide λL_λ by λ, while others divide by $\Delta\lambda$, i.e. the wavelength bin width. The correct convention to choose is the one which reproduces the bolometric luminosity of the source when the source frame spectrum is integrated.

AB magnitudes, $m_{\rm AB}$, in specific filters are then computed from

$$m_{\rm AB} = -2.5 \log_{10} \left(\frac{\int_0^\infty F(\lambda) T(\lambda) d\lambda}{\int_0^\infty F_0(\lambda) T(\lambda) d\lambda} \right), \tag{2.14}$$

where $T(\lambda)$ is the filter transmission function, $F_0(\lambda) = 3.630781 \times 10^{-20} c \lambda^{-2}$ ergs cm^{-2} s^{-1} m^{-1} is the reference spectrum for AB magnitudes, and c is the speed of light. Radiation blueward of $\lambda_{{\rm Ly}\alpha} = 1216$ Å emitted at $z > 6$ may be redshifted into $\lambda_{{\rm Ly}\alpha}$, resonantly scattered, and hence never observed (Gunn & Peterson, 1965). Consequently, at $z > 6$ we simply take all the flux shorter than $\lambda_{{\rm Ly}\alpha}$ to be absorbed by the IGM and remove it from the spectrum.

In order to validate our AB magnitude calculation, we reproduced the left panel of Figure 11 from Whalen et al. (2013e), i.e. NIRcam light curves for four different masses of zero metallicity Pop III star pair instability supernovae explosions at $z = 10$. Here, light curve refers to the H band AB magnitudes vs time since the explosion in the observer frame.

Chapter 3

On the Detection of Supermassive Primordial Stars

3.1 Abstract

The collapse of supermassive primordial stars in hot, atomically-cooled haloes may have given birth to the first quasars at $z \sim 15$ - 20. Recent numerical simulations of these rapidly accreting stars reveal that they are cool, red hypergiants shrouded by dense envelopes of pristine atomically-cooled gas at 6,000 - 8,000 K, with luminosities $L \gtrsim 10^{10}\ L_{\odot}$. Could such luminous but cool objects be detected as the first stage of quasar formation in future near infrared (NIR) surveys? We have now calculated the spectra of supermassive primordial stars in their birth envelopes with the Cloudy code. We find that some of these stars will be visible to *JWST* at $z \lesssim 20$ and that with modest gravitational lensing *Euclid* and the *Wide-Field Infrared Space Telescope* (*WFIRST*) could detect them out to $z \sim 10$ - 12. Rather than obscuring the star, its accretion envelope enhances its visibility in the NIR today by reprocessing its short-wavelength flux into photons that are just redward of the Lyman limit in the rest frame of the star.

3.2 Introduction

Supermassive primordial stars (SMSs) may have been the origin of the first quasars, a few of which have now been discovered at $z > 7$ (Mortlock et al., 2011; Bañados et al., 2018). These stars are thought to form in primordial haloes exposed to either unusually strong Lyman-Werner (LW) UV fluxes (Agarwal et al., 2016b) or highly supersonic baryon streaming motions (Hirano et al., 2017; Schauer et al., 2017). Either one can prevent primordial haloes from forming stars until they reach masses of 10^7 - 10^8 $M_\odot$ and virial temperatures of $\sim 10^4$ K that trigger rapid atomic cooling and catastrophic baryon collapse at central infall rates of up to ~ 1 $M_\odot$ yr^{-1} (Bromm & Loeb, 2003; Lodato & Natarajan, 2006; Wise et al., 2008; Regan & Haehnelt, 2009b; Latif et al., 2013).

Stellar evolution models show that Population III (Pop III) stars growing at these rates can reach masses of a few 10^5 $M_\odot$. Most then collapse to black holes (direct collapse black holes, or DCBHs; Umeda et al., 2016; Woods et al., 2017; Haemmerlé et al., 2018b) via the general relativistic (GR) instability, although a few non-accreting stars have been found to explode as highly energetic thermonuclear transients (Whalen et al., 2013b; Johnson et al., 2013b; Whalen et al., 2013d, 2014; Chen et al., 2014). Pop III SMSs are currently the leading contenders for the seeds of the earliest supermassive black holes (SMBHs) because the environments of ordinary Pop III star BHs are less conducive to their rapid growth (Whalen et al., 2004; Alvarez et al., 2009; Whalen & Fryer, 2012; Smith et al., 2018). DCBHs are born with large masses in high densities in host galaxies that can retain their fuel supply, even when it is heated by X-rays (Johnson et al., 2013a).

What are the prospects for detecting SMSs at high redshifts? Hartwig et al. (2018) found that the relics of such stars would be uniquely identifiable with the gravitational wave detector LISA at $z > 15$ if they form in binaries. Johnson et al. (2012) examined some spectral features of hot, blue, rapidly-accreting SMSs and found that they would be characterized by strong Balmer emission, i.e. hydrogen emission lines due to electron transitions from

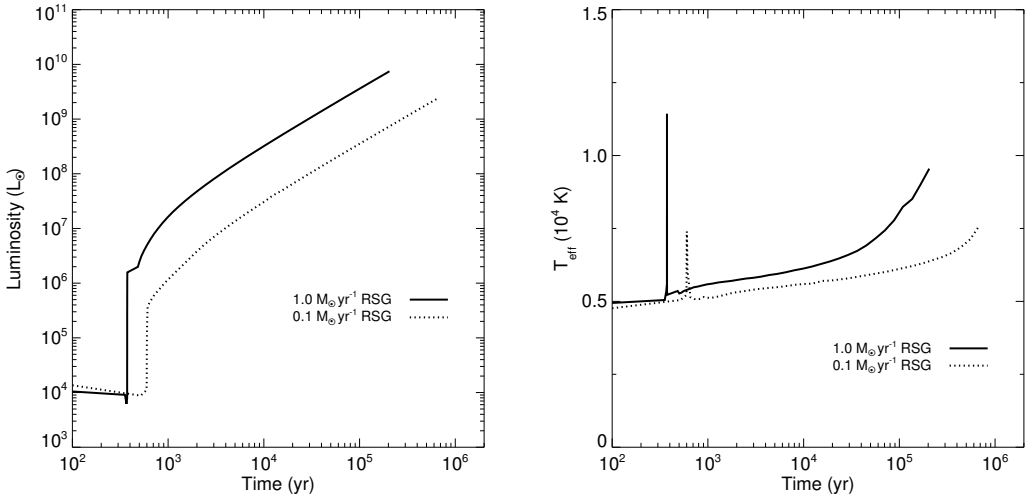

Figure 3.1: Evolution of red supergiant (RSG) stars with an initial mass of 10 $M_\odot$ accreting at 1.0 and 0.1 $M_\odot$ yr^{-1} in the GENEVA stellar evolution code. Left panel: luminosities. Right panel: surface temperatures.

excited states to the $n = 2$ level, and the conspicuous absence of Lyα lines due to absorption by their envelopes. The source of this flux was not the star but its hypercompact H II region, whose ionizing radiation was trapped close to its surface by the density and ram pressure of the inflow (which was also found to be true in cosmological simulations of highly resolved atomically cooled haloes; Becerra et al., 2018). Freese et al. (2010), Zackrisson et al. (2010a) and Zackrisson et al. (2010b) calculated the spectral signatures of hot, blue Pop III 'dark stars', supermassive primordial stars powered by the self-annihilation of weakly-interacting dark matter rather than by nuclear fusion. They found that such objects might be visible even to $8 - 10$ m telescopes on the ground today, primarily because of their high surface temperatures (20,000 - 30,000 K), larger masses (up to 10^7 $M_\odot$) and longer lives (up to 10^7 yr).

But several studies have now shown that rapidly accreting Pop III stars generally evolve as cool, red hypergiants along the Hayashi limit with surface

temperatures of 5,000 - 10,000 K (Hosokawa et al., 2013). The Hayashi limit is a constraint upon the maximum radius of a star for a given mass. When a star is fully within hydrostatic equilibrium, i.e. where the inward force of gravity is matched by the outward pressure of the gas, then the star can not exceed the radius defined by the Hayashi limit. Haemmerlé et al. (2018a) found that such stars can reach luminosities $\gtrsim 10^{10}\ L_{\odot}$ that could in principle be visible to *JWST* (Kalirai, 2018), *Euclid*, *WFIRST* and extemely large telescopes (ELTs) on the ground. However, they are shrouded by dense accretion flows that reprocess radiation from the star, perhaps suppressing its flux in the NIR today. Detecting SMSs at high redshift would capture primordial quasars at the earliest stages of their development and reveal one of their channels of formation. Here, we calculate NIR luminosities for Pop III SMSs in their accretion envelopes whose structures are taken from a high-resolution cosmological simulation. We describe our models in Section 3.3, calculate SMS spectra and NIR magnitudes in Section 3.4 and conclude in Section 3.5.

3.3 Numerical Method

Rest frame spectra for the star in its envelope are calculated with Cloudy (Ferland et al., 2017) with envelope profiles taken from a simulation of the collapse of an atomically-cooled halo done with Enzo (Bryan et al., 2014). The spectra are then redshifted, dimmed, and convolved with a variety of filter functions to obtain AB magnitudes in the NIR as a function of SMS redshift. We consider stars accreting at 0.1 and 1.0 $M_{\odot}\ \mathrm{yr}^{-1}$ whose properties are listed in Tables A3 and A2 of Haemmerlé et al. (2018a), respectively. Bolometric luminosities, L_{bol}, and effective temperatures, T_{eff}, for both stars calculated using the GENEVA stellar evolution code are shown in Figure 3.1.

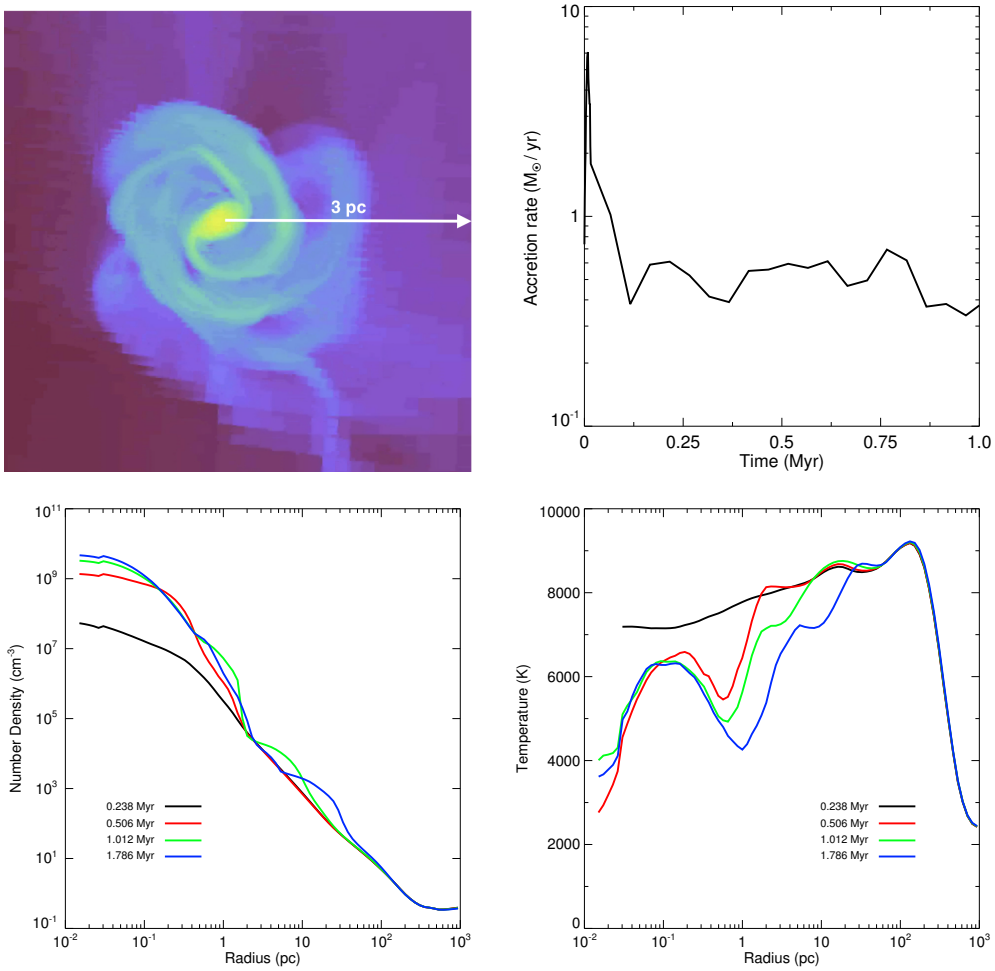

Figure 3.2: Top left: 2D density slice (6 pc proper on a side) of the accretion disk at 0.625 Myr after the onset of collapse. Top right: central accretion rates. Bottom left: spherically-averaged gas densities in the halo. Bottom right: spherically-averaged temperatures.

3.3.1 Enzo Envelope Model

The halo in which the SMS is assumed to form was evolved in a 1.5 h^{-1} Mpc box in Enzo from $z = 200$ down to $z = 17.8$, when it reaches a mass of 2.7 $\times 10^7$ $M_\odot$ and begins to atomically cool and collapse. It is centered in three nested grids for an initial effective resolution of 2048^3, and we allow up to 15 levels of refinement for a maximum resolution of 0.014 pc. The grid is initialized at $z = 200$ with cosmological parameters taken from the second-year *Planck* release: $\Omega_{\rm M} = 0.308$, $\Omega_\Lambda = 0.691$, $\Omega_{\rm b} = 0.0223$, $h = 0.677$, $\sigma_8 = 0.816$, and $n = 0.968$ (Planck Collaboration et al., 2016). No star particle was inserted at the halo centre, where it would reside in nature. The effect of the star on its host halo was modelled by post-processing the Enzo simulation with Cloudy, making use of the stellar evolution code GENEVA to generate the incident stellar black body spectrum. To approximate the presence of a strong LW background, we evolve the halo without H_2, just H, H^+, e^-, He, He^+ and He^{++} (Smith et al., 2017a). Cooling by collisional ionization and excitation of H and He, bremsstrahlung, and inverse Compton scattering are all included in the energy equation.

As shown in the upper left panel of Figure 3.2, a large atomically cooled disk forms at the center of the halo that is $\sim$ 2 pc in diameter and at 4,000 - 6,000 K at 0.625 Myr after the onset of collapse. A bar instability in the disk efficiently transports angular momentum out of its center, producing the large sustained accretion rates onto the center shown in the upper right panel of Figure 3.2. After a brief burst due to initial collapse and the formation of the disk, infall proceeds at rates of 0.4 - 0.6 $M_\odot$ yr^{-1}. Spherically averaged density and temperature profiles of the halo are shown in the bottom two panels of Figure 3.2 at 0.238 Myr, 0.506 Myr, 1.012 Myr and 1.786 Myr after the onset of collapse.

3.3.2 Cloudy Spectra

We treat both stars as blackbodies (BBs) because they are relatively cool and have no absorption lines due to metals. Cloudy fits BB spectra to each star from $L_{\rm bol}$ and $T_{\rm eff}$, which we take to be 1.26×10^9 $L_\odot$ and 6653 K for the 0.1 $M_\odot$ yr^{-1} star and 3.92×10^9 $L_\odot$ and 8241 K for the 1.0 $M_\odot$ yr^{-1} star. These values correspond to 3.49×10^5 yr and 1.089×10^5 yr for the two stars, about halfway through their respective lifetimes. Ideally, one would surround the star with the accretion envelope that created it in a cosmological simulation for self-consistency. But stellar evolution models of Pop III SMSs in time-dependent cosmological flows are not yet available, so we instead use density and temperature profiles from the Enzo simulation at 1.786 Myr as the envelope of each star. This choice is reasonable because the accretion rates associated with these profiles are intermediate to those in which our stars were evolved. The accretion rates onto the centre of the atomically cooled disk in Enzo were calculated using yt by tallying the mass passing through a spherical region.

The density and temperature profiles of the envelope that are input to Cloudy are tabulated in 70 bins that are uniformly partitioned in log radius, with inner and outer boundaries at 0.015 pc and 927 pc. Cloudy solves the equations of radiative transfer, statistical and thermal equilibrium, ionization and recombination, and heating and cooling to calculate the excitation and ionization state of the gas surrounding the star and compute its emergent spectrum. The temperatures of the gas falling onto the star are set by the virialization of cosmic flows well above it, not by radiation from the star. Since they determine to what degree the envelope is collisionally excited, and thus how it reprocesses photons from the star, we required Cloudy to use the temperatures Enzo calculates for the envelope instead of inferring them from the spectrum of the SMS because they would have been too low otherwise.

3.4 Observing Supermassive Stars

3.4.1 SMS Spectra

We show spectra for the 1.0 $M_\odot$ yr^{-1} star at 1.089×10^5 yr before and after attenuation by its envelope in Figure 3.3. As expected, the stellar spectrum peaks at 0.352 μm according to Wien's displacement law, i.e. $\lambda_{\rm max} = b/T$ where $b \approx 2898$ μm·K and T is the temperature in Kelvins. Absorption by the envelope at the Lyman limit of H is clearly visible at 0.0912 μm. The Lyman limit is the short-wavelength end of the hydrogen Lyman series, i.e. the series of UV lines due to electron transitions from excited states to the ground state $n = 1$, and corresponds to the energy required for an electron to fully escape the potential barrier from the ground state. The continuum absorption below 0.0912 μm is punctuated by several prominent He emission lines. There is a Lyα emission line at 0.1216 μm, a strong Hα line visible at 0.656 μm, and strong Paschen series lines visible at 1.28 μm and 1.88 μm. Hα is a hydrogen Balmer series line in the visible band due to an electron transition from $n = 3$ to $n = 2$. Paschen series lines in hydrogen are the result of electron transitions from excited states down to the $n = 3$ level. There is continuum absorption half a decade in wavelength above and below 1.65 μm due to H^- bound-bound and bound-free opacity, respectively.

Photons from the star that are blueward of the Lyman limit are reprocessed by its envelope into the Lyα and two-photon continuum emission visible at 0.1216 - 0.16 μm. Two-photon emission occurs when an electron transitions from the 2s to the 1s state via emission of two photons. Quantum mechanical selection rules due to not allow the transition to occur with one photon, and at the densities encountered here the electron is unlikely to be excited from the 2s to the 2p state, from where it could decay to 1s with a single photon. This latter flux is greater than that emitted by the star itself and can enhance its visibility in the NIR today. The effect varies with $T_{\rm eff}$ and source redshift but is at most 0.5 - 1 AB mag. The Lyα will not aid in the detection of the star because it will be scattered into a halo of low surface

brightness in the neutral IGM. We note that at the velocities and densities of the infall onto the surface of the star, the luminosity of its accretion shock is at most $\sim 10^4\ L_\odot$ and does not produce a significant contribution to the visibility of the SMS.

3.4.2 NIR Magnitudes

We show AB magnitudes for both stars in *JWST* NIRCam bands at 2.5 - 4.6 μm in the top left panel of Figure 3.4. The 1.0 $M_\odot$ yr^{-1} SMS is consistently 1 - 2 magnitudes brighter than the 0.1 $M_\odot$ yr^{-1} SMS except at high redshifts at 2.50 μm, where both luminosities abruptly fall off because of absorption of flux blueward of Lyα in the source frame of the star by the neutral intergalactic medium (IGM) at $z \gtrsim 6$. At $z \sim 6 - 8$ the two stars are brightest in the 3.56 μm filter but at $z > 10$ they are brighter in the 4.44 μm and 4.60 μm bands, with magnitudes that vary from 28.5 - 31.5 at $z =$ 6 - 20 for the 1.0 $M_\odot$ yr^{-1} SMS and 29.5 - 33.5 for the 0.1 $M_\odot$ yr^{-1} SMS.

SMS magnitudes are much more uniform in redshift in the mid infrared, as we show for several *JWST* MIRI bands in the top right panel of Figure 3.4. They exhibit the greatest variation at 5.6 μm, which is closest to the NIR, but largely level off at 7.7 - 25.5 μm. This behavior is primarily due to the flattening of the spectrum at wavelengths above 1.5 μm in the source frame due to reprocessing of flux from the star by its envelope. The two stars are brightest from $z =$ 6 - 20 at 5.6 - 10.0 μm, with magnitudes $\lesssim 31$ and could therefore provide important additional spectral confirmation of SMS candidates in NIRCam.

We show SMS magnitudes for *Euclid* and *WFIRST* in the lower two panels of Figure 3.4. Absorption by the neutral IGM at $z \gtrsim 6$ quenches Y, J and H band fluxes at $z \gtrsim 7$, 10 and 14, respectively, limiting detections of these stars to these redshifts in these filters. Magnitudes for the 1.0 $M_\odot$ yr^{-1} star vary from 29.5 - 31.8 in *Euclid* and 29 - 32.5 in *WFIRST* at $z = 6$. For the 0.1 $M_\odot$ yr^{-1} star, they vary from 31.5 - 32.5 in *Euclid* and from 31 - 32.5 in *WFIRST* at the same redshift. They drop off more rapidly with redshift

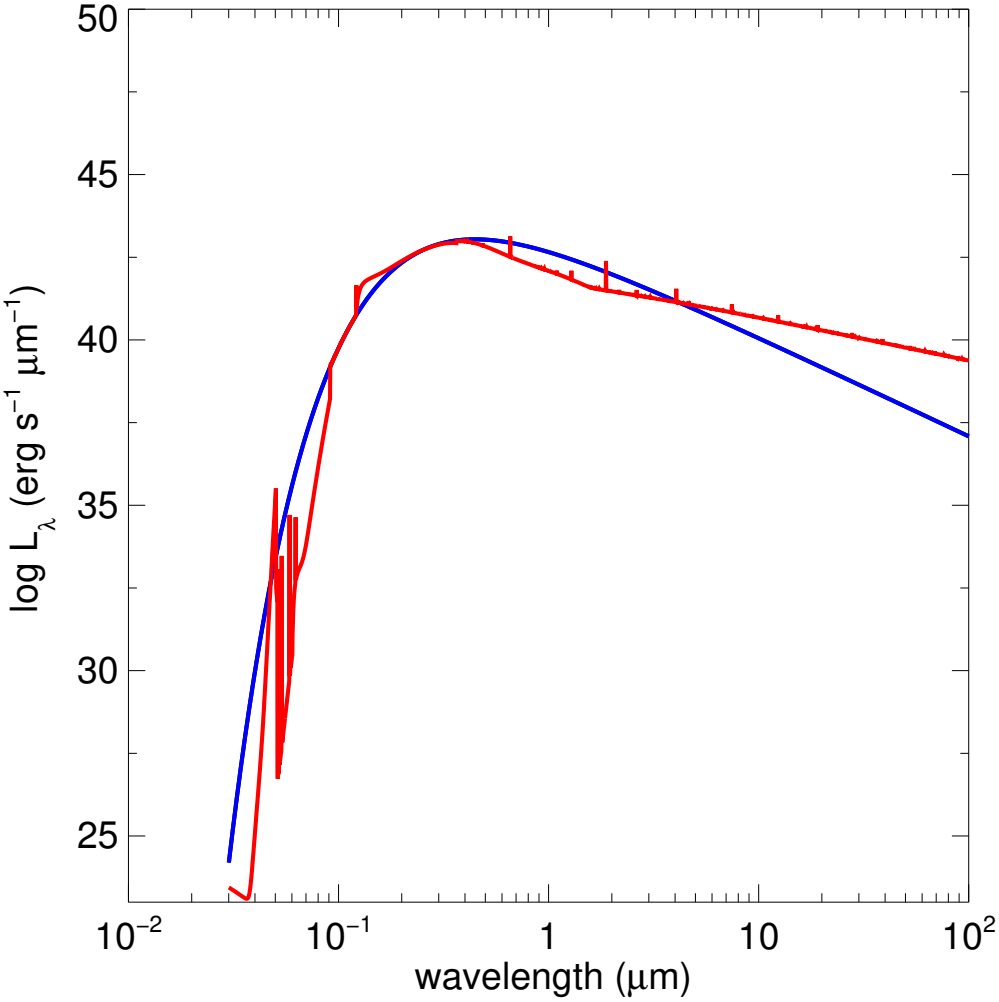

Figure 3.3: 1.0 $M_\odot$ yr^{-1} SMS spectra at a stellar age of 100,000 yr. Blue: spectrum of the star itself; red: spectrum after reprocessing by the envelope.

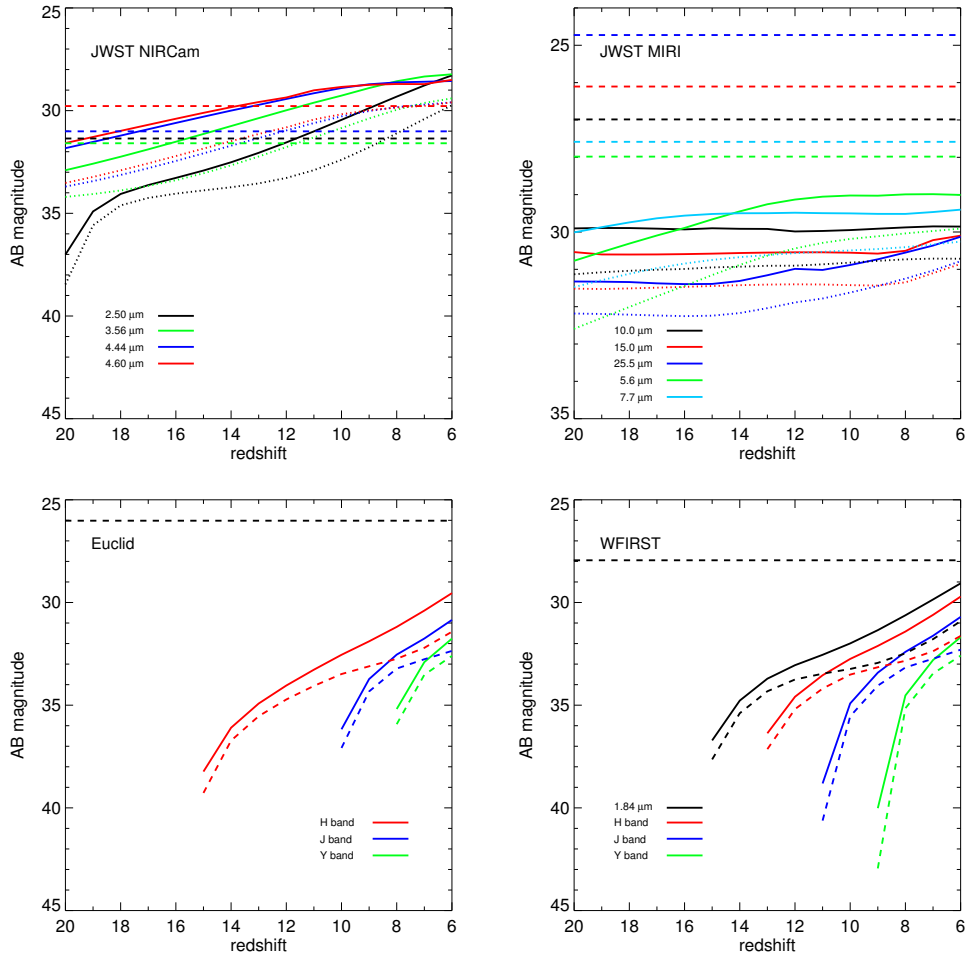

Figure 3.4: NIR AB magnitudes for the 1.0 $M_\odot$ yr^{-1} (solid) and 0.1 $M_\odot$ yr^{-1} (dashed) SMSs in *JWST*, *Euclid* and *WFIRST* bands. Top left: *JWST* NIRCam bands. Top right: *JWST* MIRI bands. Bottom left: *Euclid*. Bottom right: *WFIRST*. The horizontal lines are the 5σ AB magnitude detection limits for 100 hour exposures in the filter of the corresponding colour for the *JWST* filters, and the detection limits for deep-drilling fields in *Euclid* and *WFIRST*.

than in the NIRCam bands because spectral luminosities in the source frame fall with decreasing wavelength below ~ 0.3 μm.

3.4.3 SMS Formation / Detection Rates

Since the lifetime of an SMS is much smaller than the Hubble time, even at the high redshifts at which it is likely to form, the number of SMSs per unit redshift per unit solid angle at a redshift z can be written as

$$\frac{\mathrm{d}N}{\mathrm{d}z\mathrm{d}\Omega} = \dot{n}_{\mathrm{SMS}}\, t_{\mathrm{SMS}}\, r^2 \frac{\mathrm{d}r}{\mathrm{d}z}, \tag{3.1}$$

where $\dot{n}_{\mathrm{SMS}}$ is the SMS formation rate per unit comoving volume, t_{SMS} is the characteristic lifetime of an SMS, and $r(z)$ is the comoving distance to redshift z,

$$r(z) = \frac{c}{H_0} \int_0^z \frac{\mathrm{d}z'}{\sqrt{\Omega_{\mathrm{m}}(1+z')^3 + \Omega_\Lambda}}. \tag{3.2}$$

Unfortunately, $\dot{n}_{\mathrm{SMS}}$ is poorly constrained, with theoretical models predicting number densities that vary by up to eight orders of magnitude (see, e.g., the recent review of Woods et al., 2018). These models also predict different evolutions in $\dot{n}_{\mathrm{SMS}}$ with redshift. Habouzit et al. (2016) predict a steady increase in the comoving number density of SMSs with decreasing z while Valiante et al. (2017) predict that most form in the narrow range $z \sim 16$–18. We therefore consider two toy models that bracket this range of $\dot{n}_{\mathrm{SMS}}$.

In the first, our "optimistic" model, we assume that most SMSs form at $z \sim 10$–12 and that the final comoving number density is around $10^{-1}\,\mathrm{Mpc}^{-3}$, as in the Habouzit et al. (2016) model with a low value for J_{crit}. In the other, our "pessimistic" model, we assume that most SMSs form at redshifts $z \sim 16$–18, as in Valiante et al. (2017), with a final comoving number density of around $10^{-8}\,\mathrm{Mpc}^{-3}$. The optimistic model yields approximately 4×10^7 potentially observable SMSs per steradian per unit redshift, or around 30 per NIRCam field of view. On the other hand, the pessimistic model predicts only ~ 10 SMSs per steradian per unit redshift, meaning that any given NIRCam pointing with the appropriate limiting magnitude would have a probability of only around 10^{-5} of detecting an SMS.

The chances of detecting an SMS are highly dependent on the model assumed for their formation. However, since some models predict number counts high enough for one or more SMSs to be found in any sufficiently deep NIRCam image, *JWST* will begin to place observational constraints on these models, even if it cannot rule out extreme ones such as our pessimistic model. We note that no SMSs have been found in the *Hubble* Ultra Deep Field to date because of its AB mag limit of 29 at 1.38 μm in the H band, which is well below that expected of either star even at $z \sim 6$.

3.5 Conclusion

At NIRCam AB magnitude limits of 31.5 *JWST* could detect the 1.0 $M_{\odot}$ yr^{-1} SMS at $z \lesssim 20$ and the 0.1 $M_{\odot}$ yr^{-1} SMS at $z \lesssim 13$. But the prospects for discovering such stars would be better if they could also be found by *Euclid* and *WFIRST* because their wide fields would enclose far more of them at high redshifts. Once flagged, SMS candidates could then be studied with *JWST* in greater detail. However, as shown in Figure 3.4, the H band magnitudes of both stars at $z = 6$ - 20 are are fainter than current *Euclid* and *WFIRST* detection limits (26 and 28, respectively).

But this does not mean *Euclid* and *WFIRST* will not find these stars because only modest gravitational lensing is required to boost their fluxes above their detection limits. The fields of view of both missions will enclose thousands of galaxy clusters and massive galaxies, and at $z \sim 6$ - 10 magnification factors of only 10 - 100 would be required to reveal either star. It is likely that a sufficient fraction of their survey areas will be lensed to such factors (Rydberg et al., 2018). Even higher magnifications may be possible in future surveys of individual cluster lenses by *JWST* but at the cost of smaller lensing volumes (Whalen et al., 2013a; Windhorst et al., 2018).

In our Enzo and Cloudy calculations we have neglected the effect of radiation pressure due to flux from the star on the flows that create it. Modeling these effects in cosmological simulations is challenging in part because they

must resolve photospheres on very small scales that preclude the codes from evolving them for long times. Smith et al. (2017b) post processed simulations of highly resolved atomically cooling haloes with Lyα photon transport and found it could exert mechanical feedback on flows in the vicinity of the star. Radiation hydrodynamical simulations by Luo et al. (2018) and Ardaneh et al. (2018) that neglect resonant Lyα scattering found that radiation from the protostar in its early stages did not significantly alter flows in its vicinity but did suppress fragmentation, thus promoting the rapid growth of a single supermassive object. In principle, radiation from the SMS could blow out gas and partially expose it to the IGM, but this will have little effect on the AB magnitudes of the star today because all that would be lost is the mild enhancement of UV flux redward of the Lyman limit by the envelope discussed in Section 3.1.

While we have only considered cool red supergiant stars, hotter SMSs could be easier to detect because they would produce more flux in the NIR today. Low accretion rates ($\lesssim 0.005\ M_\odot\ \mathrm{yr}^{-1}$; Haemmerlé et al., 2018a) or clumpy accretion due to fragmentation (Sakurai et al., 2015) or turbulence in the disk can produce such stars. However, blue SMS spectra require corrections due to absorption by their atmospheres before the flux that exits the accretion envelope can be calculated. SMSs could also be found at higher redshifts if they exhibit pulsations that temporarily boost their fluxes above the detection limits of the wide-field surveys. Although current stellar evolution codes use implicit solvers and large time steps that do not resolve such oscillations, they can cause the star to periodically brighten and dim by an order of magnitude on timescales of a few weeks in the rest frame. Such variations might also facilitate their detection because their regularity would differentiate them from dusty, red high-z quasars or low-z impostors such as exoplanets. Periodic dimming and brightening could also flag these objects as high-z SMSs in transient surveys proposed for *JWST* such as FLARE (Wang et al., 2017).

DCBH birth may be the next stage of primordial quasar evolution, and

a number of studies have considered their prospects for detection in future NIR surveys. These are also deeply imbedded objects in dense, atomically-cooled flows and radiative transfer techniques similar to those we have used here are required to model their spectra. One-dimensional radiation hydrodynamics simulations of DCBH emission post processed with Cloudy have shown that they could be detected by *JWST* out to $z \sim 20$ (Becerra et al., 2015; Natarajan et al., 2017). We are now post processing radiation hydrodynamical simulations of the H II region of a SMBH from $z = 6$ - 20 (Smidt et al., 2018) with Cloudy to determine out to what redshifts it could be found by *Euclid, WFIRST and JWST*.

Chapter 4

On the detection of supermassive primordial stars. II. Blue supergiants

4.1 Abstract

Supermassive primordial stars in hot, atomically-cooling haloes at $z \sim 15$ - 20 may have given birth to the first quasars in the universe. Most simulations of these rapidly accreting stars suggest that they are red, cool hypergiants, but more recent models indicate that some may have been bluer and hotter, with surface temperatures of 20,000 - 40,000 K (Woods et al., 2017; Haemmerlé et al., 2018a; Sakurai et al., 2016a). These stars have spectral features that are quite distinct from those of cooler stars and may have different detection limits in the near infrared (NIR) today. Here, we present spectra and AB magnitudes for hot, blue supermassive primordial stars calculated with the TLUSTY and CLOUDY codes. We find that photometric detections of these stars by *JWST* will be limited to $z \lesssim 10$ - 12, lower redshifts than those at which red stars can be found, because of quenching by their accretion envelopes. With moderate gravitational lensing, *Euclid* and *WFIRST* could detect blue supermassive stars out to similar redshifts in wide-field surveys.

4.2 Introduction

Supermassive stars (SMSs) have long been the subject of analytical studies (e.g., Iben, 1963; Chandrasekhar, 1964; Fowler, 1964, 1966) and numerical simulations (e.g., Appenzeller & Fricke, 1972; Shapiro & Teukolsky, 1979; Fuller et al., 1986; Baumgarte & Shapiro, 1999; Sun et al., 2018; Butler et al., 2018). But credible scenarios for their formation have only recently been found: supermassive primordial star (SMS) formation in atomically-cooling primordial haloes at high redshifts exposed to either unusually strong Lyman-Werner (LW) UV fluxes (Latif et al., 2014b; Agarwal et al., 2016b; Chon et al., 2017; Wise et al., 2019) or highly supersonic baryon streaming motions (Latif et al., 2014a; Hirano et al., 2017; Schauer et al., 2017) or the formation of stars powered by self-annihilation of dark matter ('dark stars'; Spolyar et al., 2008; Freese et al., 2008). Strong UV backgrounds or streaming motions can suppress star formation in a halo until it reaches masses of $\sim 10^7\ M_\odot$ and virial temperatures of $\sim 10^4$ K that trigger rapid atomic cooling. This leads to catastrophic baryon collapse that can build up a star at rates of up to $\sim 1\ M_\odot\ \mathrm{yr}^{-1}$ (Lodato & Natarajan, 2006; Wise et al., 2008; Regan & Haehnelt, 2009b; Inayoshi et al., 2014; Latif & Volonteri, 2015). Such stars may have been the origin of the first quasars, a few of which have now been discovered at $z > 7$ (Mortlock et al., 2011; Bañados et al., 2018; Smidt et al., 2018).

Stellar evolution models indicate that primordial (Pop III) stars growing at these rates can reach masses of a few $10^5\ M_\odot$ before, in most cases, collapsing to black holes (direct collapse black holes, or DCBHs; Umeda et al., 2016; Woods et al., 2017; Haemmerlé et al., 2018b; Haemmerlé & Meynet, 2019). A few non-accreting Pop III SMSs may explode as thermonuclear transients (Montero et al., 2012; Whalen et al., 2013b; Johnson et al., 2013b; Whalen et al., 2013d, 2014; Chen et al., 2014). Pop III SMSs are the leading candidates for the origin of the earliest supermassive black holes (SMBHs) because the environments of ordinary Pop III star BHs are hostile to rapid growth (Whalen et al., 2004; Alvarez et al., 2009; Whalen & Fryer, 2012;

Smith et al., 2018). In contrast, DCBHs are born with much larger masses and in much higher densities in host galaxies capable of retaining their fuel supply even when it is heated by X-rays (Johnson et al., 2013a). But Pop III star BHs, in principle, could reach large masses by super- or hyper-Eddington growth if there is enough gas to fuel their rapid growth (Madau et al. 2014; Volonteri et al. 2015; Pezzulli et al. 2016; Inayoshi et al. 2016 – see Mayer et al. 2015; Mayer & Bonoli 2019 for other pathways to the formation of these quasars and Valiante et al. 2017; Woods et al. 2018 for recent reviews on the first quasars).

Most studies have found that rapidly accreting Pop III stars evolve as cool, red hypergiants along the Hayashi limit, with surface temperatures of 5,000 - 10,000 K due to H^- opacity in their atmospheres, at least until they reach $\sim 10^5\ M_\odot$ (Hosokawa et al., 2013). Haemmerlé et al. (2018a) found that SMSs can remain cool even above these masses and reach luminosities $\gtrsim 10^{10}\ L_\odot$. But Woods et al. (2017) found that SMSs evolving from similar initial conditions quickly settle onto hotter, bluer tracks with temperatures of 20,000 - 40,000 K. Haemmerlé et al. (2018a) found that Pop III SMSs accreting at low rates ($\lesssim 0.005\ M_\odot\ \mathrm{yr};^{-1}$) also evolve along blue tracks, as may stars with clumpy accretion due to fragmentation or turbulence in the accretion disk (Sakurai et al. 2015 – but see Sakurai et al. 2016a). Whether these differences are due to opacities, code physics (such as the numerical treatment of convection), accretion physics and boundary conditions, or numerical resolution remains unknown.

What are the prospects for observing blue Pop III SMSs today? Johnson et al. (2012) semi-analytically examined the spectral features of similar stars and predicted that they would be characterized by strong Balmer emission and the conspicuous absence of Lyα lines due to absorption by their envelopes. The source of this flux was the hypercompact H II region of the star, whose ionising UV was trapped close to its surface by the density and ram pressure of the inflow (which has also been found to be true in cosmological simulations of highly-resolved atomically-cooled haloes; Becerra et al., 2018).

Freese et al. (2010), Zackrisson et al. (2010a), Zackrisson et al. (2010b) and Ilie et al. (2012) modeled the spectra of hot, blue Pop III dark stars. They found that these objects could be observed today even by $8-10\,\mathrm{m}$ telescopes on the ground, primarily because of their high surface temperatures (20,000 - 30,000 K), larger masses (up to $10^7\ M_\odot$) and longer lives (up to 10^7 yr; see also recent reviews by Freese et al., 2016; Banik et al., 2018). Most recently, Surace et al. (2018) calculated spectra for cool, red SMSs and found that some will be visible to the *James Webb Space Telescope* (*JWST*; Gardner et al., 2006; Kalirai, 2018) at $z \lesssim 20$ and at $z \sim 10$ - 12 to *Euclid* (Laureijs et al., 2011) and the *Wide-Field Infrared Space Telescope* (*WFIRST*; Spergel et al., 2015) if they are gravitationally lensed. Hartwig et al. (2018) also found that the relics of such stars would be uniquely identifiable with the gravitational wave detector LISA at $z > 15$ if they form in binaries.

There are two challenges to modeling spectra for blue SMSs. First, unlike the cool, red stars in Surace et al. (2018), blue SMSs cannot be approximated as blackbodies (BBs) because they have much higher ionising fluxes due to their higher surface temperatures, and much of this flux is absorbed by their own atmospheres. Second, these stars are deeply embedded in hot, dense, accretion shrouds that reprocess flux from the star into longer wavelengths. Accurate spectra for blue SMSs require both stellar atmosphere models and radiative transfer through the envelope of the star. Such spectra are crucial to predicting detections of blue SMSs at high redshift, which would capture primordial quasars at the earliest stages of their development. Here, we calculate spectra and NIR magnitudes for hot, blue Pop III SMSs at high redshift with the TLUSTY and Cloudy codes. Our models are described in Section 4.3, and we discuss spectra, NIR magnitudes and detection rates for blue SMSs in Section 4.4. We conclude in Section 4.5.

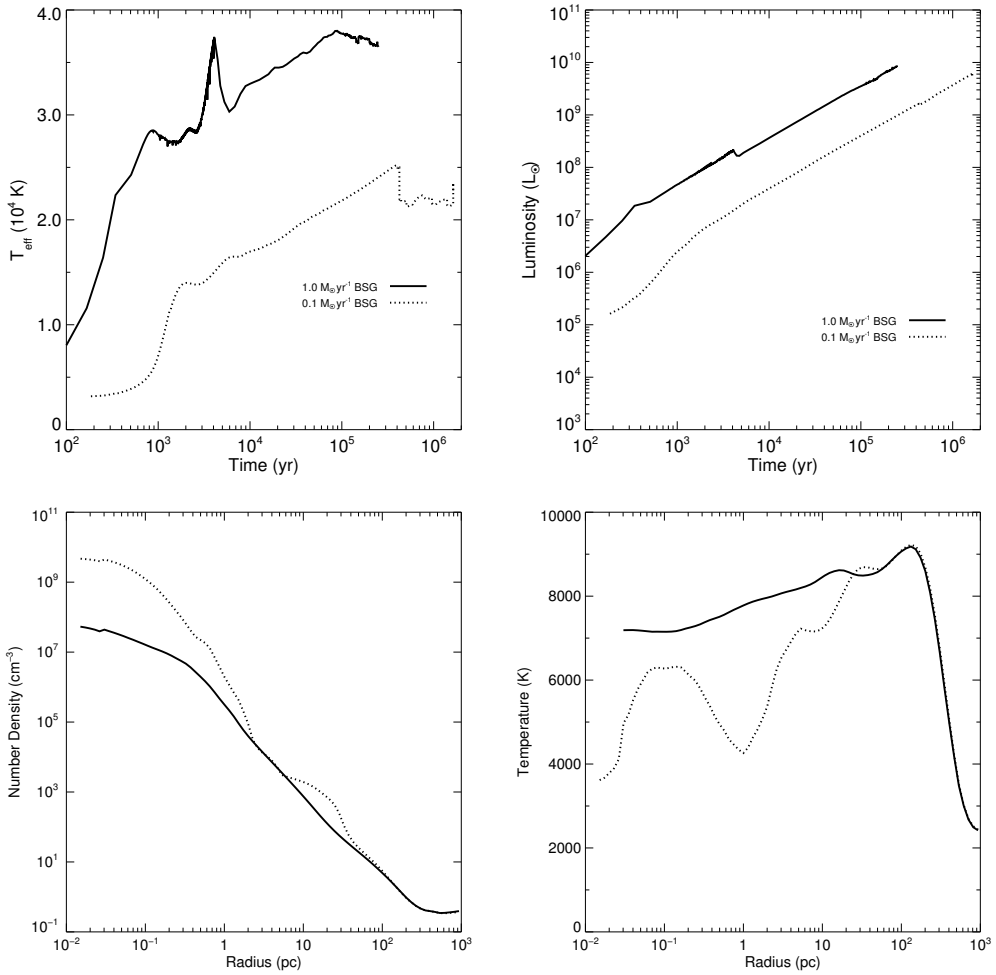

Figure 4.1: Top row: evolution of SMSs accreting at 1.0 and 0.1 $M_\odot$ yr^{-1} in our Kepler models. Left panel: surface temperatures. Right panel: luminosities. Evolution lines for the two stars end at different times because the less rapidly accreting star lives for a much longer time. Bottom row: spherically-averaged profiles of the dense, atomically-cooled shroud surrounding the star 0.238 Myr after the formation of the accretion disk. Left: gas densities. Right: temperatures.

4.3 Numerical Method

We model the atmospheres and spectra of blue SMSs with the TLUSTY code (Hubeny & Lanz, 1995) and how their accretion envelopes reprocess these spectra with the Cloudy code (Ferland et al., 2017). The emergent spectra are then cosmologically redshifted and convolved with filter functions to obtain their NIR AB magnitudes today.

4.3.1 TLUSTY Atmosphere Models

We consider SMSs accreting at 1.0 $M_{\odot}$ yr^{-1} and 0.1 $M_{\odot}$ yr^{-1} as fiducial cases. These stars were evolved in the Kepler stellar evolution code and discussed in detail in Woods et al. (2017). Surface temperatures, $T_{\rm eff}$, and bolometric luminosities for both stars over their lifetimes are shown in the upper row of Figure 4.1. The spectrum of the 1.0 $M_{\odot}$ yr^{-1} star was calculated at 1.51 $\times$ 10^5 yr, about halfway through its lifetime of 2.51 $\times$ 10^5 yr, when it has a mass of 1.51 $\times$ 10^5 $M_{\odot}$ and a surface temperature $T_{\rm eff}$ = 36,963 K. The spectrum of the 0.1 $M_{\odot}$ yr^{-1} star was calculated at 8.01 $\times$ 10^5 yr, about halfway through its lifetime of 1.63 $\times$ 10^6 yr, when it has a mass of 8.01 $\times$ 10^4 $M_{\odot}$ and a $T_{\rm eff}$ = 22,093 K. The bolometric luminosities of the two SMSs are 1.89 $\times$ 10^{43} erg s^{-1} and 1.13 $\times$ 10^{43} erg s^{-1}, respectively. As in Surace et al. (2018), we neglect the luminosity of the accretion shock at the surface of the stars because it is negligible at the velocities and densities of the infall onto the star (at most $\sim$ 10^4 $L_{\odot}$).

The TLUSTY code is used to calculate model stellar atmospheres in radiative and hydrostatic equilibrium, and also allows for convection. Departures from local thermodynamic equilibrium (LTE) are allowed for a set of occupation numbers of selected atomic and ionic energy levels. It solves the equations of radiative transfer, hydrostatic equilibrium, radiative equilibrium, statistical equilibrium, charge and particle conservation. The user must specify the stellar surface temperature, surface gravity, chemical composition (for the first 30 elements), and atomic data for selected species allowed to

contribute to the total opacity.

The surface gravities of these stars are $\log(g) \approx 3.148$ and $\log(g) \approx 2.203$ for the 1.0 $M_\odot$ yr^{-1} and 0.1 $M_\odot$ yr^{-1} SMSs, respectively. TLUSTY has great difficulties converging for surface gravities as low as these, and we have therefore settled for spectra generated using TLUSTY v.205 with $\log(g) = 3.25$ and 2.35 (i.e., offsets by $\Delta\log(g) \approx 0.1$ and 0.15). The stellar atmospheres are based on non-LTE, zero metallicity and primordial abundances of H and He. The resulting TLUSTY spectra have then been rescaled to match the actual bolometric luminosites of the two stars. Comparisons to zero-metallicity models with similar temperatures (but somewhat lower surface gravities) in the publicly available TLUSTY grids of Lanz & Hubeny (2003) and Lanz & Hubeny (2007) do not reveal significant problems due to these $\log(g)$ discrepancies, although we cannot rule out the possibility that we are slightly underestimating the ionizing flux in the case of the 0.1 $M_\odot$ yr^{-1} model.

4.3.2 Cloudy Models

We use the TLUSTY spectra of both stars as the input spectra in our Cloudy models of the flux that emerges from the accretion envelopes of the stars, whose spherically-averaged density and temperature profiles are shown in the bottom row of Figure 4.1. They are taken from an Enzo cosmology code (Bryan et al., 2014) simulation of the collapse of an atomically cooled halo after the formation of the accretion disk that creates the star (see also Figure 2 of Surace et al., 2018). These envelope models do not account for feedback from the SMS perturbing the structure of the infalling gas, but it is not expected to be important because ionizing radiation from the star is trapped close to its surface, as we discuss in the next section. We surround the 1.0 $M_\odot$ yr^{-1} SMS with the profile at 0.238 Myr after the formation of the disk and the 0.1 $M_\odot$ yr^{-1} SMS with the profile at 1.738 Myr because the envelope has time to build up to higher central densities with the more slowly accreting star. These profiles are tabulated in Cloudy with 70 bins that are uniformly partitioned in log radius, with inner and outer boundaries

at 0.015 pc and 927 pc. The temperatures in the envelope are set by the virialization of cosmic flows well above it rather than by radiation from the star because ionising UV from the star is confined to very small radii deep in the cloud. Since these temperatures determine to what degree the envelope is collisionally excited, and therefore how it reprocesses photons from the star, we require Cloudy to use the Enzo temperatures for the envelope instead of inferring them from the spectrum of the star.

Cloudy then solves the equations of radiative transfer, statistical and thermal equilibrium, ionisation and recombination, and heating and cooling to determine the excitation and ionisation state of the gas surrounding the star and calculate its emergent spectrum. These calculations use tables of recombination coefficients from Dere et al. (1997) and Landi et al. (2011) and ionic emission data from Badnell et al. (2003) and Badnell (2006). Each spectrum has 8228 bins that are uniformly partitioned in log λ. We convert the luminosity in each bin, $L(\lambda) = \lambda L_\lambda$ in erg s^{-1}, to the flux density, F_λ in erg s^{-1} cm^{-2} μm^{-1}, needed to compute AB magnitudes (equations 1 - 3 in Rydberg et al., 2018) by

$$F(\lambda) = \frac{L\left(\frac{\lambda}{1+z}\right)}{\frac{\lambda}{1+z}(1+z)4\pi d_{\rm L}^2(z)}. \tag{4.1}$$

Here, λ is the wavelength in the observer frame and $d_{\rm L}(z)$ is the luminosity distance:

$$d_{\rm L}(z) = (1+z)c/{\rm H}_0 \int_0^z \frac{1}{\sqrt{\Omega_{\rm M}(1+z)^3 + \Omega_\lambda}} dz. \tag{4.2}$$

This is done to conform to the Cloudy convention that

$$\sum_\lambda \frac{L(\lambda)}{\lambda}\Delta\lambda = L_{\rm bol}. \tag{4.3}$$

AB magnitudes, $m_{\rm AB}$, in specific filters are then calculated from

$$m_{\rm AB} = -2.5\log_{10}\frac{\int_0^\infty F(\lambda)T(\lambda)d\lambda}{\int_0^\infty F_0(\lambda)T(\lambda)d\lambda}. \tag{4.4}$$

Here, $T(\lambda)$ is the filter transmission function and $F_0(\lambda) = 3.630781 \times 10^{-20}$ $c\lambda^{-2}$ ergs cm^{-2} s^{-1} μm^{-1}, the reference spectrum for AB magnitudes. We

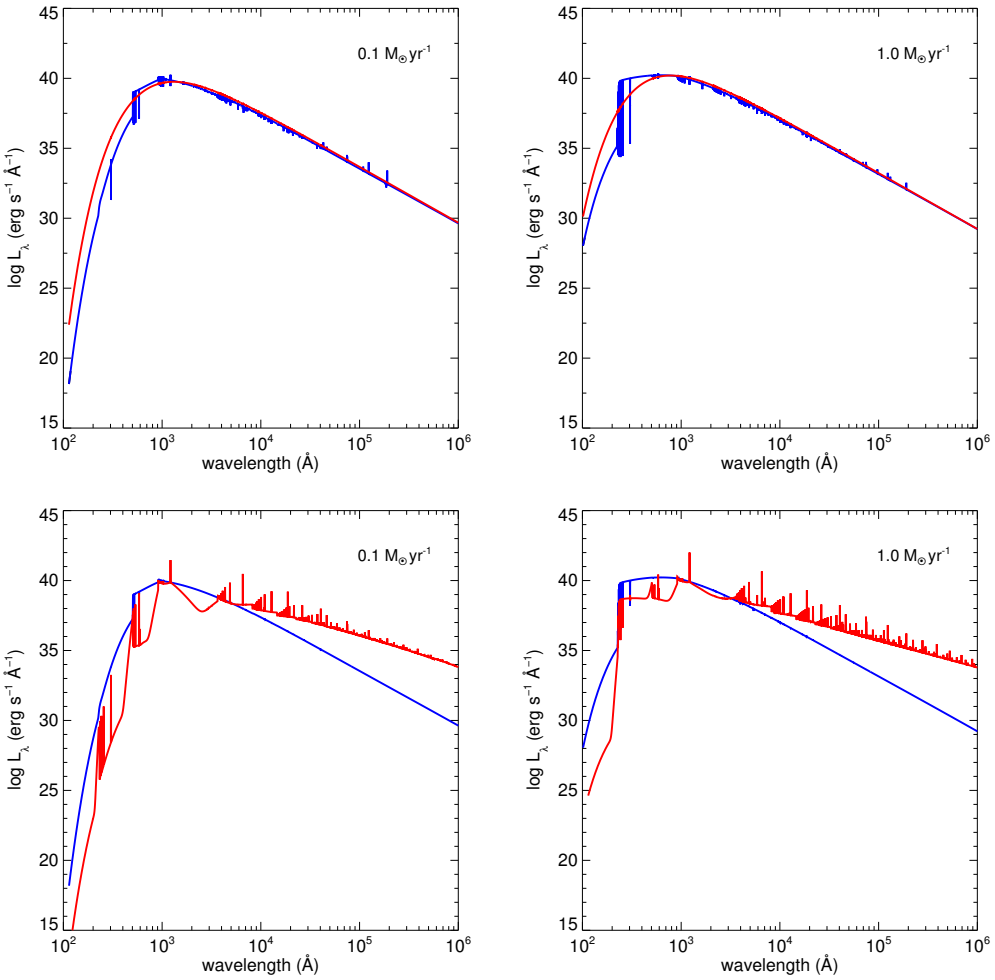

Figure 4.2: Top row: spectra of the two blue SMSs in our study. Red: uncorrected BB spectrum. Blue: TLUSTY model. Left: the 0.1 $M_\odot$ yr^{-1} star at 8.01 $\times$ 10^5 yr and $T_{\rm eff}$ = 22,093 K. Right: the 1.0 $M_\odot$ yr^{-1} star at 1.51 $\times$ 10^5 yr and $T_{\rm eff}$ = 36,963 K. Bottom row: spectra emerging from the accretion envelopes of the stars. Blue: incident stellar spectrum. Red: spectrum after reprocessing by the envelope. Left: the 0.1 $M_\odot$ yr^{-1} star. Right: the 1.0 $M_\odot$ yr^{-1} star.

assume cosmological parameters from the second-year *Planck* release: $\Omega_{\rm M} = 0.308$, $\Omega_\Lambda = 0.691$, $\Omega_{\rm b} = 0.0223$, $h = 0.677$, $\sigma_8 = 0.816$, and $n = 0.968$ (Planck Collaboration et al., 2016). Flux blueward of Lyα in the rest frame of the star is set to zero in the AB magnitude calculation because of absorption by the neutral IGM at $z > 6$.

4.4 Blue Supermassive Stars

4.4.1 Stellar Spectra

We compare TLUSTY spectra for the blue 0.1 $M_\odot$ yr^{-1} and 1.0 $M_\odot$ yr^{-1} stars to those of blackbodies at the same temperatures and luminosities in the upper panels of Figure 4.2. In both cases the atmosphere of the star has little effect on its spectrum at wavelengths redward of its blackbody peak except for some relatively weak emission and absorption lines, but the picture is different at shorter wavelengths. The sharp drops in luminosity at 504 Å in the 0.1 $M_\odot$ yr^{-1} star and at 227 Å in the 1.0 $M_\odot$ yr^{-1} star are due to the ionisation limits of He I and He II, respectively. Here the ionisation limits correspond to the minimum energy required to remove the outermost (valence) electron from the neutral He atom (He I) or ionized He (He II). There is virtually no absorption due to hydrogen just blueward of its ionisation limit except for small features at 912 Å because most of it has been been ionised by the star. There is a weak Lyα line at 1216 Å and Hα and weak Paschen lines at 6560 Å, 12800 Å, and 18,800 Å.

4.4.2 Reprocessed Spectra

We show Cloudy spectra for the two stars after absorption and re-emission by their accretion envelopes in the bottom row of Figure 4.2. The ionizing UV fluxes of the 0.1 and 1.0 $M_\odot$ yr^{-1} stars are trapped at radii of 0.033 pc and 0.02 pc in our Cloudy models. These are the resolution limits of the Enzo model at 0.238 and 1.738 Myr, so as expected the strong inflows quench the

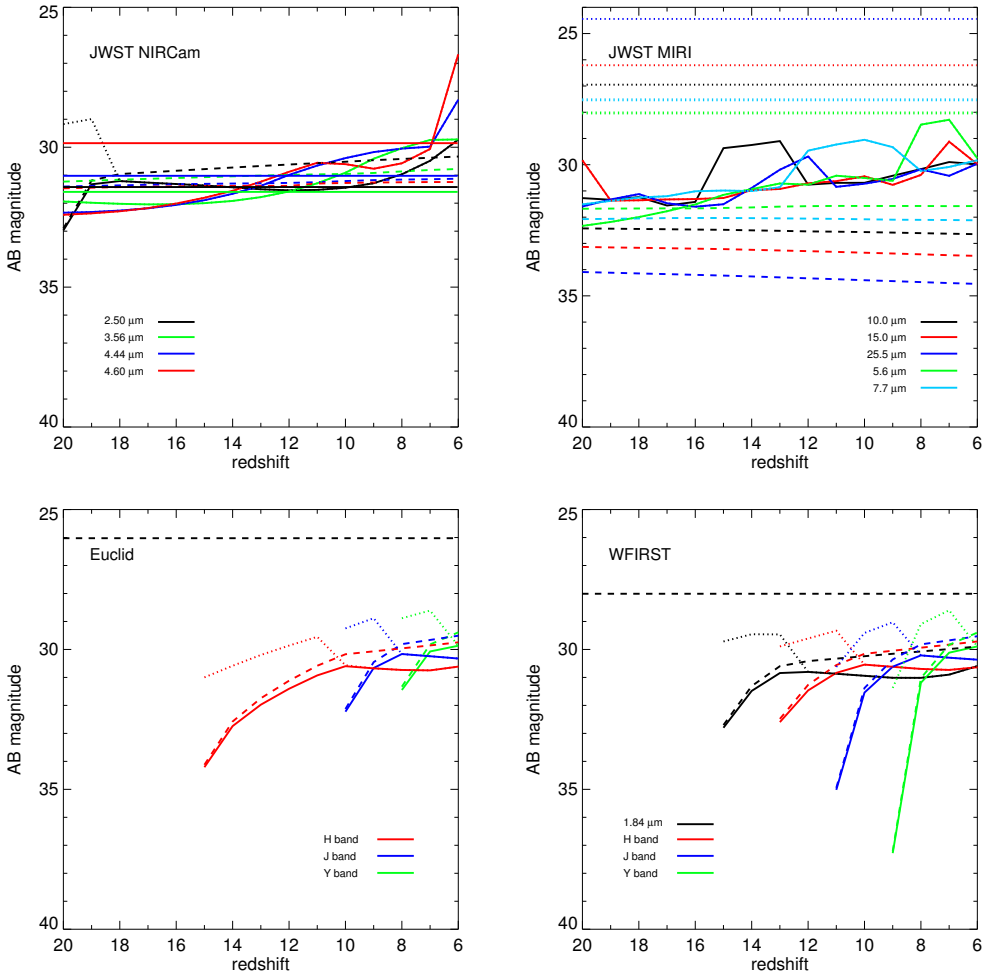

Figure 4.3: NIR AB magnitudes for the 1.0 $M_{\odot}$ yr^{-1} blue SMS in *JWST*, *Euclid* and *WFIRST* bands. Solid line: with the accretion envelope but no contribution from its Lyα line. Dashed line: no envelope. Dotted line: with the envelope and its Lyα line. Top left: *JWST* NIRCam bands. Top right: *JWST* MIRI bands. Bottom left: *Euclid filters*. Bottom right: *WFIRST filters*. The horizontal lines are the 5σ AB magnitude detection limits for 100 hour exposures in the filter of the corresponding colour for the *JWST* filters, and the detection limits for deep-drilling fields in *Euclid* and *WFIRST*.

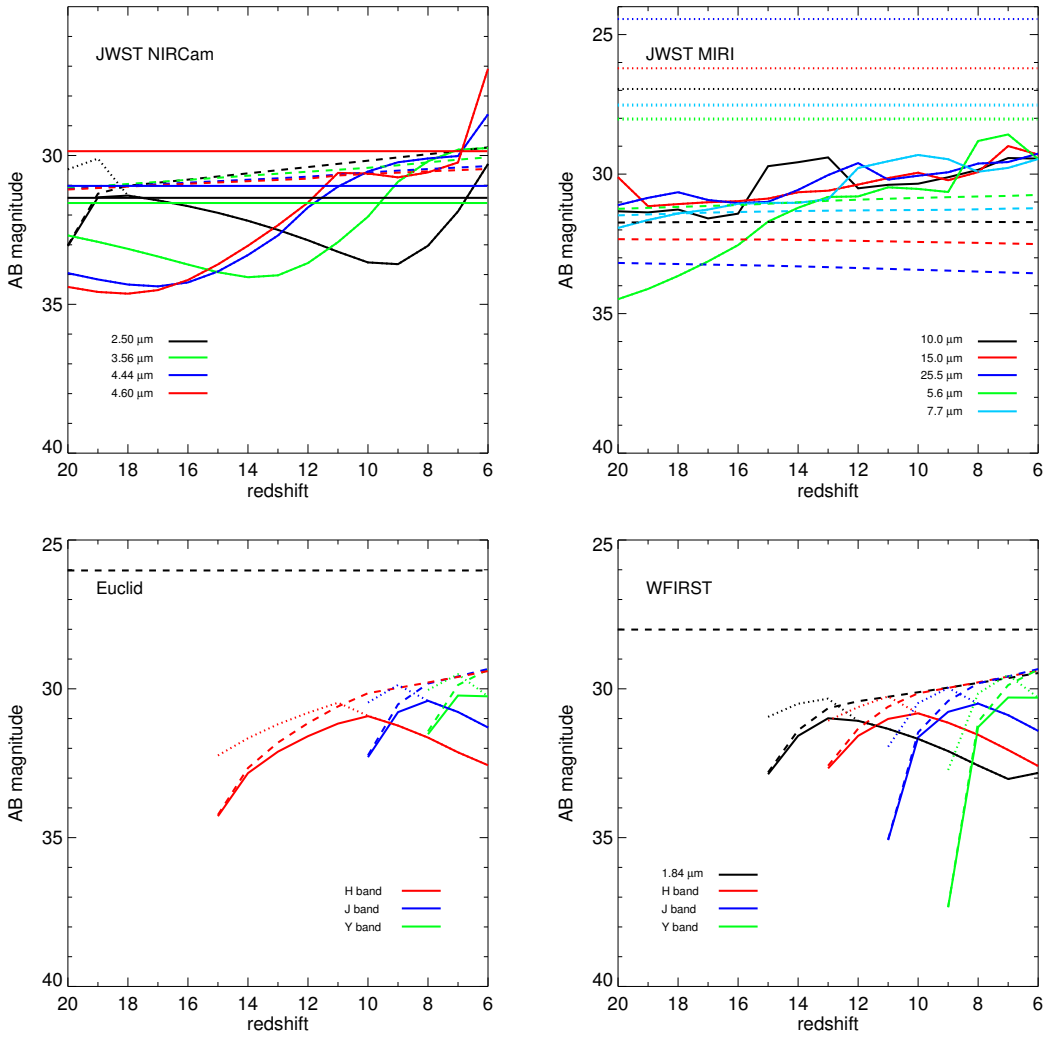

Figure 4.4: NIR AB magnitudes for the 0.1 $M_{\odot}$ yr^{-1} blue SMS in *JWST*, *Euclid* and *WFIRST* bands. Solid line: with the accretion envelope but no contribution from its Lyα line. Dashed line: no envelope. Dotted line: with the envelope and its Lyα line. Top left: *JWST* NIRCam bands. Top right: *JWST* MIRI bands. Bottom left: *Euclid filters*. Bottom right: *WFIRST filters*. The horizontal lines are the 5σ AB magnitude detection limits for 100 hour exposures in the filter of the corresponding colour for the *JWST* filters, and the detection limits for deep-drilling fields in *Euclid* and *WFIRST*.

ionizing UV of both stars. Strong continuum absorption due to ionisation of neutral H is evident below 912 Å, with additional steps in absorption at 504 Å and 227 Å due to the ionisation of He I and He II, respectively. These features are stronger with the 0.1 $M_\odot$ yr^{-1} star than the 1.0 $M_\odot$ yr^{-1} star because its envelope has collapsed to higher central densities by 1.786 Myr. Strong Hα and Paschen emission lines are visible at 6560 Å, 12800 Å, and 18800 Å. Most absorption blueward of the Lyman limit is re-emitted as the continuum and numerous lines at wavelengths above 5000 Å.

In contrast to the red stars in Surace et al. (2018), absorption and re-emission by the accretion envelopes of blue stars do not enhance their spectra in most of the bands that would be redshifted into the NIR today. A potential exception is Lyα: in contrast to red SMSs, both spectra exhibit very strong Lyα emission lines that are pumped by the much higher UV fluxes of the blue stars. Although these lines are strong it is not clear how much of this Lyα flux would be observed in the NIR today, for two reasons. First, many of the Lyα photons would be resonantly scattered by the neutral IGM into a halo of large radius but low surface brightness, so the star might not appear to be a strong point source of this flux. Second, repeated resonant scatterings broaden the line over time so some of the flux in principle could fall outside a given filter after being redshifted into the NIR today. This is not expected to be a large effect because the Lyα photons are only scattered at most $\sim$ 3% from line center before their optical depth in the wings falls below unity and they stream freely through the universe (Smith et al., 2015a). If the maximum displacement of the photon from line center is $0.03\lambda_0 = 36$ Å in the rest frame it would be ~ 0.04 μm for a $z = 10$ SMS, or about an order of magnitude smaller than the typical width of *JWST* wide band NIR filters. A detailed treatment of Lyα radiative transfer in the primordial IGM is beyond the scope of this paper so we calculate AB magnitudes for the stars with and without the Lyα line as upper and lower limits.

4.4.3 NIR Magnitudes

NIR magnitudes for the 1.0 $M_{\odot}$ yr^{-1} blue SMS in *JWST*, *Euclid* and *WFIRST* bands are plotted in Figure 4.3. We consider three cases: i) stars with accretion envelopes but no Lyα line; ii) stars with accretion envelopes and their Lyα lines; iii) stars with no envelopes. This latter case is in the event that ionising UV radiation from the star or other dynamical effects such as gravitational torqueing from nearby haloes strip away the envelope of the star. At 2.5 - 4.6 μm the magnitudes with and without the Lyα line are indistinguishable out to z =18, when it begins to be redshifted into the 2.5 μm *JWST* NIRCam filter, leading to an increase in brightness of about two magnitudes. A similar effect is visible in this filter with the 0.1 $M_{\odot}$ yr^{-1} star in Figure 4.4 but is less prominent because the Lyα line from its envelope is weaker.

From $z \sim$ 14 - 20 the envelope of the 1.0 $M_{\odot}$ yr^{-1} star somewhat suppresses flux from the star but enhances it at $z < 13$, especially at $z < 7$ where reprocessed radiation redward of 5000 Å enhances brightnesses by 3 - 4 magnitudes. Similar enhancements are evident with the 0.1 $M_{\odot}$ yr^{-1} star at the same redshifts. Absorption in the NIR by the denser envelope of the 0.1 $M_{\odot}$ yr^{-1} star is more severe, decreasing its brightness down to $z \sim 7$. In contrast, reprocessing of the spectra redward of 5000 Å by the envelopes of both stars makes them more visible at 7.7 - 25.5 μm at nearly all redshifts, but their magnitudes remain well below MIRI detection limits. NIRCam AB magnitude limits of $\sim$ 31 will effectively limit detections of the 1.0 and 0.1 $M_{\odot}$ yr^{-1} stars by *JWST* to $z \sim$ 12 and 10, respectively.

The 1.0 $M_{\odot}$ yr $^{-1}$ star is brighter by $\sim$ 2 magnitudes in the *Euclid* and *WFIRST* filters with the Lyα line than without it at redshifts over which it is shifted into these filters, as shown in the lower panels of Figure 4.3. The 0.1 $M_{\odot}$ yr^{-1} star is about one magnitude brighter. Exclusion of this line results in brightnesses that are consistently lower than those for stars without envelopes, and this effect is especially pronounced at lower redshifts where quenching by the envelope is greatest. Quenching at low redshifts

is greatest with the 0.1 $M_\odot$ yr^{-1} star because it has the denser envelope. The AB magnitudes of stars with envelopes but no Lyα never rise above 30 and could not be directly detected at $z \gtrsim 6$ with *Euclid* or *WFIRST*, whose practical detection limits are 26 and 28, respectively.

4.4.4 SMS Detection Rates

The number of SMSs per unit redshift per unit solid angle at a redshift z is

$$\frac{\mathrm{d}N}{\mathrm{d}z\mathrm{d}\Omega} = \dot{n}_{\mathrm{SMS}}\, t_{\mathrm{SMS}}\, r^2 \frac{\mathrm{d}r}{\mathrm{d}z}, \tag{4.5}$$

where $\dot{n}_{\mathrm{SMS}}$ is the SMS formation rate per unit comoving volume, t_{SMS} is the average lifetime of an SMS, which we take to be 1 Myr, and $r(z)$ is the comoving distance to redshift z,

$$r(z) = \frac{c}{H_0} \int_0^z \frac{\mathrm{d}z'}{\sqrt{\Omega_{\mathrm{m}}(1+z')^3 + \Omega_\Lambda}}. \tag{4.6}$$

Current estimates of $\dot{n}_{\mathrm{SMS}}$ vary by up to eight orders of magnitude (Woods et al., 2018), and these models also predict a variety of evolution of $\dot{n}_{\mathrm{SMS}}$ with redshift. Habouzit et al. (2016) find that the comoving number density of SMSs rises with decreasing z whereas Valiante et al. (2017) predict that most SMSs form in the narrow range $z \sim 16$ - 18.

As in Surace et al. (2018) we consider upper and lower limits for $\dot{n}_{\mathrm{SMS}}$. The upper limit is the low J_{crit} model of Habouzit et al. (2016), in which most SMSs form at $z \sim 10$ - 12 and the final comoving SMS number density is $\sim 10^{-1}\,\mathrm{Mpc}^{-3}$. The lower limit is found by assuming that most SMSs form at $z \sim 16$ - 18, as in Valiante et al. (2017), with a final comoving number density of $\sim 10^{-8}\,\mathrm{Mpc}^{-3}$. The upper limit yields about 4×10^7 SMSs per steradian per unit redshift, or around 30 per NIRCam field of view. The lower limit on $\dot{n}_{\mathrm{SMS}}$ yields only ~ 10 SMSs per steradian per unit redshift, or at most 10^{-5} SMSs per NIRCam field of view. There is also some uncertainty in SMS detection rates due to their range of lifetimes, but it is small compared to the uncertainty in $\dot{n}_{\mathrm{SMS}}$.

At present, the relative numbers of blue and red SMSs are not known. Although most studies so far have found rapidly accreting SMSs to have extended red envelopes, the codes used to model their evolution lack detailed radiation hydrodynamics and opacities and can only approximate convective mixing, all of which can have profound effects on the structure of the star. Neither blue nor red SMSs have been found in the *Hubble* Ultra Deep Field to date because its AB mag limit is 29 at 1.38 μm, well below that expected of either type of star even at $z \sim 6$. Strategies for the direct detection of SMSs by *JWST*, *Euclid* and *WFIRST* are now under development (Whalen et al., 2019).

4.5 Discussion and Conclusion

In contrast to cooler, redder SMSs that can be found at $z \sim 18$ - 20, detections of hot, blue SMSs by *JWST* will be limited to $z \lesssim 10$ - 12 due to quenching by their accretion envelopes. Likewise, these stars cannot be directly detected by *Euclid* or *WFIRST* at $z \gtrsim 6$. This does not mean that these two missions cannot find blue SMSs because only moderate gravitational lensing is required to boost their fluxes above their detection limits. Their fields of view will enclose thousands of massive galaxies and galaxy clusters, and at $z \sim 6$ - 12 magnification factors of only 10 - 100 would be required to reveal either star. It is likely that a significant fraction of their wide fields will be magnified by such factors (e.g., Oguri & Marshall, 2010; Rydberg et al., 2018). Higher magnifications may be possible in future surveys of individual cluster lenses by *JWST* but at the cost of smaller lensing volumes (Whalen et al., 2013a; Windhorst et al., 2018) that enclose fewer objects.

How could blue rapidly accreting SMSs be distinguished from hot blue dark stars of similar mass and redshift? Perhaps the greatest distinction between the two objects is the dense accretion shroud of the SMS, which imprints prominent continuum absoption features on the its spectra redward

of Lyα in the rest frame that are absent from those of blue dark stars (compare Figures 2c and 2d to Figure 6 in Freese et al., 2016). In principle, these spectral features could be used to distinguish blue SMSs from hot dark stars of similar mass. Blue SMS spectra also exhibit very prominent Lyα lines due to pumping of the accretion envelope by high-energy UV photons from the star. Dark star spectra lack this feature because they do not have dense envelopes but, as discussed earlier, it is not clear if it could be detected today because of resonant scattering of Lyα by the neutral IGM at $z > 6$.

The photospheric temperatures of supermassive Pop III stars in atomically cooling haloes (whether they are red, blue, or both in the rest frame) remain an unsolved problem. Although numerical simulations to date broadly agree on the evolution and final fates of rapidly-accreting Pop III SMSs there are key differences between them that remain poorly understood, such as the growth of the convective core mass, the final masses of the most rapidly accreting objects, and the inflation of the photosphere. But there is a general consensus that these discrepancies likely arise from differences in how the models flag the onset of convection (i.e., the Schwarzschild or Ledoux criteria), their ability to follow dynamical instabilities (e.g., KEPLER) or not (e.g., GENEVA and Yorke & Bodenheimer, 2008), and their numerical resolution and boundary conditions at the surface.

Using a code derived from Yorke & Bodenheimer (2008), Hosokawa et al. (2013) found that H^- opacity in the outermost envelopes of SMSs can greatly expand their photospheres and limit their temperatures to ~ 0.5–1×10^4K until becoming blue at masses $\gtrsim 10^5 M_\odot$. Woods et al. (2017), however, find SMSs to be compact and blue from early times in the KEPLER stellar evolution code, without enough H^- in their atmospheres to expand and cool them. A third study by Haemmerlé et al. (2018a) with the GENEVA code found that rapidly-accreting SMSs are persistently red throughout their lifetimes, although more slowly-accreting ones may be blue (see discussion below). Efforts to benchmark these studies and converge on a solution continue (see, e.g., the recent review by Woods et al., 2018), but the final answer may only

come from observations like those proposed here.

Our Enzo simulations neglect the effect of radiation pressure due to flux from the star on the flows that create it. Including these effects in cosmological simulations is challenging because they must resolve photospheres, the inner regions of accretion disks, and how the two are connected on very small scales that prevent codes from evolving them for long times. Smith et al. (2017b) post processed simulations of highly-resolved atomically cooling haloes with Lyα photon transport and found it could alter flows onto the star. Radiation hydrodynamical calculations by Luo et al. (2018) and Ardaneh et al. (2018) without resonant Lyα scattering found that radiation from the protostar did not significantly alter local flows at early times but did suppress fragmentation, thus promoting the rapid growth of a single, supermassive object. There is somewhat more of a possibility that ionising flux from blue SMSs could blow out gas from the disk and partially expose it to the IGM, but this will simply result in AB magnitudes closer to those of the bare star shown in Figures 4.3 and 4.4.

Pulsations in blue or red SMSs (e.g., Osaki, 1966) could improve their prospects for detection by temporarily boosting their fluxes above the detection limits of surveys. This phenomenon is not captured by the stellar evolution codes used here because their implicit solvers and large time steps do not resolve such oscillations, but it might cause the star to periodically brighten and dim by an order of magnitude on timescales of a few weeks to months in the rest frame. These oscillations might also facilitate their detection because their regularity would differentiate them from dusty, red high-z quasars or low-z interlopers such as cool Milky Way stars. Periodic dimming and brightening in principle could flag high-z SMSs in transient surveys proposed for *JWST* such as FLARE (Wang et al., 2017).

The original studies on the collapse of pristine, atomically cooled haloes and the subsequent formation of SMSs assumed very high LW backgrounds that completely suppressed H_2 formation in their cores, so collapse was nearly isothermal at temperatures of $\sim$ 8000 K and flow rates of 0.1 - 1 $M_\odot$ yr^{-1}.

This is why we adopted them as the two fiducial rates in our study (they are also typical of the collapse of atomically cooled haloes due to supersonic baryon streaming motions; Hirano et al., 2017). But in lower LW backgrounds some H_2 can form in the core of the halo and enhance cooling there, leading to lower infall rates of a few 10^{-3} $M_\odot$ yr^{-1} (e.g., Latif et al., 2015; Regan & Downes, 2018). Such rates result in much less massive stars, perhaps 10^3 - 10^4 $M_\odot$ rather than 10^5 $M_\odot$. It is not clear at this point which of these two populations of SMS was more prevalent in the early universe because average LW background strengths are not well understood and supersonic streaming motions are thought to have produced about as many SMSs as LW backgrounds. Furthermore, it is not clear if these stars evolved along hot blue tracks or cool red ones, although there are indications that some would be blue (Haemmerlé et al., 2018a). The prospects for detection of this second, less massive population of SMSs are unclear because it is not yet known if they were red or blue and they evolved in accretion envelopes with lower densities than those considered here. But they may be more difficult to find because of their lower fluxes. They will be studied in future work.

DCBH birth after the collapse of the SMS is the next stage of primordial quasar evolution, and a number of studies have examined prospects for their detection in future NIR surveys. These objects are also deeply embedded in dense, hot flows and techniques similar to those used here are required to model their spectra. One-dimensional radiation hydrodynamics simulations of DCBH emission post processed with Cloudy have shown that they could be detected by *JWST* out to $z \sim 20$ (Pacucci et al., 2015; Natarajan et al., 2017). We will next post process radiation hydrodynamical simulations of the H II regions of DCBHs from $z = 10$ - 20 with Cloudy to find out to what redshifts they could be found by *Euclid, WFIRST and JWST*.

Chapter 5

Finding the First Quasars at Birth

5.1 Abstract

Direct collapse black holes (DCBHs) are currently the leading contenders for the origins of the first quasars in the universe. But the birth of a DCBH in an atomically-cooling halo does not by itself guarantee it will become a quasar by $z \sim 7$, the halo must also be located in cold accretion flows or later merge with a series of other gas-rich haloes capable of fueling the BH's rapid growth. Here, we present near infrared luminosities for DCBHs born in cold accretion flows in which they are destined to grow to 10^9 $M_\odot$ by $z \sim 7$. Our observables, which are derived from cosmological simulations with radiation hydrodynamics with Enzo, reveal that DCBHs could be found by the *James Webb Space Telescope* at $z \lesssim 20$ and strongly-lensed DCBHs could be found in future wide-field surveys by *Euclid* and *WFIRST* at $z \lesssim 15$.

5.2 Introduction

DCBHs may be the origins of the first quasars in the universe (e.g., Mortlock et al., 2011; Bañados et al., 2018). They are thought to form in primordial

haloes immersed in either strong LW UV fluxes (Agarwal et al., 2016b) or highly supersonic baryon streaming flows (Hirano et al., 2017; Schauer et al., 2017), either of which can prevent them from forming primordial (or Pop III) stars until they reach masses of 10^7 - 10^8 $M_\odot$ and virial temperatures of $\sim 10^4$ K that trigger rapid atomic H cooling. Atomic cooling causes gas to collapse at rates of up to ~ 1 $M_\odot$ yr^{-1}, forming an accretion disk that builds up a single, supermassive star at its center (Bromm & Loeb, 2003; Lodato & Natarajan, 2006; Wise et al., 2008; Regan & Haehnelt, 2009b; Latif et al., 2013) - although binaries or even small multiples are now thought to be possible; Latif et al. (2020)).

Stellar evolution models show that these stars can reach masses of a few 10^5 $M_\odot$ before collapsing to DCBHs via the general relativistic instability (Hosokawa et al., 2013; Umeda et al., 2016; Woods et al., 2017; Haemmerlé et al., 2018b), although a few for which accretion has shut down have been found to explode as highly energetic thermonuclear supernovae (Whalen et al., 2013d,c; Johnson et al., 2013b; Chen et al., 2014). DCBHs are currently the leading candidates for the seeds of the first supermassive black holes (SMBHs) because they are born with large masses in high densities in haloes that can retain their fuel supply, even when heated by X-rays (Johnson et al. 2013a – see Valiante et al. 2017; Woods et al. 2018 for recent reviews). In contrast, while Pop III star BHs in principle can reach 10^9 $M_\odot$ with periodic episodes of super- or hyper-Eddington accretion (Madau et al., 2014; Volonteri et al., 2015; Pezzulli et al., 2016; Inayoshi et al., 2016; Sakurai et al., 2016b), their environments are hostile to such growth (Whalen et al., 2004; Alvarez et al., 2009; Whalen & Fryer, 2012; Smith et al., 2018).

What are the prospects for detecting DCBHs, and thus the birth of the first quasars? Using one-dimensional (1D) radiation hydrodynamical models, Pacucci et al. (2015) predicted that DCBHs could be detected by *JWST* at $z \sim 25$ and by the Advanced Telescope for High-Energy Astrophysics (ATHENA) at $z \sim 15$. Natarajan et al. (2017) used such models to develop criteria for distinguishing the host galaxies of DCBHs from those of other

SMBH seeds at $z \sim 10$, showing that *JWST* can distinguish between seeding mechanisms at this redshift. But these models assume idealized host haloes and neglect the cold flows required for the BHs to later become quasars by $z \sim 7$. Like the supermassive stars from which they form, DCBHs are deeply imbedded in these flows and they can heavily reprocess radiation from the BH in ways that could not be considered in previous studies, impacting their rest frame spectra and luminosities in the NIR today.

Here, we calculate NIR luminosities for a DCBH at birth in cosmological environments that lead to its evolution into a quasar by $z = 7$ with high-resolution radiation hydrodynamical simulations. Rather than assuming a grid of accretion rates for the BH, ours are an emergent feature of the simulations. Our models also capture the anisotropy of X-ray breakout into the early intergalactic medium (IGM) and how it affects their detection today. In Section 5.3 we describe our cosmological simulations and how we extract AB magnitudes for the BH from them. DCBH spectra and AB magnitudes for a variety of *JWST*, *Euclid* and *WFIRST* bands are examined in Section 5.4, and we conclude in Section 5.5.

5.3 Numerical Method

We first extract luminosities and H II region profiles for the DCBH from Smidt et al. (2018), which was done with the Enzo adaptive mesh refinement (AMR) cosmology code (Bryan et al., 2014). They are then post processed with Cloudy (Ferland et al., 2017) to obtain rest frame BH spectra. These spectra are then cosmologically redshifted and dimmed, corrected by absorption by the neutral IGM at $z > 6$, and convolved with telescope filter functions to compute AB magnitudes in a variety of NIR bands as a function of source redshift.

5.3.1 Enzo Model

Here we briefly review our Enzo simulation. We found a 100 h^{-1} Mpc box

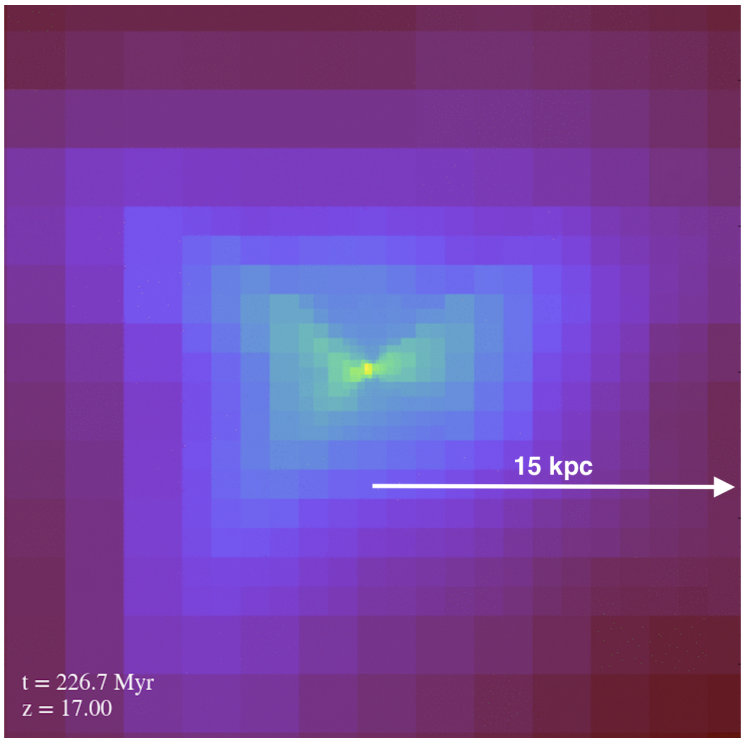

Figure 5.1: Ionized H fraction in the vicinity of the DCBH $z = 17$. The image is 30 kpc proper on a side.

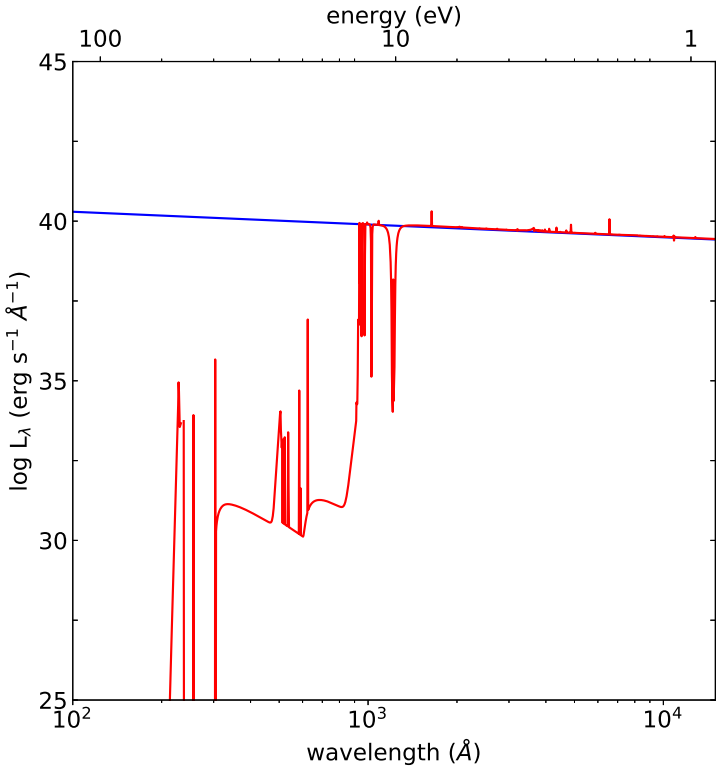

Figure 5.2: Rest frame spectra for the DCBH at $z = 19$ before (blue) and after (red) reprocessing by its host halo.

that contains a halo that grows to 1.2×10^{12} $M_\odot$ by $z = 7$ by accretion rather than by major mergers. We then centered three nested grids on this halo, resimulated it down to $z = 19.2$, when it reaches a mass of 3×10^8 $M_\odot$ and begins to atomically cool, placed a 10^5 $M_\odot$ DCBH at its center, and turned on X-rays. Our root grid was 256^3 and the nested grids were 25 h^{-1} Mpc each for an effective resolution of 2048^3. The initial dark matter particle mass resolution was 8.41×10^6 h^{-1} $M_\odot$.

We initialized the grid with gaussian primordial density fluctuations at $z = 200$ with MUSIC (Hahn & Abel, 2011) with cosmological parameters from the second-year *Planck* best fit lowP+lensing +BAO+JLA+H_0: $\Omega_{\rm M} = 0.308$, $\Omega_\Lambda = 0.691$, $\Omega_{\rm b} = 0.0223$, $h = 0.677$, $\sigma_8 = 0.816$, and $n = 0.968$ (Planck Collaboration et al., 2016). Our maximum refinement level $l = 10$ produced a maximum resolution of 35 pc (comoving), which was sufficient to resolve the gas flows and radiation transport deep in the halo. Given that only one or two dozen haloes per Gpc^{-3} are expected to reach $\sim 10^{12}$ $M_\odot$ by $z \sim 7$ by smooth accretion (Di Matteo et al., 2012; Feng et al., 2014a), our 100 h^{-1} Mpc box was the smallest one that could enclose such a reservoir in a reasonable number of tries.

The refinement criteria used to trigger refinement in Enzo were based on three physical quantities: the DM particle overdensity, the baryon overdensity, and the Jeans length. The first two criteria refine the root grid when the overdensity of a grid cell with respect to the mean density exceeds 3.0 for baryons and/or DM. According to the Truelove criterion, the local Jeans length should be resolved with at least 4 cells at all times to avoid artificial fragmentation during collapse (Truelove et al., 1997). However, Federrath et al. (2011), Turk et al. (2012), and Latif et al. (2013) have all shown that simulations require a minimum Jeans length resolution of 32 cells in order to obtain converged turbulent energy results, which is the resolution that we therefore adopt.

X-rays from the BH are propagated with the MORAY ray tracing code (Wise & Abel, 2011) and are self-consistently coupled to hydrodynamics and

nine-species nonequilibrium primordial gas chemistry in Enzo. This physics is key to capturing the onset of SF in the primordial galaxy because free electrons due to secondary ionizations by energetic photoelectrons, which are included in the chemistry and energy equations, catalyze the formation of H_2, which cools gas and creates stars (see, e.g., Machacek et al., 2003). MORAY includes radiation pressure on gas due to photoionizations, and Compton heating by X-rays and primordial gas cooling are included in the energy equation: collisional excitational and ionizational cooling by H and He, recombinational cooling, bremsstrahlung cooling, H_2 cooling, and inverse Compton cooling by the cosmic microwave background.

The BH was represented by a sink particle with a 1 keV X-ray luminosity $L_{\rm r} = \epsilon_{\rm r}\dot{m}_{\rm BH}c^2$, where $\epsilon_{\rm r}$, the mean radiative efficiency, is 0.1, and $\dot{m}_{\rm BH}$ is the accretion rate. Because our simulations did not resolve the accretion disk of the BH, we used an alpha disk model to compute $\dot{m}_{\rm BH}$ to approximate the transport of angular momentum out of the disk on subgrid scales. Although stochastic star formation, which includes winds, ionizing UV and supernovae due to stars, was turned on at the same time as X-rays from the BH, no stars formed in the short times we examine the DCBH here so its host halo is still free of metals. We also turned on a uniform LW background due to a global population of primordial stars that evolved with redshift. An image of the H II region of the DCBH at $z = 17$ is shown in Figure 5.1.

5.3.2 Cloudy Spectra

To compute DCBH spectra we port spherically-averaged density and temperature profiles of the BH H II region from Enzo to Cloudy. They are tabulated in 33 bins that are uniformly partitioned in log radius and extend to the outer layers of the H II region where the temperature of the gas has fallen below 10^4 K ($\sim$ 30 kpc). Each radial bin, or shell, constitutes a single Cloudy model in which densities and temperatures are assumed to be constant. The spectrum emerging from the outer surface of one shell is calculated and then used as the incident spectrum of the next shell. The spectrum emerging from

the outermost shell of the H II region is taken to be the rest frame spectrum of the quasar.

The spectrum incident to the lower face of the innermost shell is assumed to be a broken power law $F_\nu \propto \nu^\alpha$, where $\alpha = -2$ for $h\nu > 50$ keV (2.48×10^{-5} μm), $\alpha = -1.6$ for 50 keV $> h\nu >$ 0.124 eV (10 μm), and $\alpha = 5/2$ above 10 μm. It is normalized to the bolometric luminosity of the DCBH. Coronal equilibrium is assumed, in which the gas is collisionally ionized. The rest frame spectrum of the DCBH was calculated shortly after its birth at $z = 19$. We require Cloudy to use the temperatures Enzo calculates for the H II region instead of inferring them from the spectrum and luminosity of the BH and its surrounding density field because they take into account cooling due to nonequilibrium primordial gas chemistry in cosmological flows. How we compute AB magnitudes from rest frame Cloudy spectra is described in detail in Surace et al. (2018).

5.4 Detecting DCBHs

We show rest frame spectra for the DCBH at $z = 19$ before and after reprocessing by the halo in Figure 5.2. It has a bolometric luminosity of 4.18×10^{44} erg s^{-1} corresponding to an accretion rate of 0.85 $L_{\rm Edd}$. There is a conspicuous lack of metal lines in the emergent spectrum because star formation has not yet been triggered by X-rays from the BH. Strong Lyα absorption is evident at 1216 Å as is continuum absorption below 912 Å due to the ionization of H. Additional absorption features due to ionization of He I and He II are visible at 504 Å and 227 Å, respectively. Several prominent He emission lines are superimposed on the continuum absorption below 912 Å. There are Hα and weak Paschen series lines at 6560 Å and 12800 Å. Unlike the spectrum of the cool, red progenitor star, there is a lack of continuum absorption above and below 16500 Å due to H^- bound-bound and bound-free opacity in the DCBH spectrum because it is destroyed by radiation from the BH.

5.4.1 NIR Magnitudes

We show AB magnitudes for the DCBH at $z = 8$ - 20 in *JWST* NIRCam bands at 2.5 - 4.6 μm along with 5σ detection limits for the filters for 100 hr exposures in the top left panel of Figure 5.3. The BH is clearly brighter in the NIR than its progenitor star (see Figures 4 and 3 of Surace et al., 2018, 2019, respectively), with AB magnitudes that are 0.5 - 2.5 brighter depending on filter and wavelength. The magnitudes in all four filters are also more tightly grouped together in consequence of the relatively flat power-law spectrum of the BH. The drop in magnitude at $z = 18$ at 2.5 μm is due to the redshifting of the Lyα absorption feature of the rest frame spectrum into that wavelength. The BH is brightest in the 4.60 μm and 4.44 μm filters over all redshifts, with magnitudes that vary from 27.5 - 30.1 from $z = 8$ - 20. We find that detections in all four NIRCam filters are possible out to $z \sim 19$ with 100 hr exposures and in all the bands redward of 3.56 μm out to $z \sim 25$.

As shown in the upper right panel of Figure 5.3, DCBH magnitudes in the MIRI filters are significantly brighter than in NIRCam, ranging from 24.5 - 27 at 25.5 μm to 27 - 29.8 at 5.6 μm for $z = 8$ - 20. Some of these magnitudes are also much brighter than those of the progenitor star. For example, the magnitudes of a red SMS vary from 31 - 32 at 5.6 μm over the same redshift range (Surace et al., 2018). The ordering of the magnitudes with filter wavelength for the SMS is opposite that of the DCBH, with the shortest wavelengths having the brightest magnitudes. This feature is due to continuum absorption by H^- in the envelope of the SMS that is absent from the host halo of the BH. However, while the DCBH magnitudes are brighter in MIRI than NIRCam, the 5σ detection limits for a 100 hour exposure are considerably dimmer, ranging from 24.8 at 18 μm to 28.0 at 5.6 μm. They limit detections of DCBHs to $z = 9$ at 18 μm to $z = 12$ at 5.6 μm. Nevertheless, these AB magnitudes reveal that MIRI could be a powerful instrument for the detection of DCBHs at high redshifts and could discriminate them from SMSs at the same epochs, for which there would be no MIRI signal.

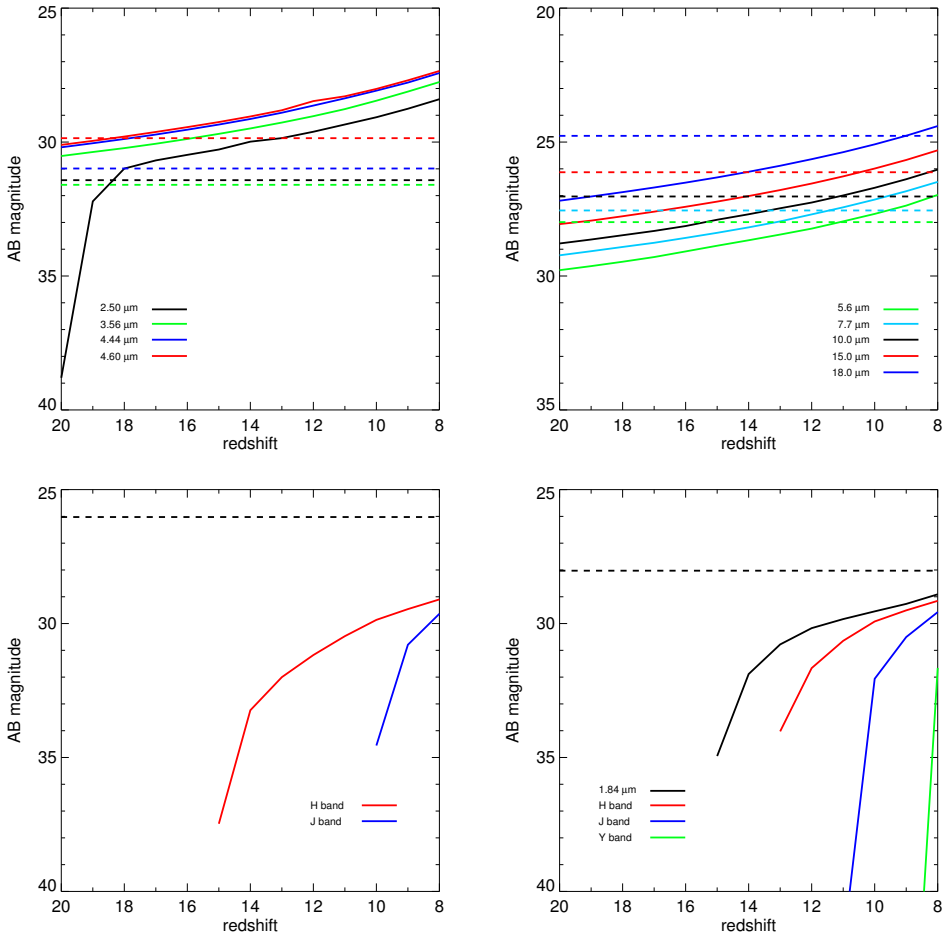

Figure 5.3: NIR AB magnitudes for the 1.0 $\times$ 10^5 $M_\odot$ DCBH at birth as it would appear at z = 8 - 20 in *JWST*, *Euclid* and *WFIRST*. Top left: *JWST* NIRCam bands. The horizontal dashed lines are 5σ AB magnitude detection limits for 100 hour exposures in the filters of corresponding color (2.77 μm: 31.4, 3.56 μm: 31.5, 4.44 μm: 31.0 and 4.60 μm: 29.8). Top right: *JWST* MIRI bands. The horizontal dashed lines are 5σ AB magnitude detection limits for 100 hour exposures in the filters of corresponding color (5.6 μm: 28.0, 7.7 μm: 27.6, 10.0 μm: 27.0, 15.0 μm: 26.1 and 18.0 μm: 24.7). Bottom left: *Euclid*. Bottom right: *WFIRST*. The horizontal dashed lines are detection limits for each instrument (32 for NIRCam, 28 for MIRI assuming a 20 hr exposure, and 26 and 28 for deep-drilling fields in *Euclid* and *WFIRST*, respectively.

We show DCBH magnitudes in the *Euclid* and *WFIRST* bands in the lower two panels of Figure 5.3. Absorption by the neutral IGM at $z \gtrsim 6$ quenches flux in the Y, J and H bands at $z \gtrsim 7$, 10 and 14, respectively, limiting DCBH detections to these redshifts in these filters. Magnitudes vary from 29 - 34 in *Euclid* and 29 - 37 in *WFIRST*. The AB magnitude limits of 26 and 28 for surveys currently planned for *Euclid* and *WFIRST*, respectively, would rule out direct detections of DCBHs at $z \gtrsim 6$ - 8.

5.4.2 DCBH Formation / Detection Rates

While our synthetic spectrum indicates that DCBHs would be detectable in multiband photometric surveys with *JWST* at $z \sim 8$ - 20, the prospect of actually finding such objects in a given survey depends on their formation rates and the time interval over which a DCBH is likely to display tell-tale spectral or photometric signatures. Wise et al. (2019) and Regan et al. (2020) identified atomically cooling haloes at $z \gtrsim 12$ in the Renaissance simulations that could form DCBHs. The 3 DCBH candidate haloes that appeared in their 220 cMpc^3 average-density region over the ~ 70 Myr from $z \sim 14$ - 12 imply a formation rate of $\sim 10^{-10}$ cMpc^{-3} yr^{-1} at these redshifts. While their simulations did not track the subsequent evolution of the gas in these haloes, this formation rate can be used to place an upper limit on detections of DCBHs in future *JWST* surveys.

If we adopt a characteristic time scale of 10^7 yr for the validity of our spectrum (set by when star formation likely begins in its host halo) then we expect a comoving density of observable DCBHs of $\sim 10^{-3}$ $f_{\rm DCBH}$ cMpc^{-3}, where $f_{\rm DCBH}$ is the fraction of candidate haloes that produce $\sim 10^5$ $M_\odot$ BHs. The *JWST* NIRcam field of view (9.7 arcmin^2) covers 1.3×10^4 cMpc^3 per unit redshift at $z \sim 12$, so one would expect $\sim 10 f_{\rm DCBH}$ detectable DCBHs for each such survey field. With planned medium-deep NIRCam multiband surveys covering ~ 20 times this area down to AB mag 29 in the longest-wavelength NIRCam filters (Rieke et al., 2019), the prospects for detecting DCBHs photometrically with *JWST* would appear to be quite good, even if

just some minor fraction ($f_{\rm DCBH} \gtrsim 0.01$) of the Regan et al. (2020) candidate haloes end up forming them. Another route to detection could be to search the field around an unusually bright $z \sim 15$ galaxy found by some other means, as Wise et al. (2019) and Regan et al. (2020) note that the formation rate of DCBHs may rise by more than an order of magnitude in high-density regions, where the most massive first galaxies are also expected to form.

5.5 Discussion and Conclusion

With NIRCam AB mag photometry limits of 31 - 32 and NIRSpec limits of ~ 29, *JWST* will be able to detect the birth of the first quasars at $z \gtrsim 20$ and spectroscopically confirm their redshift out to $z \sim 10$ - 12. Our DCBH magnitudes are consistent with simplified 1D calculations in past studies (Pacucci et al., 2015; Natarajan et al., 2017). As shown in the previous section, up to 10 DCBHs could appear in any given *JWST* field of view from $z = 8$ - 20. But the prospects for discovering them would be better if they could also be found by *Euclid* and *WFIRST* because their wide fields would enclose far more of them at high redshifts. Once flagged, DCBH candidates could then be examined with *JWST* or ground-based extremely large telescopes (ELTs) in greater detail. But, as shown in Figure 5.3, DCBH magnitudes in the H band magnitudes at $z = 8$ - 20 are greater than the detection limits currently envisioned for *Euclid* and *WFIRST* (26 and 28, respectively). In principle, these magnitudes could become brighter if accretion rates exceed the Eddington limit but only modestly so because the luminosity rises only logarithmically with such rates, not linearly.

However, this does not mean *Euclid* and *WFIRST* cannot find DCBHs at birth because only modest gravitational lensing is required to boost their fluxes above their detection limits. The survey areas of both missions will enclose thousands of galaxy clusters and massive galaxies that could lense flux from background DCBHs, and at $z \sim 8$ - 14 magnification factors of only 10 - 100 would be required to reveal them. It is likely that a sufficient

fraction of their survey areas will be magnified by such factors (Rydberg et al., 2018). Even higher magnifications may be realized in future surveys of individual cluster lenses by *JWST* but at the cost of smaller lensing volumes (e.g., Whalen et al., 2013a; Windhorst et al., 2018).

DCBHs can be distinguished from their SMS progenitors at high redshift because they are brighter and have much higher ratios of flux in the MIRI and NIRCam bands. Also, unlike SMSs and high-z galaxies, they are transients because of variations in cosmological flows onto them on timescales as short as the redshifted light-crossing time of the BH. Periodic dimming and brightening could therefore tag these objects as high-z BHs in transient surveys proposed for *JWST* such as FLARE (Wang et al., 2017). Initial redshift cuts can be made for DCBHs because they could appear as dropouts in the NIRCam filters, but more precise determinations would require spectroscopy by instruments such as NIRSpec with *JWST* or MOSAIC for the European ELT (E-ELT). Synergies between *Euclid* or *WFIRST* and *JWST* or the ELTs could open the era of $z = 8$ - 20 quasar astronomy in the coming decade.

Chapter 6

Summary and Conclusions

6.1 Aims

In this thesis, we set out to calculate the observable signatures of cool and hot primordial supermassive stars and their accreting supermassive black hole remnant at birth. The initial conditions from which the first quasars were formed are well constrained by the observed intensity fluctuations in the CMB. However, understanding the physical properties of the first stars and BHs requires following the evolution of density perturbations deep into the non-linear regime where a number of physical processes can strongly affect the late stages of gravitational collapse. These include for example: the effects of turbulence on sub-grid scales, which can affect hydrodynamics on resolved scales, the presence of weak seed magnetic fields, the nature of dark matter (cold vs. warm vs. self-interacting), streaming velocities between dark matter and baryons, or metal pollution due to star formation in the host galaxy. The current lack of observations of objects beyond $z \sim 6 - 7$ underscores the need for detailed numerical predictions to refine our models and inform future survey strategies.

We adopted the promising DCBH scenario in our models as the mechanism for forming massive BH seeds that grow into the observed SMBHs. Stellar mass Pop III star BHs are unlikely to grow to sufficient masses by

$z \sim 6$ since they might not encounter enough gas in their shallower potential wells. The collapse of primordial SMSs in hot, atomically-cooled haloes may have given birth to the first quasars at $z \sim 15$ - 20. We made predictions for the observable signatures of SMSs and DCBHs at various source redshifts, in particular with the new generation of telescopes including *JWST*, *Euclid*, *WFIRST*, and *E-ELT*. This required numerical simulations that resolved highly detailed gas physics and radiative processes over a vast range of scales, from the cosmological down to the subparsec scale. For such simulations, huge memory and computing resources on HPC clusters are necessary.

6.2 Simulations

In Chapter 3 we post-processed a highly resolved Enzo simulation of the atomically cooling accretion envelope surrounding a red, cool SMS, without the inclusion of a star particle in Enzo itself however. The post-processing was performed using the Cloudy code to model the reprocessing of the star's black body radiation by its envelope and calculate synthetic rest-frame spectra. This calculation requires the bolometric luminosity of the star to normalise the spectra, which is calculated using the GENEVA stellar evolution code. It also requires the density and temperature structure of the envelope, including its chemical composition, which is extracted from the Enzo output in the form of 1D spherically averaged profiles. We then developed a routine to take the source frame spectra and transform them into observer frame spectra via cosmological redshifting and geometric dilution. These can then be convolved with instrumental filter transmission functions to calculate AB magnitudes and predict the source's observed brightness at various source redshifts.

In Chapter 4, we post-processed the same Enzo simulation as in Chapter 3, but instead we assumed a hot, blue SMS to be sitting at the centre of the accretion envelope. In this case the Kepler stellar evolution code and the TLUSTY radiative transfer code were used to model the stellar atmosphere

and how it reprocesses the star's own black body spectrum. Cloudy was used again to model reprocessing by the envelope and calculate synthetic rest-frame spectra, and AB magnitude predictions were made for the source at various source redshifts in different filters.

In Chapter 5 we post-processed an Enzo simulation of a DCBH born in cold accretion flows in which it is destined to possess properties that are very similar to those recently measured for ULAS J1120, a 2×10^9 $M_\odot$ SMBH at $z = 7.1$. In this case a BH sink particle was inserted at the centre of the host halo, whose mass evolution is tracked and which provides mechanical and radiative feedback to its environment. As in Chapters 3 and 4, Cloudy was used to post-process the Enzo output and calculate synthetic spectra. These were then transformed to the observer frame to calculate AB magnitudes and predict the DCBH at birth's observed brightness for different source redshifts and different filters.

6.3 Conclusions and Future Prospects

Our results suggest that synergies between *Euclid* or *WFIRST* and *JWST* or the ELTs could open up the era of $z = 8$ - 20 quasar astronomy in the 2020s.

We have shown that red, cool supermassive stars could be visible to *JWST* at $z \lesssim 20$. Rather than obscuring the star, its accretion envelope enhances its visibility in the NIR today by reprocessing its short-wavelength flux into photons that are just redward of the Lyman limit in the rest frame of the star. With modest gravitational lensing, *Euclid* and *WFIRST* could also detect them out to $z \sim 10$ - 12. Their wide fields of view will enclose thousands of massive galaxies and galaxy clusters, and at $z \sim 6-12$ magnification factors of only 10 - 100 are sufficient to reveal the star.

We have also shown that photometric detections of blue, hot supermassive stars by *JWST* will be limited to $z \lesssim 10$ - 12, lower redshifts than those at which red stars can be found, because of quenching by their accretion envelopes. With moderate gravitational lensing however, we found that *Euclid*

and *WFIRST* could detect blue SMSs out to similar redshifts in wide-field surveys.

Finally, our results for DCBHs at birth reveal that they could be photometrically detected with NIRcam on *JWST* at $z \lesssim 20$ and spectroscopically confirmed with NIRSpec on *JWST* out to $z \sim 10 - 12$. Strongly-lensed DCBHs could be found in future wide-field surveys by *Euclid* and *WFIRST* at $z \lesssim 15$.

The next generation of space-based telescopes launching in the coming decade: *JWST*, *Euclid* and *WFIRST*, as well as ground-based telescopes such as *E-ELT*, will represent a step change in our ability to peer into the distant past, especially in the NIR band for wavelengths $\sim$ 1-5 μm. The planned space-bound gravitational wave interferometer LISA might also be able to uniquely identify the SMBH relics of SMSs at $z > 15$ if they form in binaries.

In future Enzo simulation campaigns, we could include more physics by switching on magnetic fields to investigate their influence on the development of the atomically cooling accretion disk forming at the centre of the halo. We could also investigate different initial BH sink particle seed masses, i.e. 10^3 and 10^4 $M_{\odot}$, and follow their growth histories to compare with our fiducial 10^5 $M_{\odot}$ case. Additionally, models for dust grains could be included in future Cloudy calculations, which will deplete the gas phase metal abundances, to see how they modify the predicted source spectrum. They might be present in the DCBH host galaxies though there is currently no observational evidence as to their composition or abundances at such high redshifts.

A well known issue with the AMR Enzo code is that the simulation scales poorly beyond 512 processors on distributed memory machines. For example, the inclusion of costly MORAY ray tracing of UV and X-ray photons from star or BH particles can considerably lengthen the execution time. To address this issue, a new version of Enzo is under development, known as Enzo-P i.e. the 'petascale' version, which will scale better on larger numbers of cores. This will enable us to perform simulations with a larger box size than is currently possible, potentially avoiding having to simulate many smaller

boxes to obtain a halo with the properties we desire. At the same time we would be able to refine to small scales deep inside the DCBH host halo, enabling us to capture the physical processes occurring over a vast range of scales.

Bibliography

Abel T., Wandelt B. D., 2002, Monthly Notices of the Royal Astronomical Society, 330, L53

Abel T., Anninos P., Norman M. L., Zhang Y., 1998, The Astrophysical Journal, 508, 518

Agarwal B., Khochfar S., 2015, Monthly Notices of the Royal Astronomical Society, 446, 160

Agarwal B., Khochfar S., Johnson J. L., Neistein E., Dalla Vecchia C., Livio M., 2012, Monthly Notices of the Royal Astronomical Society, 425, 2854

Agarwal B., Davis A. J., Khochfar S., Natarajan P., Dunlop J. S., 2013, Monthly Notices of the Royal Astronomical Society, 432, 3438

Agarwal B., Smith B., Glover S., Natarajan P., Khochfar S., 2016a, Monthly Notices of the Royal Astronomical Society, 459, 4209

Agarwal B., Smith B., Glover S., Natarajan P., Khochfar S., 2016b, Monthly Notices of the Royal Astronomical Society, 459, 4209

Agarwal B., Johnson J. L., Khochfar S., Pellegrini E., Rydberg C.-E., Klessen R. S., Oesch P., 2017, Monthly Notices of the Royal Astronomical Society, 469, 231

Alexander T., Natarajan P., 2014, Science, 345, 1330

Alvarez M. A., Wise J. H., Abel T., 2009, The Astrophysical Journal Letters, 701, L133

Appenzeller I., Fricke K., 1972, Astronomy and Astrophysics, 18, 10

Ardaneh K., Luo Y., Shlosman I., Nagamine K., Wise J. H., Begelman M. C., 2018, Monthly Notices of the Royal Astronomical Society, 479, 2277

Aykutalp A., Wise J. H., Spaans M., Meijerink R., 2014, The Astrophysical Journal, 797, 139

Bañados E., et al., 2018, Nature, 553, 473

Badnell N. R., 2006, The Astrophysical Journal Supplement Series, 167, 334

Badnell N. R., et al., 2003, Astronomy & Astrophysics, 406, 1151

Banik N., Tan J. C., Monaco P., 2018, Monthly Notices of the Royal Astronomical Society, 483, 3592

Baumgarte T. W., Shapiro S. L., 1999, The Astrophysical Journal, 526, 941

Becerra F., Greif T. H., Springel V., Hernquist L. E., 2015, Monthly Notices of the Royal Astronomical Society, 446, 2380

Becerra F., Marinacci F., Bromm V., Hernquist L. E., 2018, Monthly Notices of the Royal Astronomical Society, 480, 5029

Begelman M. C., Rees M. J., 1978, Monthly Notices of the Royal Astronomical Society, 185, 847

Begelman M. C., Volonteri M., Rees M. J., 2006, Monthly Notices of the Royal Astronomical Society, 370, 289

Begelman M. C., Rossi E. M., Armitage P. J., 2008, Monthly Notices of the Royal Astronomical Society, 387, 1649

Boekholt T. C. N., Schleicher D. R. G., Fellhauer M., Klessen R. S., Reinoso B., Stutz A. M., Haemmerlé L., 2018, Monthly Notices of the Royal Astronomical Society, 476, 366

Bondi H., Hoyle F., 1944, Monthly Notices of the Royal Astronomical Society, 104, 273

Bournaud F., Dekel A., Teyssier R., Cacciato M., Daddi E., Juneau S., Shankar F., 2011, The Astrophysical Journal Letters, 741, L33

Bowler R. A. A., McLure R. J., Dunlop J. S., McLeod D. J., Stanway E. R., Eldridge J. J., Jarvis M. J., 2017, Monthly Notices of the Royal Astronomical Society, 469, 448

Bromm V., Loeb A., 2003, The Astrophysical Journal, 596, 34

Bromm V., Yoshida N., 2011, Annual Review of Astronomy and Astrophysics, 49, 373

Bromm V., Coppi P. S., Larson R. B., 2002, The Astrophysical Journal, 564, 23

Bromm V., Yoshida N., Hernquist L., McKee C. F., 2009, Nature, 459, 49

Bryan G. L., et al., 2014, The Astrophysical Journal Supplement, 211, 19

Butler S. P., Lima A. R., Baumgarte T. W., Shapiro S. L., 2018, Monthly Notices of the Royal Astronomical Society, 477, 3694

Cen R., Ostriker J. P., 1992, The Astrophysical Journal Letters, 399, L113

Chandrasekhar S., 1964, The Astrophysical Journal, 140, 417

Chen K.-J., Heger A., Woosley S., Almgren A., Whalen D. J., Johnson J. L., 2014, The Astrophysical Journal, 790, 162

Chen K.-J., Heger A., Whalen D. J., Moriya T. J., Bromm V., Woosley S. E., 2017a, Monthly Notices of the Royal Astronomical Society, 467, 4731

Chen K.-J., Whalen D. J., Wollenberg K. M. J., Glover S. C. O., Klessen R. S., 2017b, The Astrophysical Journal, 844, 111

Chon S., Hosokawa T., Yoshida N., 2017, arXiv:1711.05262,

Ciotti L., Ostriker J. P., Proga D., 2009, The Astrophysical Journal, 699, 89

Clark P. C., Glover S. C. O., Smith R. J., Greif T. H., Klessen R. S., Bromm V., 2011, Science, 331, 1040

Costa T., Sijacki D., Trenti M., Haehnelt M. G., 2014a, Monthly Notices of the Royal Astronomical Society, 439, 2146

Costa T., Sijacki D., Trenti M., Haehnelt M. G., 2014b, Monthly Notices of the Royal Astronomical Society, 439, 2146

D'Amico G., Panci P., Lupi A., Bovino S., Silk J., 2018, Monthly Notices of the Royal Astronomical Society, 473, 328

DeBuhr J., Quataert E., Ma C.-P., Hopkins P., 2010, Monthly Notices of the Royal Astronomical Society, 406, L55

Dekel A., Birnboim Y., 2006, Monthly Notices of the Royal Astronomical Society, 368, 2

Dekel A., et al., 2009, Nature, 457, 451

Dere K. P., E. Landi Mason, H. E. Monsignori Fossi, B. C. Young, P. R. 1997, Astron. Astrophys. Suppl. Ser., 125, 149

Devecchi B., Volonteri M., 2009, The Astrophysical Journal, 694, 302

Di Matteo T., Khandai N., DeGraf C., Feng Y., Croft R. A. C., Lopez J., Springel V., 2012, The Astrophysical Journal Letters, 745, L29

Dijkstra M., Haiman Z., Mesinger A., Wyithe J. S. B., 2008, Monthly Notices of the Royal Astronomical Society, 391, 1961

Dijkstra M., Sethi S., Loeb A., 2016a, The Astrophysical Journal, 820, 10

Dijkstra M., Gronke M., Sobral D., 2016b, The Astrophysical Journal, 823, 74

Dubois Y., Volonteri M., Silk J., Devriendt J., Slyz A., Teyssier R., 2015, Monthly Notices of the Royal Astronomical Society, 452, 1502

Federrath C., Sur S., Schleicher D. R. G., Banerjee R., Klessen R. S., 2011, The Astrophysical Journal, 731, 62

Feng Y., Di Matteo T., Croft R., Khandai N., 2014a, Monthly Notices of the Royal Astronomical Society, 440, 1865

Feng Y., Di Matteo T., Croft R., Khandai N., 2014b, Monthly Notices of the Royal Astronomical Society, 440, 1865

Ferland G. J., et al., 2017, *Rev. Mex. Astron & Astrophys*, 53, 385

Ferrara A., Salvadori S., Yue B., Schleicher D., 2014, Monthly Notices of the Royal Astronomical Society, 443, 2410

Field G. B., Partridge R. B., 1961, Astrophysical Journal, 134, 959

Fowler W. A., 1964, Reviews of Modern Physics, 36, 545

Fowler W. A., 1966, The Astrophysical Journal, 144, 180

Freese K., Bodenheimer P., Spolyar D., Gondolo P., 2008, The Astrophysical Journal, 685, L101

Freese K., Ilie C., Spolyar D., Valluri M., Bodenheimer P., 2010, The Astrophysical Journal, 716, 1397

Freese K., Rindler-Daller T., Spolyar D., Valluri M., 2016, Reports on Progress in Physics, 79, 066902

Fuller G. M., Woosley S. E., Weaver T. A., 1986, The Astrophysical Journal, 307, 675

Gardner J. P., et al., 2006, Space Science Reviews, 123, 485

Glover S. C. O., 2015, Monthly Notices of the Royal Astronomical Society, 451, 2082

Glover S. C. O., Abel T., 2008, Monthly Notices of the Royal Astronomical Society, 388, 1627

Glover S. C. O., Jappsen A.-K., 2007, The Astrophysical Journal, 666, 1

Greif T. H., White S. D. M., Klessen R. S., Springel V., 2011a, The Astrophysical Journal, 736, 147

Greif T. H., Springel V., White S. D. M., Glover S. C. O., Clark P. C., Smith R. J., Klessen R. S., Bromm V., 2011b, The Astrophysical Journal, 737, 75

Greif T. H., Bromm V., Clark P. C., Glover S. C. O., Smith R. J., Klessen R. S., Yoshida N., Springel V., 2012, Monthly Notices of the Royal Astronomical Society, 424, 399

Gunn J. E., Peterson B. A., 1965, ApJ, 142, 1633

Habouzit M., Volonteri M., Latif M., Dubois Y., Peirani S., 2016, Monthly Notices of the Royal Astronomical Society, 463, 529

Habouzit M., Volonteri M., Dubois Y., 2017, Monthly Notices of the Royal Astronomical Society, 468, 3935

Haemmerlé L., Meynet G., 2019, Astronomy & Astrophysics, 623, L7

Haemmerlé L., Woods T. E., Klessen R. S., Heger A., Whalen D. J., 2018a, Monthly Notices of the Royal Astronomical Society, 474, 2757

Haemmerlé L., Woods T. E., Klessen R. S., Heger A., Whalen D. J., 2018b, The Astrophysical Journal Letters, 853, L3

Hahn O., Abel T., 2011, Monthly Notices of the Royal Astronomical Society, 415, 2101

Hartwig T., et al., 2016, Monthly Notices of the Royal Astronomical Society, 462, 2184

Hartwig T., Agarwal B., Regan J. A., 2018, Monthly Notices of the Royal Astronomical Society, 479, L23

Heger A., Woosley S. E., 2002, The Astrophysical Journal, 567, 532

Heger A., Fryer C. L., Woosley S. E., Langer N., Hartmann D. H., 2003, The Astrophysical Journal, 591, 288

Hirano S., Hosokawa T., Yoshida N., Umeda H., Omukai K., Chiaki G., Yorke H. W., 2014, The Astrophysical Journal, 781, 60

Hirano S., Hosokawa T., Yoshida N., Omukai K., Yorke H. W., 2015, Monthly Notices of the Royal Astronomical Society, 448, 568

Hirano S., Hosokawa T., Yoshida N., Kuiper R., 2017, Science, 357, 1375

Hirschmann M., Dolag K., Saro A., Bachmann L., Borgani S., Burkert A., 2014, Monthly Notices of the Royal Astronomical Society, 442, 2304

Hosokawa T., Omukai K., Yoshida N., Yorke H. W., 2011, Science, 334, 1250

Hosokawa T., Yorke H. W., Inayoshi K., Omukai K., Yoshida N., 2013, The Astrophysical Journal, 778, 178

Hubeny I., Lanz T., 1995, The Astrophysical Journal, 439, 875

Hummel J. A., Stacy A., Bromm V., 2016, Monthly Notices of the Royal Astronomical Society, 460, 2432

Iben Jr. I., 1963, The Astrophysical Journal, 138, 1090

Ilie C., Freese K., Valluri M., Iliev I. T., Shapiro P. R., 2012, Monthly Notices of the Royal Astronomical Society, 422, 2164

Inayoshi K., Omukai K., 2012, Monthly Notices of the Royal Astronomical Society, 422, 2539

Inayoshi K., Omukai K., Tasker E., 2014, Monthly Notices of the Royal Astronomical Society, 445, L109

Inayoshi K., Visbal E., Kashiyama K., 2015, Monthly Notices of the Royal Astronomical Society, 453, 1692

Inayoshi K., Haiman Z., Ostriker J. P., 2016, Monthly Notices of the Royal Astronomical Society, 459, 3738

Johnson J. L., Whalen D. J., Fryer C. L., Li H., 2012, The Astrophysical Journal, 750, 66

Johnson J. L., Whalen D. J., Li H., Holz D. E., 2013a, The Astrophysical Journal, 771, 116

Johnson J. L., Whalen D. J., Even W., Fryer C. L., Heger A., Smidt J., Chen K.-J., 2013b, The Astrophysical Journal, 775, 107

Kalirai J., 2018, Contemporary Physics, 59, 251

Katz H., Sijacki D., Haehnelt M. G., 2015, Monthly Notices of the Royal Astronomical Society, 451, 2352

Kitayama T., Yoshida N., 2005, The Astrophysical Journal, 630, 675

Landi E., Zanna G. D., Young P. R., Dere K. P., Mason H. E., 2011, The Astrophysical Journal, 744, 99

Lanz T., Hubeny I., 2003, The Astrophysical Journal Supplement Series, 146, 417

Lanz T., Hubeny I., 2007, The Astrophysical Journal Supplement Series, 169, 83

Latif M. A., Ferrara A., 2016, Publications of the Astronomical Society of Australia, 33, e051

Latif M. A., Volonteri M., 2015, Monthly Notices of the Royal Astronomical Society, 452, 1026

Latif M. A., Schleicher D. R. G., Schmidt W., Niemeyer J., 2013, Monthly Notices of the Royal Astronomical Society, 430, 588

Latif M. A., Niemeyer J. C., Schleicher D. R. G., 2014a, Monthly Notices of the Royal Astronomical Society, 440, 2969

Latif M. A., Bovino S., Van Borm C., Grassi T., Schleicher D. R. G., Spaans M., 2014b, Monthly Notices of the Royal Astronomical Society, 443, 1979

Latif M. A., Bovino S., Grassi T., Schleicher D. R. G., Spaans M., 2015, Monthly Notices of the Royal Astronomical Society, 446, 3163

Latif M. A., Khochfar S., Whalen D., 2020, The Astrophysical Journal, 892, L4

Laureijs R., et al., 2011, arXiv:1110.3193,

Li Y., et al., 2007, The Astrophysical Journal, 665, 187

Lodato G., Natarajan P., 2006, Monthly Notices of the Royal Astronomical Society, 371, 1813

Luo Y., Ardaneh K., Shlosman I., Nagamine K., Wise J. H., Begelman M. C., 2018, Monthly Notices of the Royal Astronomical Society, 476, 3523

Lupi A., Haardt F., Dotti M., Fiacconi D., Mayer L., Madau P., 2016, Monthly Notices of the Royal Astronomical Society, 456, 2993

Machacek M. E., Bryan G. L., Abel T., 2003, Monthly Notices of the Royal Astronomical Society, 338, 273

Madau P., Haardt F., Dotti M., 2014, The Astrophysical Journal Letters, 784, L38

Mayer L., Bonoli S., 2019, Reports on Progress in Physics, 82, 016901

Mayer L., Kazantzidis S., Escala A., Callegari S., 2010, Nature, 466, 1082

Mayer L., Fiacconi D., Bonoli S., Quinn T., Roškar R., Shen S., Wadsley J., 2015, The Astrophysical Journal, 810, 51

McLure R. J., Dunlop J. S., 2004, Monthly Notices of the Royal Astronomical Society, 352, 1390

Mezcua M., 2017, International Journal of Modern Physics D, 26, 1730021

Milosavljević M., Couch S. M., Bromm V., 2009a, The Astrophysical Journal Letters, 696, L146

Milosavljević M., Bromm V., Couch S. M., Oh S. P., 2009b, The Astrophysical Journal, 698, 766

Montero P. J., Janka H.-T., Müller E., 2012, The Astrophysical Journal, 749, 37

Mortlock D. J., et al., 2011, Nature, 474, 616

Nanni R., Vignali C., Gilli R., Moretti A., Brandt W. N., 2017, Astronomy and Astrophysics, 603, A128

Natarajan P., Pacucci F., Ferrara A., Agarwal B., Ricarte A., Zackrisson E., Cappelluti N., 2017, The Astrophysical Journal, 838, 117

O'Shea B. W., Abel T., Whalen D., Norman M. L., 2005, The Astrophysical Journal Letters, 628, L5

Oguri M., Marshall P. J., 2010, Monthly Notices of the Royal Astronomical Society, 405, 2579

Omukai K., 2001, The Astrophysical Journal, 546, 635

Omukai K., Tsuribe T., Schneider R., Ferrara A., 2005, The Astrophysical Journal, 626, 627

Osaki Y., 1966, Publications of the ASJ, 18, 384

Pacucci F., Ferrara A., Volonteri M., Dubus G., 2015, Monthly Notices of the Royal Astronomical Society, 454, 3771

Pacucci F., Pallottini A., Ferrara A., Gallerani S., 2017, Monthly Notices of the Royal Astronomical Society, 468, L77

Pallottini A., Ferrara A., Gallerani S., Salvadori S., D'Odorico V., 2014, Monthly Notices of the Royal Astronomical Society, 440, 2498

Pallottini A., et al., 2015, Monthly Notices of the Royal Astronomical Society, 453, 2465

Park K., Ricotti M., 2011, The Astrophysical Journal, 739, 2

Park K., Ricotti M., 2012, The Astrophysical Journal, 747, 9

Park K., Ricotti M., 2013, The Astrophysical Journal, 767, 163

Pezzulli E., Valiante R., Schneider R., 2016, Monthly Notices of the Royal Astronomical Society, 458, 3047

Pezzulli E., Volonteri M., Schneider R., Valiante R., 2017, Monthly Notices of the Royal Astronomical Society, 471, 589

Planck Collaboration et al., 2016, Astronomy and Astrophysics, 594, A13

Press W. H., Schechter P., 1974, Astrophysical Journal, 187, 425

Rees M. J., 1978, The Observatory, 98, 210

Regan J. A., Downes T. P., 2018, Monthly Notices of the Royal Astronomical Society, 475, 4636

Regan J. A., Haehnelt M. G., 2009a, Monthly Notices of the Royal Astronomical Society, 393, 858

Regan J. A., Haehnelt M. G., 2009b, Monthly Notices of the Royal Astronomical Society, 396, 343

Regan J. A., Johansson P. H., Wise J. H., 2014, The Astrophysical Journal, 795, 137

Regan J. A., Visbal E., Wise J. H., Haiman Z., Johansson P. H., Bryan G. L., 2017, Nature Astronomy, 1, 0075

Regan J. A., Wise J. H., O'Shea B. W., Norman M. L., 2020, Monthly Notices of the Royal Astronomical Society, 492, 3021

Reinoso B., Schleicher D. R. G., Fellhauer M., Klessen R. S., Boekholt T. C. N., 2018, Astronomy & Astrophysics, 614, A14

Rieke M., et al., 2019, Bulletin of the American Astronomical Society, 51, 45

Ritter J. S., Safranek-Shrader C., Gnat O., Milosavljević M., Bromm V., 2012, The Astrophysical Journal, 761, 56

Ritter J. S., Sluder A., Safranek-Shrader C., Milosavljević M., Bromm V., 2015, Monthly Notices of the Royal Astronomical Society, 451, 1190

Ritter J. S., Safranek-Shrader C., Milosavljević M., Bromm V., 2016, Monthly Notices of the Royal Astronomical Society, 463, 3354

Rydberg C.-E., Whalen D. J., Maturi M., Collett T., Carrasco M., Magg M., Klessen R. S., 2018, arXiv:1805.02662,

Safranek-Shrader C., Milosavljević M., Bromm V., 2014, Monthly Notices of the Royal Astronomical Society, 438, 1669

Sakurai Y., Hosokawa T., Yoshida N., Yorke H. W., 2015, Monthly Notices of the Royal Astronomical Society, 452, 755

Sakurai Y., Vorobyov E. I., Hosokawa T., Yoshida N., Omukai K., Yorke H. W., 2016a, Monthly Notices of the Royal Astronomical Society, 459, 1137

Sakurai Y., Inayoshi K., Haiman Z., 2016b, Monthly Notices of the Royal Astronomical Society, 461, 4496

Sakurai Y., Yoshida N., Fujii M. S., Hirano S., 2017, Monthly Notices of the Royal Astronomical Society, 472, 1677

Schaerer D., 2002, Astronomy and Astrophysics, 382, 28

Schauer A. T. P., Regan J., Glover S. C. O., Klessen R. S., 2017, Monthly Notices of the Royal Astronomical Society, 471, 4878

Schneider R., Omukai K., Limongi M., Ferrara A., Salvaterra R., Chieffi A., Bianchi S., 2012, Monthly Notices of the Royal Astronomical Society: Letters, 423, L60

Shang C., Bryan G. L., Haiman Z., 2010, Monthly Notices of the Royal Astronomical Society, 402, 1249

Shapiro S. L., Teukolsky S. A., 1979, The Astrophysical Journal Letters, 234, L177

Sijacki D., Springel V., Haehnelt M. G., 2009, Monthly Notices of the Royal Astronomical Society, 400, 100

Sluder A., Ritter J. S., Safranek-Shrader C., Milosavljević M., Bromm V., 2016, Monthly Notices of the Royal Astronomical Society, 456, 1410

Smidt J., Whalen D. J., Johnson J. L., Surace M., Li H., 2018, The Astrophysical Journal, 865, 126

Smith A., Safranek-Shrader C., Bromm V., Milosavljević M., 2015a, Monthly Notices of the Royal Astronomical Society, 449, 4336

Smith B. D., Wise J. H., O'Shea B. W., Norman M. L., Khochfar S., 2015b, Monthly Notices of the Royal Astronomical Society, 452, 2822

Smith B. D., et al., 2017a, Monthly Notices of the Royal Astronomical Society, 466, 2217

Smith A., Becerra F., Bromm V., Hernquist L., 2017b, Monthly Notices of the Royal Astronomical Society, 472, 205

Smith B. D., Regan J. A., Downes T. P., Norman M. L., O'Shea B. W., Wise J. H., 2018, Monthly Notices of the Royal Astronomical Society, 480, 3762

Sobral D., Matthee J., Darvish B., Schaerer D., Mobasher B., Röttgering H. J. A., Santos S., Hemmati S., 2015, The Astrophysical Journal, 808, 139

Spergel D., et al., 2015, arXiv:1503.03757,

Spitzer L., 1978, Physical processes in the interstellar medium

Spolyar D., Freese K., Gondolo P., 2008, Physical Review Letters, 100

Springel V., 2005, Monthly Notices of the Royal Astronomical Society, 364, 1105

Springel V., et al., 2005, Nature, 435, 629

Stacy A., Greif T. H., Bromm V., 2010, Monthly Notices of the Royal Astronomical Society, 403, 45

Stacy A., Bromm V., Loeb A., 2011, The Astrophysical Journal Letters, 730, L1

Sun L., Ruiz M., Shapiro S. L., 2018, Physical Review D, 98, 103008

Sunyaev R. A., Zeldovich Y. B., 1970, Astrophysics and Space Science, 7, 3

Surace M., et al., 2018, The Astrophysical Journal, 869, L39

Surace M., Zackrisson E., Whalen D. J., Hartwig T., Glover S. C. O., Woods T. E., Heger A., 2019, Monthly Notices of the Royal Astronomical Society, 488, 3995

Tanaka T. L., Li M., 2014, Monthly Notices of the Royal Astronomical Society, 439, 1092

Tanaka T. L., Li M., Haiman Z., 2013, Monthly Notices of the Royal Astronomical Society, 435, 3559

Trenti M., Santos M. R., Stiavelli M., 2008, The Astrophysical Journal, 687, 1

Truelove J. K., Klein R. I., McKee C. F., Holliman II J. H., Howell L. H., Greenough J. A., 1997, The Astrophysical Journal Letters, 489, L179

Tseliakhovich D., Hirata C., 2010, Physical Review D, 82, 083520

Turk M. J., Abel T., O'Shea B., 2009, Science, 325, 601

Turk M. J., Oishi J. S., Abel T., Bryan G. L., 2012, The Astrophysical Journal, 745, 154

Umeda H., Hosokawa T., Omukai K., Yoshida N., 2016, The Astrophysical Journal Letters, 830, L34

Valiante R., Agarwal B., Habouzit M., Pezzulli E., 2017, Publications of the Astronomical Society of Australia, 34, e031

Van Borm C., Bovino S., Latif M. A., Schleicher D. R. G., Spaans M., Grassi T., 2014, Astronomy and Astrophysics, 572, A22

Volonteri M., Silk J., Dubus G., 2015, The Astrophysical Journal, 804, 148

Wang L., et al., 2017, arXiv:1710.07005,

Whalen D. J., Fryer C. L., 2012, The Astrophysical Journal Letters, 756, L19

Whalen D., Abel T., Norman M. L., 2004, The Astrophysical Journal, 610, 14

Whalen D., O'Shea B. W., Smidt J., Norman M. L., 2008a, The Astrophysical Journal, 679, 925

Whalen D., van Veelen B., O'Shea B. W., Norman M. L., 2008b, The Astrophysical Journal, 682, 49

Whalen D., Hueckstaedt R. M., McConkie T. O., 2010, The Astrophysical Journal, 712, 101

Whalen D. J., Smidt J., Johnson J. L., Holz D. E., Stiavelli M., Fryer C. L., 2013a, arXiv:1312.6330,

Whalen D. J., Fryer C. L., Holz D. E., Heger A., Woosley S. E., Stiavelli M., Even W., Frey L. H., 2013b, The Astrophysical Journal Letters, 762, L6

Whalen D. J., Johnson J. L., Smidt J., Meiksin A., Heger A., Even W., Fryer C. L., 2013c, The Astrophysical Journal, 774, 64

Whalen D. J., Johnson J. L., Smidt J., Heger A., Even W., Fryer C. L., 2013d, The Astrophysical Journal, 777, 99

Whalen D. J., et al., 2013e, The Astrophysical Journal, 777, 110

Whalen D. J., Smidt J., Even W., Woosley S. E., Heger A., Stiavelli M., Fryer C. L., 2014, The Astrophysical Journal, 781, 106

Whalen D., Hartwig T., Surace M., 2019, Monthly Notices of the Royal Astronomical Society, in prep

White S. D. M., Rees M. J., 1978, Monthly Notices of the Royal Astronomical Society, 183, 341

Windhorst R. A., et al., 2018, The Astrophysical Journal Supplement, 234, 41

Wise J. H., Abel T., 2011, Monthly Notices of the Royal Astronomical Society, 414, 3458

Wise J. H., Turk M. J., Abel T., 2008, The Astrophysical Journal, 682, 745

Wise J. H., Regan J. A., O'Shea B. W., Norman M. L., Downes T. P., Xu H., 2019, Nature, 566, 85

Wolcott-Green J., Haiman Z., Bryan G. L., 2011, Monthly Notices of the Royal Astronomical Society, 418, 838

Woods T. E., Heger A., Whalen D. J., Haemmerlé L., Klessen R. S., 2017, The Astrophysical Journal Letters, 842, L6

Woods T. E., et al., 2018, arXiv:1810.12310,

Xu H., Ahn K., Wise J. H., Norman M. L., O'Shea B. W., 2014, The Astrophysical Journal, 791, 110

Yorke H. W., Bodenheimer P., 2008, Theoretical Developments in Understanding Massive Star Formation. p. 189

Yoshida N., Abel T., Hernquist L., Sugiyama N., 2003, The Astrophysical Journal, 592, 645

Zackrisson E., et al., 2010a, Monthly Notices of the Royal Astronomical Society, 407, L74

Zackrisson E., et al., 2010b, The Astrophysical Journal, 717, 257

Zel'dovich Y. B., Novikov I. D., 1967, Soviet Astronomy, 10, 602